



كلية العلوم  
Faculté des Sciences  
جامعة محمد الأول وجدة

MOHAMMED FIRST UNIVERSITY  
FACULTY OF SCIENCES  
OUJDA



جامعة محمد الأول وجدة  
UNIVERSITE MOHAMMED PREMIER OUJDA  
جامعة محمد الأول وجدة

## DOCTORAL THESIS

To obtain the grad of Doctor in Physics from  
Mohammed first University in Oujda

**Speciality: Physics**

Mention: Physics of matter and radiation  
high-energy physics, and experimentation

---

### Search for nuclearites with ANTARES and contribution to the construction of the KM3NeT telescope

---

Presnted by:  
Mohammed Bouda

Supervised by:  
Prof. Abdelilah Moussa

Defendef in front of the jury members:

Prof. Antoine Kouchner (President)	Paris Diderot University - Paris 7
Prof. Gouighri Mohammed (Reviwer)	Faculty of Sciences, Ibn Tofail University - Kenitra
Prof. El Hassan Tahrie (Reviwer)	Faculty of Sciences, Mohammed I University - Oujda
Prof. Mohammed Hamal (Reviwer)	Faculty of Sciences, Mohammed I University - Oujda
Prof. Rajaa Cherkaoui (Examiner)	Faculty of Sciences, Mohammed V University - Rabat
Prof. Yahya Tayalati (Examiner)	Faculty of Sciences, Mohammed V University - Rabat
Prof. Abdelilah Moussa (Thesis supervisor)	Faculty of Sciences, Mohammed I University - Oujda

Oujda, 08/07/2023

Physics of matter and radiation laboratory

## **Abstract**

---

The interaction of theoretical and experimental physics plays an essential role in developing our knowledge of the fundamental concepts that govern the structure of the universe. This dissertation begins a thorough investigation at the interface of theoretical and experimental physics, concentrating on the enigmatic domains of neutrinos, exotic particles, and cutting-edge detectors.

The first chapter provides the theoretical base, getting into the complex worlds of neutrino physics and exotic particles. These serve as the starting point for our search for the nuclearites and establish a frame for the coming chapters. The second chapter is a comprehensive description of the ANTARES neutrinos telescope, a key component of equipment that forms the basis our study. This chapter emphasizes the significance of experimental data in establishing a solid foundation for our investigations. The Third chapter details our in-depth analysis of the enigmatic nuclearites within the ANTARES framework. We report on the complete research that resulted in the determination of an upper limit on the nuclearite flow using the Fieldman-Cousins approach, based on nine years of experimental data. The fourth and final part focuses on the KM3Net telescope, stressing Morocco's significant contributions to the integration of base modules and digital optical modules. An investigation of the reconstruction of magnetic monopoles within the ORCA detector is discussed within the context of the KM3Net neutrinos telescope.

This dissertation emphasizes the significant interaction between theoretical and experimental physics, revealing insights into the universe's fundamental theories. It is a dedication to the never-ending search of knowledge, where theoretical notions are tested in the crucible of experimental rigor, resulting in a deeper comprehension of the universe and the processes that form it.

---

## **ملخص**

إن التفاعل بين الفيزياء النظرية والتجريبية يلعب دوراً أساسياً في تطوير معرفتنا بالمفاهيم الأساسية التي تحكم بنية الكون. تجمع هذه الأطروحة بين الفيزياء النظرية والتجريبية، مع التركيز على المجالات الغامضة للنيوترونات، والجسيمات الغريبة، وأجهزة الكشف المتقدمة.

يقدم الفصل الأول الأساس النظري، ويدخل في العالم المعقّد لفيزياء النيوترونو والجسيمات الغريبة. وهذه بمثابة نقطة انطلاق لبحثنا عن النيكليلاريات وتأسیس إطار للحصول القادمة. أما الفصل الثاني فهو وصف شامل لتلسكوب النيوترونو، ANTARES وهو مكون رئيسي للمعدات التي تشكل أساس دراستنا. يؤكد هذا الفصل على أهمية البيانات التجريبية في إنشاء أساس متين لدراستنا. يعرض الفصل الثالث تفاصيل تحليلنا المتعمق للنيكليلاريات ضمن إطار ANTARES. نحن نقدم تقريراً عن البحث الكامل الذي أدى إلى تحديد الحد الأعلى لتدفق النيكليلاريات باستخدام نهج Fieldman-Cousins، استناداً إلى تسع سنوات من البيانات التجريبية. أما الجزء الرابع والأخير، فيركز على تلسكوب KM3NeT، مؤكداً على مساهمات المغرب الكبيرة في تكامل الوحدات الأساسية والوحدات البصرية الرقمية كما تمت مناقشة التحقيق في إعادة بناء أحاديث القطب المغناطيسي داخل كاشف ORCA في سياق تلسكوب النيوترونات KM3NeT.

تؤكد هذه الأطروحة على التفاعل الكبير بين الفيزياء النظرية والتجريبية، وتكتشف عن روى حول النظريات الأساسية للكون. إنه تكريس للبحث الذي لا ينتهي عن المعرفة، حيث يتم اختبار المفاهيم النظرية في ظل الدقة التجريبية، مما يؤدي إلى فهم أعمق للكون والعمليات التي تشكله.

---

## **Résumé**

L'interaction de la physique théorique et expérimentale joue un rôle essentiel dans le développement de notre connaissance des concepts fondamentaux qui régissent la structure de l'univers. Cette thèse commence une étude approfondie à l'interface de la physique théorique et expérimentale, en se concentrant sur les domaines énigmatiques des neutrinos, des particules exotiques et des détecteurs de pointe.

Le premier chapitre fournit la base théorique, abordant les mondes complexes de la physique des neutrinos et des particules exotiques. Ceux-ci servent de point de départ à notre recherche des nuclearites et établissent le cadre des prochains chapitres. Le deuxième chapitre est une description complète du télescope à neutrinos ANTARES, un élément clé de l'équipement qui constitue la base de notre étude. Ce chapitre souligne l'importance des données expérimentales pour établir une base solide pour nos investigations. Le troisième chapitre détaille notre analyse approfondie des nuclearites dans le cadre d'ANTARES. Nous rendons compte de la recherche complète qui a abouti à la détermination d'une limite supérieure sur le flux des nuclearites utilisant l'approche Fieldman-Cousins, basée sur neuf années de données expérimentales. La quatrième et dernière partie se concentre sur le télescope KM3NeT, soulignant les contributions significatives du Maroc dans l'intégration des modules opto-électroniques et des modules optiques numériques. Une étude de la reconstruction des monopôles magnétiques au sein du détecteur ORCA est discutée dans le contexte du télescope à neutrinos KM3NeT.

Cette thèse met l'accent sur l'interaction significative entre la physique théorique et expérimentale, révélant un aperçu des théories fondamentales de l'univers. Il s'agit d'un dévouement à la recherche sans fin de connaissances, où les notions théoriques sont testées dans le creuset de la rigueur expérimentale, aboutissant à une compréhension plus profonde de l'univers et des processus qui le constituent.

---

# Acknowledgement

I am deeply grateful to my family, especially my father, mother, brother, and sisters, for their unwavering support, sacrifices, and encouragement. My father provided me with financial support, mentorship, and guidance, while my mother made countless sacrifices to ensure my success. My siblings were also a source of companionship and support. I owe everything I have achieved to my family's love and dedication.

I am sincerely grateful to my PhD supervisor, Professor Abdelilah Moussa, for his invaluable support, guidance, and expertise. He provided me with a clear vision, detailed plan, and the necessary tools to execute our project effectively. His attention to detail and thorough review helped me to improve our work, and his mentorship and leadership were instrumental in my growth as a researcher. I am deeply appreciative of his contributions to my success and will always remember his assistance. Thank you, Professor Abdelilah. I want also to express my gratitude to Professor Yahya Tayalati from Rabat for his exceptional support and guidance during a critical moment in my research. He generously shared his expertise and provided valuable insights that helped push my analysis forward. His unwavering commitment to helping me find solutions and overcome obstacles was truly inspiring. I learned a lot from him, and I am grateful for his selfless assistance. Thank you, Professor Yahya Tayalati, for your invaluable support and mentorship.

My heartfelt gratitude goes out to the members of the ANTARES collaboration, especially Professor Maurizio Spuro, Juergen Brunner, Sergio Navas, Antoine Couchner, and Vlad Popa. Their invaluable remarks and suggestions were instrumental in the success of my analysis, and their expertise, patience, and willingness to help were a constant source of motivation and inspiration. I am particularly grateful to Professor Spuro for his invaluable feedback and suggestions, which pushed me to strive for excellence in my work.

I would like to express my heartfelt gratitude to all my colleagues and professors at the Laboratory of Physics of Matter and Radiations (LPMR). It was an honor and a privilege to work alongside such a talented and inspiring group of individuals. The countless moments we shared together, both socially and scientifically, will be cherished memories for years to come.

I was fortunate to have several incredible professors during my master's years, whose knowledge, expertise, and passion for their fields of study were inspiring. They provided me with the academic foundation and technical skills necessary to succeed in my research, and their guidance and encouragement were invaluable. I deeply appreciate their unwavering support, encouragement, and mentorship.

I thank my colleagues who worked with me in the laboratory for their teamwork, collaboration, and shared passion for science, which made challenging experiments enjoyable and fulfilling. I learned a lot from their insights and perspectives, which helped me approach

my research from different angles.

In conclusion, I sincerely hope that this thesis serves as a valuable resource to readers and researchers alike. The work presented here represents a culmination of years of research, analysis, and dedication, and I believe that the results and insights gleaned from this study have important implications for the broader field. I encourage readers to engage with the findings presented in this thesis, to delve into the intricacies of the research, and to use the work presented here as a springboard for their own future investigations. Ultimately, my hope is that this thesis inspires a deeper appreciation for the beauty and complexity of the subject matter, and that it contributes to a deeper understanding of the world around us.

# Contents

<b>1 Neutrino physics and exotic particles</b>	<b>11</b>
1.1 Introduction . . . . .	11
1.2 The Standard Model of particle physics . . . . .	12
1.2.1 Definition . . . . .	12
1.2.2 The standard model particles . . . . .	13
1.2.3 Theoretical framework of the standard model . . . . .	15
1.3 Astrophysical messengers . . . . .	17
1.3.1 Electromagnetic spectrum . . . . .	18
1.3.2 Cosmic rays . . . . .	19
1.3.3 Gamma rays . . . . .	21
1.3.4 Neutrinos . . . . .	23
1.3.5 Neutrino Sources . . . . .	25
1.4 Exotic particles . . . . .	29
1.4.1 Nuclearites . . . . .	30
1.4.2 Magnetic monopoles . . . . .	35
1.4.3 Q-balls . . . . .	39
1.5 Conclusion . . . . .	42
<b>2 The ANTARES Neutrino telescope</b>	<b>43</b>
2.1 Introduction . . . . .	43
2.2 Neutrino telescopes . . . . .	44
2.3 The ANTARES detector description . . . . .	45
2.3.1 Optical Modules . . . . .	46
2.3.2 Storeys . . . . .	47
2.3.3 Lines . . . . .	47
2.4 The ANTARES data acquisition system . . . . .	48
2.5 Detector calibration . . . . .	49
2.5.1 Time calibration . . . . .	49
2.5.2 Charge calibration . . . . .	51
2.5.3 Position calibration . . . . .	52
2.5.4 ANTARES filters . . . . .	53
2.5.5 Optical background . . . . .	54
2.5.6 Atmospheric background . . . . .	55
2.6 Conclusion . . . . .	56
<b>3 Search for nuclearites with nine years of ANTARES data</b>	<b>59</b>
3.1 Analysis strategy . . . . .	59
3.2 Monte Carlo simulation of nuclearites . . . . .	60

3.2.1	Nuclearite mass threshold in ANTARES . . . . .	60
3.2.2	Run selection . . . . .	61
3.2.3	Event simulation . . . . .	62
3.2.4	Triggers and event selection . . . . .	64
3.3	Event selection and analysis . . . . .	65
3.3.1	Discrimination variables . . . . .	67
3.3.2	Selection efficiency . . . . .	68
3.3.3	Variables optimisation . . . . .	69
3.4	Analysis results . . . . .	72
3.4.1	Systematic uncertainties . . . . .	72
3.4.2	Unblinding results . . . . .	72
3.5	Conclusion . . . . .	73
<b>4</b>	<b>A Collaborative Effort: Contribution of Morocco in the construction of the KM3NeT neutrino telescope</b>	<b>75</b>
4.1	Introduction . . . . .	75
4.2	KM3NeT/ORCA design . . . . .	75
4.2.1	Digital Optical Module, the KM3NeT eyes . . . . .	77
4.2.2	Photons propagation at the ORCA site . . . . .	78
4.3	Background sources . . . . .	78
4.3.1	Bioluminescence events . . . . .	79
4.3.2	Potassium-40 decay events . . . . .	79
4.3.3	Atmospheric muons events . . . . .	80
4.4	ORCA base module integration in Oujda . . . . .	80
4.4.1	Introduction . . . . .	80
4.4.2	ORCA Base Module . . . . .	80
4.4.3	Base Module mechanics . . . . .	81
4.4.4	Base module components . . . . .	82
4.5	Integration of Digital Optical Module in Rabat . . . . .	87
4.5.1	Production strategies for the DOMs . . . . .	87
4.5.2	DOM Components . . . . .	89
4.6	Magnetic monopoles reconstruction with ORCA . . . . .	94
4.6.1	Simulation chain of MMs in ORCA . . . . .	95
4.6.2	Results on the MMs simulation . . . . .	96
4.6.3	Reconstruction of MMs . . . . .	98
4.6.4	Preliminary results on track reconstruction . . . . .	103
4.7	Conclusion . . . . .	105
<b>A</b>	<b>Feldma-Cousin approach</b>	<b>109</b>
<b>B</b>	<b>Incorporating of systematic uncertainties in limits computation</b>	<b>112</b>

# Introduction

The so-called Standard Model of particle physics has recently seen a phenomenal success in the field of particle physics. Some researchers assert that we are getting near to the limit of the physics that humans can understand after a lengthy hunt for the model's missing element, the Higgs particle, was successfully ended. Furthermore, cosmology and astrophysics have undergone a remarkable development that has been pushed by experiments and reinforced by theories and models. Nowadays, we have a "standard model of cosmology" that accurately depicts the evolution of the Universe from a very short spell following its formation to any conceivable future. In the past few years, gravitational waves have been observed. An event in which gravitational waves were associated with electromagnetic waves has been discovered, and an extragalactic source of astrophysical neutrinos has been positioned and associated with a gamma-ray emitter. The experimental field of astroparticle physics is being developed rapidly, and its revelation capacity appears to still be enormous.

However, there are currently many clouds that might obscure a modern physics revolution. The key concern is that, according to observations, we still lack a description of the fundamental components of the universe from the perspective of its energy requirements. We suspect that one of these components is a novel particle - about which we know very little - and that the other represents a new sort of energy. Recent years have seen a revolutionary phase in neutrino physics. Elementary particle physics is primarily interested in the investigation of neutrino's intrinsic properties. The discovery of the neutrino oscillation phenomenon, which revealed evidence of non-zero mass, was one of the most intriguing discoveries of the past ten years. The neutrino's ability to change flavour, while traveling through space, and interact exclusively with one of the three leptons (electron, muon or tau) is explained by neutrino oscillation. To put things in perspective, a neutrino created, for instance, in the sun that can only interact with electrons, once it reaches the earth, may have undergone a flavor change and be entirely unaffected by the electrons, interacting only with muons or taus. It has been necessary to use a variety of neutrino sources, such as the sun, stars, particle accelerators, and reactors, in order to precisely and thoroughly understand the oscillation mechanism for how one type of neutrino turns into another. A phenomenon known as neutrinoless double beta decay may be observed in order to fill in the critical gaps in the neutrino picture (searched by the GERDA, CUORE and Lucifer experiments [1–3]). In addition to confirming Ettore Majorna's initial idea, this observation will radically change how we describe elementary particles. Some fundamental aspects of the history of the cosmos can be understood, and it will also be proven that the neutrino is its own antiparticle.

Exotic (or hypothetical) particles are those that exhibit exotic properties and are predicted to exist by certain theories but have not yet been confirmed. Before being discovered by

CERN in 2012 [4, 5], the Higgs boson was only a hypothesis. The LHCb collaboration recently reported the discovery of the pentaquark, an exotic particle, on March 26, 2019 [6]. The graviton is a particle that, according to quantum gravity theories, mediates the gravitational interaction force, which has been undiscovered up to now. There are a variety of exotic particles that have been hypothesized in several theories, all of which are hypothetical until they are proven. Let us just concentrate on Strange Quark Matter (SQM), a type of matter similar to ordinary nuclear matter but that has the s quark attached to it. Bodmer originally raised the concept of collapsed nuclei in 1971 [7]. Decades later, in 1984, Edward Witten established the first structures of the SQM and revealed how they could be more stable than standard nuclear matter over a wide range of baryonic number values [8]. In literature, nuclearites are hypothetical particles thought to be formed by a bound state of SQM. The nomination is limited to SQM objects with a specified range of baryonic number; the other ranges are covered by strangelets and neutron stars. In the context of MIT's bag model, Farhi and Jaffe developed a detailed calculation for strange matter objects. The three quarks up, down, and strange are thought to be contained in this object in approximately equivalent amounts and in a stable equilibrium. A method to detect nuclearites through several detectors with diverse active volumes was discussed by Glashow and De Rujula in 1984. The authors went over the possible approach of hunting for this particle in transparent media as a black body radiation and provided the estimated luminous efficiency in highly purified water in the order of  $3 \times 10^{-5}$ .

By combining 10 years of experimental data. The ANTARES experiment has published new limits on the magnetic monopole [9]. The results, taking into account the size difference between the two detectors, are consistent with the study conducted by IceCube [10], according to the authors. A magnetic monopole is favorable to being detected inside neutrinos telescopes as a hypothetical particle owing to its relativistic speed and conformity with the majority of data processors used to trigger events. Our dissertation's primary objective is to search for nuclearites of SQM using the ANTARES detector; nevertheless, finding a track of these particles in a neutrino telescope would present a novel way to study equipment and look for other exotic particles including magnetic monopoles and Q-balls.

The field of neutrino physics and the exotic particle are covered in the first chapter of this dissertation. The Standard Model has been discussed since it is the reliable theoretical foundation of particle physics. The four fundamental forces that govern our universe and the interactions between particles are also covered. The most significant source of information about our cosmos are cosmic rays, which also offer practical resources for studying high and ultra-high energy particles that are extremely challenging or even difficult to produce in the biggest particle accelerator currently operating on Earth. Cosmic rays are briefly covered in the first chapter. We found it interesting to discuss neutrinos physics and the prospective origin of neutrino from both galactic and extra-galactic sources because our work is based on data accumulated by a neutrino telescope. We also addressed the two most challenging properties of neutrinos: the oscillation and the mass ordering. In the chapter's concluding section, we discuss exotic particles by introducing three hypothetical particles - nuclearites, magnetic monopoles, and Q-balls - that are now the subject of investigation at various research organizations.

The description of the ANTARES neutrinos telescope is the subject of the second chapter. Since this telescope is the instrument we use to conduct out our research on nuclearites signal, we consider it essential to clearly describe it. The working principle of the telescope as well as its diverse components are addressed in that chapter. The detailed data

acquisition system is followed by the events selection and trigger systems that are used for the onshore data analysis. The calibration procedures —of which we mentioned about the time, charge, and position calibration for the ANTARES telescope— are among the most critical parts of any system that measures physical parameters. Essentially, this chapter is devoted to providing a detailed description of the ANTARES neutrinos telescope.

In chapter 3, we discuss the analysis we conducted regarding the search for nuclearites in the nine years of data collected between 2009 and 2017 by the ANTARES detector. The methodology and various procedures used to carry out an ambiguous analysis are explained. The overall velocity of these exotic particles at the top of the atmosphere in their origin from space is assumed to be similar to the Galactic rotational speed ( $\beta = 10^{-3}$ ), and is taken into account in our study. Nuclearites are exotic particles that move with low speed as expected from the theoretical background. One of the biggest challenges to the research was the optical background events that were present at the detector site. However, the ability of ANTARES to trigger slow particle events passing through it was fundamental to the beginning of our investigation; without it, the search could not be carried out. No nuclearite events have been able to escape the cuts optimized by a dedicated algorithm, and ANTARES has established a flux limit for these particles.

The last chapter is devoted to KM3NeT, the currently-under-construction cubic kilometer neutrino telescope that will succeed ANTARES. Two sites are currently being built for KM3NeT; the first, KM3NeT-ORCA, is close to the ANTARES location, while the second, KM3NeT-ARCA, is being built at Capo Pasero, Italy. The second and third sections, which follow an introduction to the KM3NeT, discuss the integration work being done in Morocco’s Oujda and Rabat cities for the base modules and optical modules, respectively. The final section focuses on an ongoing effort to reconstruct the magnetic monopole track within the full ORCA detector. While there is still work to be done to enhance the fit parameters and angular resolution for the reconstructed tracks, preliminary results will be given.

# Chapter 1

## Neutrino physics and exotic particles

### 1.1 Introduction

Visible radiation is only present in a relatively narrow range of the electromagnetic spectrum. Since Galileo, who invented astronomy, this band has historically been studied using optical telescopes. Radio waves, Infrared, Ultraviolet, X-rays, and Gamma-ray spectres, however, may offer more comprehensive information about the astrophysical objects forming our Universe. Although electromagnetic spectrum observation only enables the observation of close objects, its performance is limited. This is because the matter absorbs these particles, and the interaction of high-energy gamma rays from a distant source with the cosmic microwave background reduces their energy. The cosmic microwave background impacts the monitoring of charged cosmic ray particles like protons and restricts their range to less than 100 megaparsec (Mpc) for protons with energy of about  $10^8$  TeV. Low energy proton directional information is incorrectly reconstructed because of the fluctuating galactic magnetic fields, which modify the proton's initial orientation. Because they are neutral particles and are not influenced by magnetic fields, neutrons are not deflected, but because of their extremely short lifetime, their range is severely constrained.

On the other hand, neutrinos are able to travel for much longer distances than photons and protons given that they are electrically neutral, stable, and interact very weakly with the environment. Their neutrality allows for the identification of cosmic ray sources from both galactic and extra-galactic regions without directional deflection.

As a cosmic messenger carrying information on far-off celestial objects, neutrinos are used in the field of neutrino astronomy, which is a subfield of astroparticle physics. However, due to the low cross section of a neutrino's interaction, a relatively large detector is required to detect one. Due to the recent technical advancements that have made it possible to construct detectors with such enormous volume, these particles are now being explored. Markov first suggested employing a huge natural material, such sea water or ice, as an active volume in 1960 as a prospective method for detecting high energy neutrinos. Muon neutrinos produced in astrophysical sources would navigate in the Universe and interact via charged current (CC) with the nucleons of the medium. Neutrino CC interaction would generate a muon that emits TCherenkov photons in a transparent mediums like water and ice. The visible light induced could be detected by a set of photomultiplier tubes (PMTs) placed in the medium. At high energies (above  $\sim$  TeV) muons resulting from CC interactions can travel kilometers and are almost collinear with the initial neutrinos. A

typical size of a neutrino detector should be of the order of  $Km^3$  due to the low interactions cross section.

We provide a broad review of the theoretical side of astrophysics in this chapter. We begin with a quick description of the fundamental forces and particles described in the Standard Model of particle physics. The astrophysical messengers are the subject of the next section, which concentrates on neutrinos and their sources. We conclude by providing a basic review of the exotic particles in the final section. We discuss nuclearites, magnetic monopoles, and Q-balls as three different hypothetical particles.

## 1.2 The Standard Model of particle physics

The description of matter has always intrigued mankind. Given the immense diversity of forms that matter takes on the human scale, it is tempting to think that on a smaller scale, it exists in a more fundamental or even simpler form. Rightly or wrongly, the scientific approach has allowed itself to be guided by this concept, hoping that once the fundamental elements have been obtained, it is possible to reconstruct the building up to our scale, and even beyond.

The first notion of fundamental elements comes to us from the Greeks. Nature was thought to be made up of four elements: air, fire, earth, and water. Today, the theoretical framework that describes the fundamental elements that make up matter is particle physics. Particle physics describe the fundamental constituents of matter (particles with mass) and radiation (particle without mass), as well as their interactions, within a quantum field theory called the Standard Model.

The term "standard model" refers to the high energy physics (or particle physics) Standard Model, which was created in the 1960s. This theory provides a description of the fundamental building blocks of matter known as particles. It is based on special relativity (high energies, near-light speed) and quantum physics (infinitely small, infinitely speedy). Since its creation, the model has had a lot of success, and as a result, it can now rigorously describe nature and account for all observations obtained using particle accelerators. The Higgs boson was predicted in 1964 and first observed in 2012, making its discovery the most recent achievement. This paradigm includes quantum chromodynamics and electrodynamics, which explain all interactions excepting gravity (the graviton has never been detected). The Standard Model has proven to be a theory with solid scientific foundations throughout time and via numerous experiments.

### 1.2.1 Definition

The Standard Model of particle physics is based on quantum field theory. From a mathematical point of view, quantum field theories have been formalized in the framework of Gauge theories using local symmetry groups taking the form of complex Lie groups each underlying the modeled gauge symmetries. Thus:

- Quantum electrodynamics has made it possible to describe electromagnetism within the framework of an abelian Gauge theory with the unitary group  $U(1)_Y$  (hypercharge group).
- $SU(3)_C$  is the Unitary Special mathematical group of three dimensions, quantum

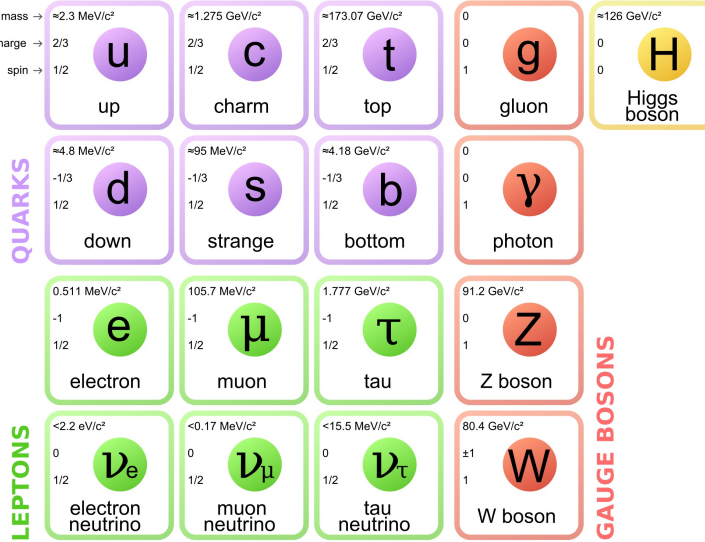


Figure 1.1: Standard Model elementary particles and their associated spin, charge and mass.

chromodynamics group (describes the strong interaction). The subscript c refers to the charge color of quarks and gluons.

- $SU(2)_L$  is the Unitary Special group of dimension 2, isospin group. It describes the weak interaction.
- The electroweak interaction is constructed with the gauge group  $SU(2) \otimes U(1)$

Finally, the standard module was formulated with the Gauge group:  $SU(3)_C \otimes SU(2)_L \otimes U(1)_Y$ . The Standard Model uses the Lagrangian formalism, in order to take maximum advantage of the symmetry that exists between the particles (in particle physics, the symmetry is maximum). Thus, each interaction is described by a Lagrangian density.

## 1.2.2 The standard model particles

To describe the world around us, physicists have indeed broken it down into small bricks: the famous elementary particles (an elementary particle is an elementary system in which we cannot distinguish elementary constituents of given mass and spin [11]). According to Wigner, an elementary system (a quantum elementary system is an object entirely characterized by its mass and its spin), in quantum physics, is an object in the quantum states transform according to an irreducible unitary representation of the Poincaré group (the group of Poincaré includes the Lorentz group and the translations of space and time), this transformation being characterized by two invariant: mass and spin [11]. Depending on the value of their spins<sup>1</sup>, elementary particles can be separated into two groups: **fermions** and **bosons** as it is shown in figure ??.

<sup>1</sup>The spin is the intrinsic angular momentum of a particle, it is a quantum concept. The angular momentum takes only discrete values in units of  $\hbar = h/2\pi$ , where  $h$  is the Planck constant. These values can be an integer or a half-integer.

### 1.2.2.1 Fermions

Fermions are the particles that make up matter as we know it (atoms, living beings, galaxies, etc.). They have a half-integer spin ( $1/2, 3/2, 5/2 \dots$ ) and obey the Fermi-Dirac statistics, hence their name of fermions. The fermions are therefore subject to the Pauli exclusion principle, which requires them not to be able to be in the same quantum state (on the same atomic orbital for example). It is this principle which, applied to electrons whose spin is equal to  $1/2$  and which are therefore fermions, places them in distinct orbits and gives the great richness of macroscopic physics. There are 12 fermions in the Standard Model: 6 quarks and 6 leptons. The leptons and quarks are grouped 2 by 2 in three generations. Each of the 12 elementary particles is associated with an anti-particle, i.e. a particle of the same mass, but with opposite quantum numbers and charge: there are therefore 24 elementary constituents of matter. Fermions and anti-fermions can annihilate each other in energy, or create a pair with enough energy. Fermions are classified into two broad categories.

- Leptons
  1. Electron  $e$  and electron neutrino  $\nu_e$  forming the first generation
  2. Muons  $\mu$  and Muons neutrino  $\nu_\mu$  forming the second generation
  3. Tau  $\tau$  and tau neutrino  $\nu_\tau$  forming the third generation

Leptons are insensitive to strong interactions, they are characterized by a non-zero leptonic number  $L$ :  $L = +1$  for the particle and  $L = -1$  for its anti-particle. The lepton number is conserved in all reactions, this mean that the number of leptons minus the number of anti-leptons is constant in the universe. We realized that the muon neutrino differs from the electron neutrino and it was then necessary to differentiate the leptonic number: electronic leptonic number, muonic leptonic number and tauonic leptonic number. These lepton numbers are each conserved separately [5, 6].

- Quarks
  1. Up  $u$  and down  $d$  quarks for the first generation.
  2. Charm  $c$  and strange  $s$  quarks for the second generation.
  3. Top  $t$  and bottom  $b$  quarks for the third generation.

Quarks are the fundamental particles that form nuclear matter, there are 6 flavors of known quarks; like leptons, there are 3 generations of quarks:

1. Up  $u$  and down  $d$  quarks for the first generation.
2. Charm  $c$  and strange  $s$  quarks for the second generation.
3. Top  $t$  and bottom  $b$  quarks for the third generation.

Quarks are strongly interacting particles (sensitive to the strong interaction), they have fractional electric charges and they have a colored charge. The quarks, which cannot exist in a free state, assemble and form hadrons. There are two types of (observed) hadrons:

- **Baryons** meaning "heavy", are combinations of three quarks: e.g. the proton is formed of two quarks up and one down ( $uud$ ), and the neutron is formed of one quark up and two down ( $udd$ ). Baryons, like leptons, are characterized by a non-zero baryon number  $B$  ( $B = +1$  for the particle (Proton, neutron, etc.) and  $B = -1$  for the antiparticle (Antiproton, antineutron, etc. )) [5, 6]. Baryon number is conserved in reactions. Now it is thought that the baryonic

Generation	Fermions			
	Leptons		Quarks	
	Symbol	Mass (GeV)	Symbol	Mass (GeV)
1 <sup>st</sup> Generation	$e$	$3.3 \times 10^{-3}$	$u$	$(1.55 - 3.3) \times 10^{-3}$
	$\nu_e$	$< 2 \times 10^{-9}$	$d$	$(3 - 6) \times 10^{-3}$
2 <sup>nd</sup> Generation	$\mu$	$105.7 \times 10^{-3}$	$c$	1.27
	$\nu_\mu$	$< 0.19 \times 10^{-6}$	$s$	$(70 - 130) \times 10^{-3}$
2 <sup>nd</sup> Generation	$\tau$	1.77	$t$	171.2
	$\nu_\tau$	$< 18.2 \times 10^{-6}$	$b$	$(4.2 - 4.7)$

Table 1.1: Standard model fermions and their generation of flavors. Each particle has its own antiparticle with an inverse charge (see Fig. ??).

Standard model bosons				
particle	Charge	Spin	Function	
Jauge bosons				
$g_i$	$i = 1 \dots 8$	0	1	Strong interaction mediator
	$W^\pm$	$\pm 1$	1	Weak interaction mediator
	$Z^0$	0	1	Weak interaction mediator
	$\gamma$	0	1	Electromagnetic interaction mediator
Higgs boson				
$H$	0	0	Mass generator	

Table 1.2: Bosons of the standard model and their charge, spin and fonction.

number  $B$  is veiled because of the unstability of the protons (could decay with a lifetime of the order of 1032 years), and the same for the lepton number  $L$ .

- **Mesons:** mesons are constituted by a pair of quark and anti-quark: for example, pion  $\pi^+$  ( $u\bar{d}$ ) and kaon  $K^+$  ( $u\bar{s}$ ) are type of measons.

### 1.2.2.2 Bosons

Bosons are the particles that guarantee the interactions between the fermions. They are the vectors of three among four main forces that exist in nature (weak, strong, electromagnetic forces and the gravitational force which is not described within the framework of the Standard Model). Bosons have an integer spin (1, 2, 3 ...) and obey the Bose-Einstein statistics [7]. They are the mediators (also called messengers or vectors) of the fundamental interactions: the photon  $\gamma$  (mediator of the electromagnetic interaction), gluon  $g$  (mediator of the strong nuclear interaction eight in number), and the bosons  $W^+$ ,  $W^-$  and  $Z_0$  (mediator of the weak interaction). So the exchange of a boson between two elementary particles constitutes an interaction.

### 1.2.3 Theoretical framework of the standard model

The Standard Model unifies the two physical theories: electroweak model and quantum chromodynamics which are based on other physical theories. The hierarchy in figure ?? shows the physical theoretical framework of the standard module.

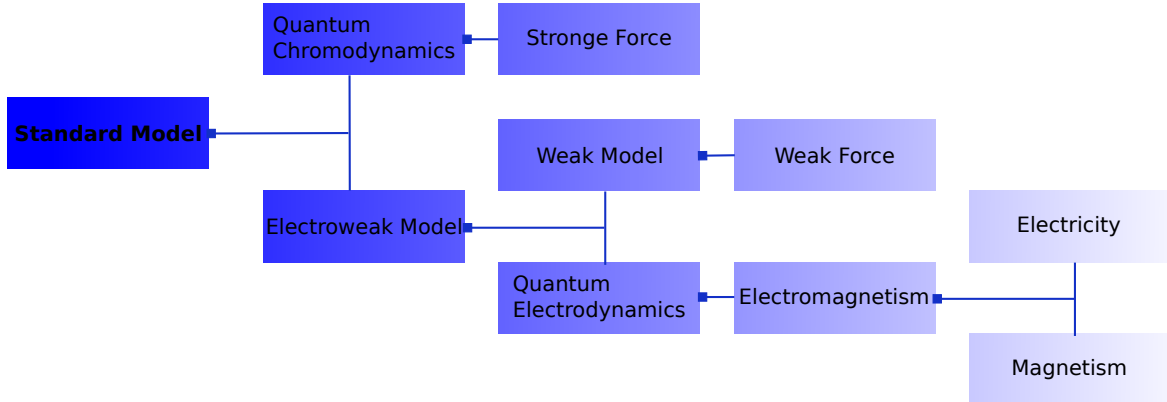


Figure 1.2: theoretical hierarchy of the Standard Model.

### 1.2.3.1 Quantum electrodynamics

The quark model is a great success. It made it possible to explain in an elegant way the proliferation of new particles ( $\pi^{0/+/+}, K, \eta, \dots$ ) discovered in the 1940s. However, the discovery of  $\Delta^{++}$  ( $uuu$ ) In 1951, this casts doubt on the established model. Indeed, this hadron is composed of three quarks  $u$ . The Pauli exclusion principle forbids the fermions to be in the same quantum state.  $\Delta^{++}$  is necessarily composed of two  $u$  of the same spin, which is not allowed by the Pauli exclusion principle since quarks are fermions.

The solution to this problem is to introduce, within the framework of a new quantum theory called quantum chromodynamics or QCD that describes the strong interaction, a new quantum number, similar to the electric charge: the color charge. A quark can therefore exist in three different colors: red ( $r$ ), green ( $g$ ) or blue ( $b$ ), and their anti-colors ( $\bar{r}, \bar{g}, \bar{b}$ ). The gluon which is the mediator of the strong interaction carries both the color and its anti-color, so we might think that there should be  $3 \times 3$  combinations of gluons. However one of these nine is colorless, so we only have 8 orthogonal gluon states [10].

The QCD, therefore, describes the strong force which makes it possible to understand the interaction between quarks and gluons as well as the cohesion of the atomic nucleus. It was proposed by H. David, Politzer, David Gross and Frank Wilczek in 1973 to understand the structure of hadrons (baryons and mesons). The term "chromodynamics" comes from the Greek word "chrôma" which means color. QCD describes the strong interaction as a particular gauge group on the color of quarks, named  $SU(3)$  gauge group (special unitary group of dimension 3) since each quark exists in three different colors. QCD has predicted many effects, such as quark confinement and fermions condensates.

### 1.2.3.2 Electroweak model

This model is the result of the unification of quantum electrodynamics (QED) which is none other than electromagnetism in quantum formulation and the weak nuclear force. It was developed during the 1960s by Sheldon Glashow, Abdus Salam and Steven Weinberg (Nobel Prize in Physics in 1979) [8]. It is a quantum field theory based on the simplest gauge group  $SU(2)_L \otimes U(1)_Y$  where the index  $Y$  designates the weak hypercharge. In order to differentiate between  $U(1)_Y$  and the group  $U(1)_Q$  of the simple electrodynamic model, and the subscript  $L$  indicates that this group acts only on left *isospin* fermions. Indeed, the  $U(1)_Q$  symmetry of QED does not commute with the  $SU(2)_L$  gauge group of

weak interactions. On the other hand, one can introduce a symmetry  $U(1)_Y$ , called weak hypercharge  $y$ , compatible with  $SU(2)_L$ , and such that by mixing with the third component of  $SU(2)_L$  (weak isospin  $t_3$ ), we find the electric charge  $q$  (or  $Q$ ) by the so-called Gell-Mann and Nishijima equation [11]:

$$q = t_3 + \frac{y}{2} \quad (1.1)$$

This model is able to predict the masses of bosons at 80 GeV for the  $W^\pm$  and at 90 GeV for the  $Z^0$ , the vector bosons of the weak force, while the photon, vector of the electromagnetic interaction at zero mass [8]. These mass differences explain the considerable difference in the behavior of these low-energy interactions. When the energy scale of the observations is lower than the electroweak scale, an asymmetry indeed appears between electromagnetism and weak interaction via a spontaneous breaking of the electroweak symmetry generated by the Higgs mechanism.

#### 1.2.3.3 Higgs mechanism

After having brought together the three forces electromagnetic, weak and strong, in the same theory which is called the standard model, the equations of this model which rely on the notion of symmetry require that these three forces formed only one at the first moments of the Universe: the electronuclear force. But this theory had a considerable flaw. It was necessary at all costs that the mass of the particles, and more particularly of the bosons, be zero to respect the underlying mathematical formalism. However, this is not the case: the intermediate bosons do indeed have mass. And this is important: several hundred times that of the proton. Two possibilities then presented themselves to theoreticians: either to discard the theory entirely or to contemplate that, up to that point, we had not fully grasped the true meaning of mass.

In the early 1960s, three researchers, the Belgian physicists François Englert and Robert Brout, and independently, the British physicist Peter Higgs, chose this second path and postulated, almost simultaneously, a mechanism to save the Standard Model: *the mechanism of Higgs or Brout-Englert-Higgs mechanism*, by postulating the existence of a new boson, the Higgs boson. This particle would be present everywhere in the Universe and would form a uniform field. It is these bosons that would give their mass to the other particles. The more a particle interacts with the Higgs field (Higgs bosons), the heavier it is [11].

## 1.3 Astrophysical messengers

Astrophysical messengers encompass a diverse range of particles and radiations generated by celestial objects and events, traversing through the cosmos to reach our planet. These messengers serve as crucial carriers of insights into the universe's essence, its chronological development, and the behaviors of its fundamental constituents.

Detecting these astrophysical messengers requires sophisticated instruments and techniques, many of which are based on the principles of particle physics and astrophysics. Some of the most important techniques include:

1. **Electromagnetic radiation:** This includes visible light, radio waves, X-rays, and gamma rays, among others. These types of radiation can be detected using telescopes and other instruments that are designed to capture different wavelengths of the electromagnetic spectrum.
2. **Cosmic rays:** These are high-energy particles that originate from space and can be detected using specialized detectors on Earth. The Pierre Auger Observatory in Argentina and the Telescope Array in Utah are two of the largest cosmic ray detectors in the world.
3. **Gamma rays:** These high-energy photons are produced by cosmic phenomena such as supernovae, black holes, and active galactic nuclei. The Fermi Gamma-ray Space Telescope has detected thousands of gamma-ray sources in the sky.
4. **Gravitational waves:** These are ripples in the fabric of space-time that are produced by the most violent and energetic events in the universe, such as the collision of black holes or neutron stars. These waves can be detected using extremely sensitive instruments like the Laser Interferometer Gravitational-Wave Observatory (LIGO). LIGO made history in 2015 by detecting the first gravitational waves, which were produced by the collision of two black holes.
5. **Neutrinos:** These are tiny particles that are produced by nuclear reactions in stars and other cosmic events. They are notoriously difficult to detect, but large-scale detectors like IceCube in Antarctica have been built to capture these elusive particles. These ghostly particles can be detected using large detectors like ANTARES, KM3NeT and IceCube, which are located deep beneath the water and ice. In 2017, IceCube detected a high-energy neutrino that was traced back to a blazar, a type of active galactic nuclei.

Astrophysical messengers are critical to our understanding of the universe, and the development of increasingly sensitive detectors and techniques has allowed us to study them in ever-greater detail. From gamma rays to cosmic rays, and from gravitational waves to neutrinos, these messengers provide a unique and fascinating window into the cosmos. In the following, we will address some Astrophysical messengers in more details.

### 1.3.1 Electromagnetic spectrum

In the cosmos, energy comes in a variety of forms. Radiant energy, or electromagnetic radiation as it is known in science, is what the sun emits. This energy is generated at the sun's core through nuclear processes, and it radiates from its surface in waves of various sizes. Our eyes can't see the lowest and longest wavelengths, but the middle range is what we can see and call sunshine (see Fig. ??). These visible wavelengths are where the sun releases the majority of its energy.

Every substance has kinetic energy, which manifests as atom or molecule vibrations. Radiation is produced by the vibrations. The term for all of the many radiation types is the electromagnetic (EM) spectrum. Energy that propagates as it moves is known as electromagnetic radiation. Two examples of electromagnetic radiation are visible light radiation from a bulb in a home or radio wave radiation from a radio station. Microwaves, infrared, ultraviolet, X-rays, and gamma rays are more types of EM radiation. Higher energy radiation is produced by hotter, more energetic objects and events than by cold

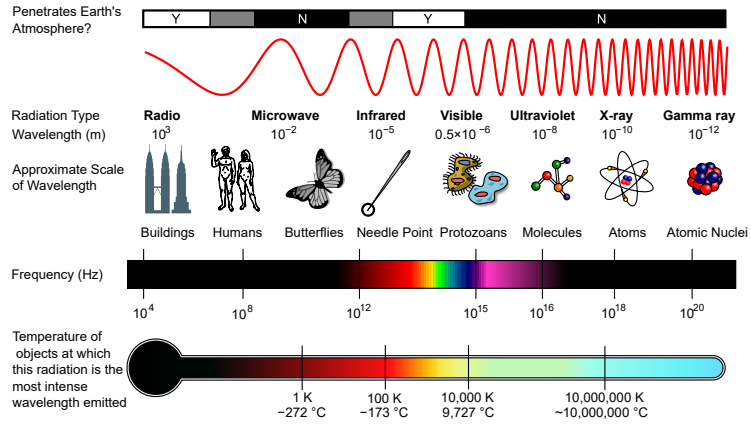


Figure 1.3: Properties of the electromagnetic spectrum.

ones. High-energy radiation like X-rays and gamma rays are only produced by extremely hot objects or particles travelling at extremely high speeds.

The length (wavelength) of a wave is expressed in meters. Moreover, their frequency or the amount of waves that pass a space location each second are used to quantify them. The length of electromagnetic waves ranges from very small (billions of a centimeter) to very large waves (hundreds of kilometers). It's crucial to keep in mind that the only physical characteristics of electromagnetic radiation that vary are its wavelength and frequency. In every other way, they are the same.

### 1.3.2 Cosmic rays

Victor Franz Hess discovered cosmic rays (CRs) in 1912 after noticing that the flux of this mysterious radiation increases as he ascends in altitude (in a balloon flight) [12]. This contradicted the concept that these radiations were created in the Earth's crust and proves the cosmic origin of these radiations. CRs are non-photon particles fall on Earth in an isotropic manner all the time. *Primary* CRs are energetic elementary particles accelerated by astrophysical processes, such as protons, which are the dominant particle (89%), helium (10%), carbon, oxygen, as well as other heavy nuclei synthesized in stars (around 1%) [13]. While particles produced by the interaction of primary CRs, mainly protons, with the interstellar gas are referred to as *secondary* particles, lithium and beryllium nuclei are examples, as are antiprotons and positrons, which might also be primaries, secondaries may collide again or decay into other particles that could initiate cascades via pair production, bremsstrahlung, and other interactions generating photons, muons, electrons, and neutrinos. The CRs that reach the Earth's atmosphere are made up of all stable charged particles and nuclei with lifetimes of  $10^6$  years or more. The atmosphere serves as a shield for the Earth from CRs, with over 20 absorption lengths absorbing a considerable amount of radiation. However, because of the relativistic temporal expansion of muons and the low strength of neutrinos interaction, these particles reach the Earth, causing a significant flux. Every second, millions of muons and neutrinos pass through our body.

A significant amount of the CRs particles that fall on Earth's upper atmosphere originates from outside the solar system, and they are affected by the solar wind, which interrupts galactic CRs and destroys low-energy particles. In our solar system, solar flares are also a source of CRs. Solar activity and the intensity of CRs below 10 GeV exhibit a significant anti-correlation. Furthermore, the geomagnetic field influences low-energy CRs, meaning

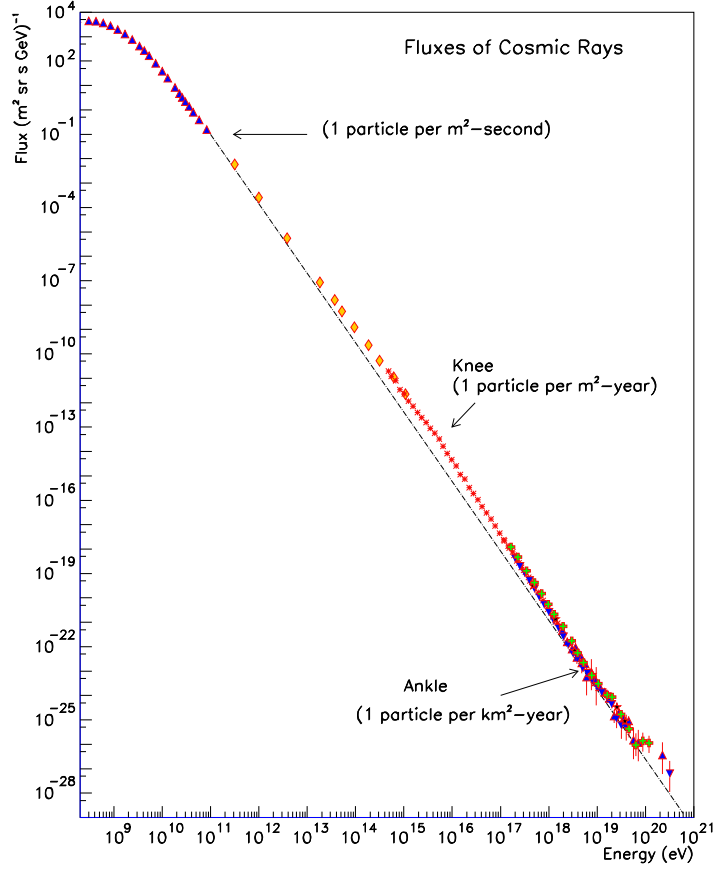


Figure 1.4: The cosmic rays energy spectrum [14]. The following experiments collect data: LEAP, Proton, Akeno, AGASA, Fly's Eye, Haverah Park, and Yakutsk.

that time and place limits the intensity of CRs components.

The energy spectrum of cosmic radiation, which covers more than 23 orders of magnitude in flux, is perhaps its most remarkable feature. Figure ?? illustrates the spectrum as measured on Earth. Three power laws, a function of energy such as  $Flux \propto E^{-\gamma}$  with unique spectral indices  $\gamma$  may be used to characterize this curve. The spectrum follows a nearly perfect power law with a spectral index of 2.7 up to  $5 \times 10^{15}$  eV, then there is a break in the slope dubbed the "knee," when the logarithmic slope goes to 3. Finally, about  $10^{18}$  eV, the slope drops and is determined to be around 2.8. The regularity of the flux over such broad energy ranges implies that this radiation is linked with global phenomenology.

The cosmic rays are the most abundant between  $\sim 10^8$  eV and  $\sim 10^{10}$  eV, and they play an important role in the interstellar medium's equilibrium. However, these cosmic rays are strongly affected by the magnetic fields of the solar winds, and their galactic transit is driven by a variety of poorly understood processes, including acceleration, convection, re-acceleration, absorption, and diffusion/escapement. At higher energies, above  $10^{11}$  eV, only scattering events caused by random irregularities in the galactic magnetic field dominate cosmic ray propagation conditions. The composition of charged nuclear cosmic rays between  $\sim 10^{12}$  eV and  $\sim 10^{15}$  eV is rather well understood, thanks to direct detection of nuclei by satellites and sounding balloons. Protons account for 89% of nuclei, helium nuclei for 10%, and the remaining is divided among the heavier nuclei.

The "knee" slope break around  $10^{15}$  eV in Fig. ?? is still poorly understood. This behavior

is explained by the maximum energy limit of shock wave charged particles in supernova remnants. This limitation is determined by the nucleus's charge  $Z$  and can reach  $10^{15}$  eV for the heaviest nuclei:

$$E_{max}(Z) \simeq Z \times 100 \text{ TeV.} \quad (1.2)$$

This maximal energy, however, is not enough to explain the spectral index of 3 seen after the "knee." This signifies the addition of new components, such as extragalactic cosmic rays, a novel interaction channel, and/or the presence of an astrophysical source in our proximity, which contributes to this region of the spectrum. A second break in slope is observed in the spectrum at ultra-high energy (above  $10^{18}$  eV), which is commonly referred to as the "peg." Cosmic rays can no longer be confined in the Galaxy beyond  $10^{19}$  eV since their Larmor radius has become larger than the radius of the Galaxy ( $R_{Galaxy} \simeq 12$  kpc). The "ankle" can be explained by the conversion of cosmic radiation from a galactic origin to an extragalactic origin.

Finally, for cosmic rays with energies more than  $10^{20}$  eV, the weak deflection of their direction caused by the galactic and extragalactic magnetic fields enables astronomy to occur. However, above  $10^{19}$  eV, a new restriction arises: the Greisen, Zatsepin, and Kuzmin (GZK) effect [15, 16], which predicts a very large interaction cross section between the diffuse cosmological microwave background (CMB) and these high energy particles:

$$p + \gamma_{CMB} \rightarrow \Delta \rightarrow \pi + p. \quad (1.3)$$

As a result, the mean free path of cosmic rays decreases with energy (see Fig. ??), and a drop in cosmic ray flux is predicted above  $10^{19}$  eV. The AUGER experiment from  $4 \times 10^{19}$  eV did, in fact, confirm a progressive cutoff [17].

There are two types of hypotheses that seek to explain the mechanics of cosmic ray acceleration up to very high energy (beyond  $10^{15-18}$  eV):

- "Bottom-up" models, which rely on the acceleration of charged particles in particularly active objects and are commonly described by the first and second order Fermi models [18].
- "Top-down" theories that are based on physics beyond the standard model and assume the presence of super-massive particles whose disintegration products might be the high-energy particles observed [19, 20].

However, Auger's [21] discovery of an anisotropy in the spectrum of very high energy cosmic rays ( $> 6 \cdot 10^{19}$  eV), which is correlated with the presence of active galactic nuclei at distances less than 75 Mpc and appears to agree with the expected GZK cutoff (about 100 Mpc at this energy), It instills doubt in the top-down type models.

### 1.3.3 Gamma rays

Astronomy is a relatively new discipline, having emerged in the 1970s. Gamma astronomy is the study of photons with energies higher than  $10^5$  eV and covering more than 9 orders

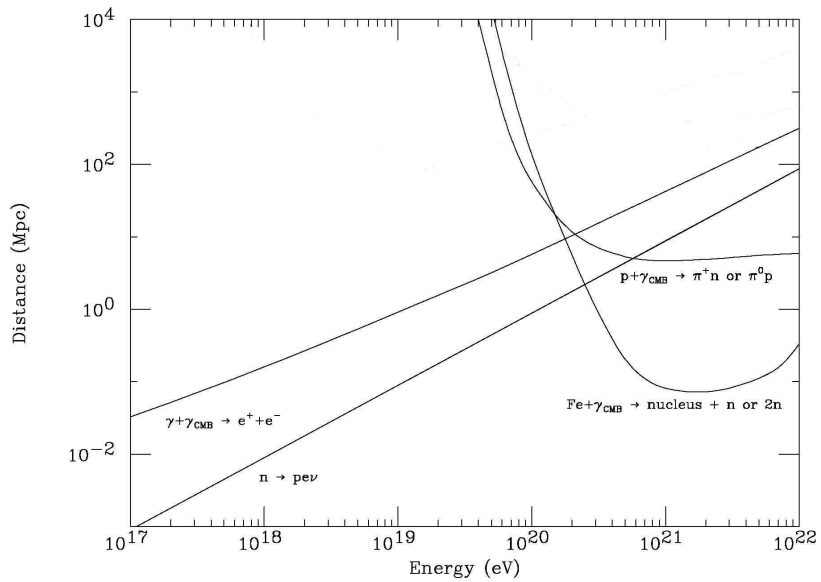


Figure 1.5: Cosmic rays mean free path.

of magnitude. Its research is driven by a knowledge of the Universe's violent events. The border with X-ray astronomy is rather ambiguous, with detection procedures for "soft" rays being the same as those used for "hard" X-rays. Non-thermal processes produce  $\gamma$ -rays, which are typically connected with particle acceleration to ultra-relativistic velocities.

The challenge in detecting  $\gamma$ -rays is that their wavelength is smaller than the inter-atomic distance, therefore they cannot be focused. Furthermore, the sources of emissions are changing, necessitating continual monitoring. Finally, as photon energy increases, their flux decreases. As a result, new detection methods similar to those employed in particle physics were required. Two detecting approaches can be distinguished depending on the point of view:

- **From space:** The use of satellites enables the employment of simpler detection techniques and the prevention of the effects of cosmic ray interaction with the atmosphere. Detection relies on the photoelectric effect, the Compton effect, and the production of electron-positron pairs, depending on the energy of the incident photons, up to around  $10^8$  eV. The FERMI-GLAST telescope [22], which was launched in 2008, can probe energies as high as  $> 10^{10}$  eV and is currently the most sensitive onboard telescope in the field of high energies.
- **From the Earth:** To investigate a higher energy domain, starting at  $\sim 10^8$  eV, the search for  $\gamma$  will need considerably bigger detection surfaces, which will be challenging to achieve in space. Gamma rays, like extremely high energy cosmic rays, will be observable on Earth due to their interaction with the Earth's atmosphere, which will result in showers of relativistic particles producing TCherenkov light, which will be detectable on the ground. The HESS experiment [23], for example, employs this detection approach and has already discovered several sources of very high energy

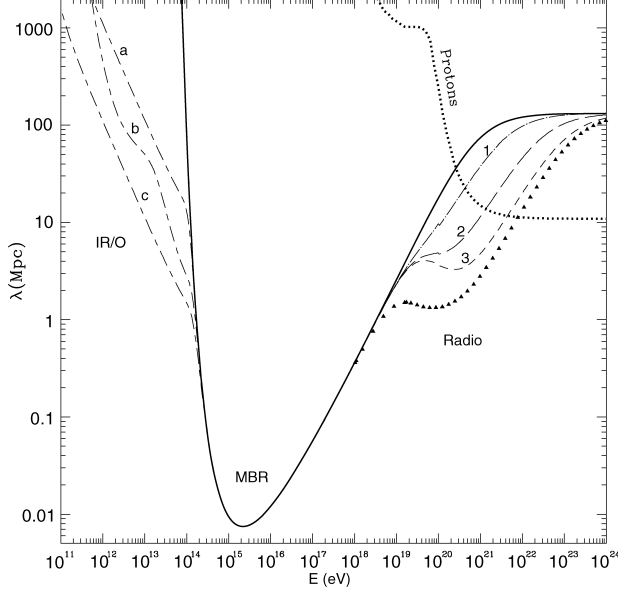


Figure 1.6: Pair-production photon mean free path as a function of beam photon energy.

gamma rays.

Despite big improvements in detection, limits emerge owing to photon intrinsic properties. Because of their powerful interactions with matter, photons will be quickly absorbed by interstellar dust clouds. Furthermore, at  $10^{12}$  eV, as shown in Fig. ??, they will interact with diffused electromagnetic radiation, radio, microwave, and infrared via a pair production process. Therefore, photons with energies of the order of  $10^{15}$  eV will be extremely unlikely to be detected from extragalactic sources.

With the development of the discipline, numerous sources of  $\gamma$ -rays with energy more than the GeV have been detected. However, without the observation of further messengers, it is impossible to identify whether these sources are charged nuclear cosmic radiation accelerators. Indeed, the production of  $\gamma$ -rays is non-thermal and may be divided into two distinct types:

- Leptonic processes: It rely on the inverse Compton (IC) scattering mechanism, in which electrons accelerated in a source give up a significant portion of their energy via scattering with photons [24].
- Hadronic processes: It include the interaction of protons with lower energy particles such as  $\gamma$  photons or nuclei, resulting in mesons (particularly pions  $\pi$ ) or neutrons. The  $\pi^0$  decays into gamma rays [25].

Thus, knowing whether nuclear cosmic rays are accelerated within the sources of nuclear cosmic rays will be achievable by identifying the leptonic or hadronic origin of  $\gamma$ -rays for a specific source. The observation of high energy neutrinos from these sources allows for this distinction.

### 1.3.4 Neutrinos

In 1930, researches on beta decay showed a continuous distribution of electron energy, posing an energy-momentum and conservation angular momentum problem. To "preserve" these fundamental principles, Wolfgang Pauli proposed the neutron, an electrically neutral

particle with spin 1/2 that interacts extremely weakly with matter and has practically no mass. After James Chadwick found the "actual" neutron in 1932, Enrico Fermi dubbed it the neutrino and included it into his theory of beta decay, which would later become the theory of weak interaction.

Before being able to detect the first neutrino, scientists had to wait several years. Frederick Reines and Clyde L. Cowen discovered the electron neutrino in their effort to identify the reverse beta reaction  $\nu_e + p \rightarrow n + e^+$  in 1953. This conclusion was later verified in 1956 [26], and at the same time, Lee and Yang found one of the most interesting properties of neutrinos, the low parity violation of the interaction [27]. Existing neutrinos and antineutrinos have either left-handed or right-handed chirality, which refers to the handedness of a particle's spin relative to its direction of motion. In other words, it describes the orientation of the particle's spin with respect to its momentum vector. A particle with left-handed chirality has its spin pointing in the opposite direction of its momentum vector, while a particle with right-handed chirality has its spin pointing in the same direction as its momentum vector. Chirality is an important property in the study of subatomic particles and their interactions, as it can affect the way particles interact with each other and with external fields. The lack of right, respectively left, chirality for neutrinos and antineutrinos has been proposed to be due to their zero mass, which suppresses their weak isospin singlet component.

L.M. Lederman, M. Schwartz, J. Steinberger, and their coworkers [28] proved the presence of a second neutrino, connected with the muon, in 1962, by the decay of pions released in the impact of a proton beam on a beryllium target. Finally, after M. Perl discovered the lepton near the SPEAR collider in 1975 [29], it became essential to assume the presence of a third flavor of neutrinos, tau neutrinos, which were found in 2000 by the DONUT experiment from neutrinos originating from tau decay [30].

In the Standard Model, there are two types of neutrinos: Dirac neutrinos and Majorana neutrinos. This hypothesis violates the conservation of the lepton number, which is one of the Standard Model's most mysterious aspects because it is supported by no underlying theory. Since the discovery of neutrino oscillations, scientists have had to reassess the existence of these particles' mass. Indeed, the fact that neutrinos, Dirac, or Majorana, are particles with non-zero mass leads to the idea of neutrino flavor mixing. In fact, neutrinos may change flavour or "oscillate," which explains the decrease in solar electron neutrino flux and the absence of atmospheric muon neutrino flux. The reason for this oscillation among neutrino eigenstates is that the flavour states induced by the weak interaction  $\nu_\alpha$  are not eigenstates of the mass matrix  $\nu_i$  but rather a linear composition of them:

$$|\nu_\alpha\rangle = \sum_{i=1}^3 U_{\alpha i} |\nu_i\rangle \quad (1.4)$$

where  $\alpha = e, \mu, \tau$  indicate neutrino flavours and  $i = 1, 2, 3$  denote mass eigenstates. Once the temporal evolution is included, the Equation 1.4 yields

$$|\nu_\alpha(t)\rangle = \sum_{i=1}^3 U_{\alpha i} |\nu_i(t)\rangle = \sum_{i=1}^3 U_{\alpha i} e^{-iE_i t} |\nu_i\rangle. \quad (1.5)$$

The oscillation probability may be calculated on the approximation that oscillations between just two states dominate [31]

$$P_{\alpha\beta} = \sin^2(2\theta) \sin^2 \left( 1.27 \frac{L}{E} \Delta m^2 \right) \quad (1.6)$$

where  $\Delta m^2 = (m_\alpha^2 - m_\beta^2)$  in eV<sup>2</sup>,  $L$  is the distance in metres between the neutrino source and detector, and  $E$  is the neutrino energy in MeV. According to Equation ??, at least two of the neutrino states should have mass since  $\Delta m^2$  simply couldn't be zero. The probability of oscillation is based on two fundamental unknowns,  $\theta$  and  $\Delta m^2$ . There are three mixing angles  $\theta_{12}$ ,  $\theta_{13}$  and  $\theta_{23}$ , a CP-violating phase  $\delta$ , and two independent squared mass differences,  $\Delta m_{12}^2$  and  $\Delta m_{23}^2$  in the three-flavour approach of neutrino oscillations. The Pontecorvo-MakiNakagawa-Sakata (PMNS) mixing matrix may be written as [31]

$$U = \begin{pmatrix} 1 & 0 & 0 \\ 0 & c_{23} & s_{23} \\ 0 & -s_{23} & c_{23} \end{pmatrix} \begin{pmatrix} c_{13} & 0 & s_{13}e^{-i\delta} \\ 0 & 1 & 0 \\ -s_{13}e^{i\delta} & 0 & c_{13} \end{pmatrix} \begin{pmatrix} c_{12} & s_{12} & 0 \\ -s_{12} & c_{12} & 0 \\ 0 & 0 & 1 \end{pmatrix}, \quad (1.7)$$

where  $c_{ij} \equiv \cos \theta_{ij}$  and  $s_{ij} \equiv \sin \theta_{ij}$ . The first matrix may be investigated using atmospheric neutrinos and LBL (Long-Base-Line) accelerators, the second using SBL (Short-Base-Line) reactors, and the third using solar neutrinos and LBL reactors. The parameter  $\delta$  is predicted to be tiny, and the Daya Bay experiment [32] shows that  $\sin^2(2\theta_{13}) = 0.092 \pm 0.017$  with a statistical inference of  $5.2\sigma$ . The center matrix in Eq. ?? reduces to the identity matrix in the limit when  $\theta_{13}$  and  $\delta$  are zero, and the experimental situation may be described by two decoupled oscillations. The first decoupled oscillation,  $\nu_e \rightarrow \nu_\mu$ , is responsible for solar neutrino oscillations [31], whereas the second,  $\nu_\mu \rightarrow \nu_\tau$ , is responsible for atmospheric neutrino oscillations [31]. The removal of one neutrino flavour, the matching arrival of neutrinos of a different flavour, and evidence for an oscillating pattern constitute the experimental signature for neutrino oscillations.

The "Bottom-Up" production mechanisms of neutrinos in the sources are of the hadronic type. They require the decay of mesons produced by the interaction of protons with nuclei or photons. Thus, the detection of neutrinos, and of an optical counterpart, coming from a source, will make it possible to constrain the models of acceleration of cosmic rays of very high energies. Moreover, the detection of neutrinos without any counterpart, could be attributed to a new class of as yet unknown source. However, the predicted neutrino fluxes from  $\gamma$ -ray observations are very low [33], and a very large detection volume is required to be able to start to do astronomy. Because of its stability, neutrality, and relatively weak interaction with matter, the neutrino appears to be the best channel of information, allowing it to escape from the source's core without being impacted.

### 1.3.5 Neutrino Sources

This section examines the many types of neutrino sources. Neutrinos are created in a variety of environments, including stars, supernovae, and the Big Bang. They are produced as a result of gamma ray bursts and cosmic ray interactions in the atmosphere. The earth produces a large number of them as radioactive elements (mainly Uranium and Thorium

decay), and humans produce them in nuclear reactors and accelerators. Their energy ranges from micro electron-volts for neutrinos left over from the Big Bang to peta electron-volts for neutrinos formed in the universe's furious gamma-ray bursts and Z-bursts.

Neutrino sources can be categorized into two groups: one originating from outside our galaxy (extragalactic sources) and the other arising within our galaxy (galactic sources).

### 1.3.5.1 Extra-Galactic neutrinos sources

Extra-Galactic objects are the Universe's most energetic sources. We will discuss Gamma-Ray Bursts (GRBs) and Active Galactic Nuclei (AGNs), which are now known as gamma-ray emitters and potentially neutrino sources. Neutrinos have the advantage of being the only particles susceptible of escaping from these source dense cores (black hole typically). Because of the extremely high optical depth within, photons are not able to escape.

**1.3.5.1.1 Gamma-Ray Bursts - GRBs** *Gamma-ray bursts* (GRBs), are brief and extremely intense emissions of gamma rays of extragalactic origin. The first were observed accidentally in 1967 by the American satellites Vela, intended to monitor nuclear tests on Earth, and were attributed from 1973 to violent cosmic phenomena [34]. GRBs are classified into two types, short bursts, whose main emission (called prompt emission) is less than 2s, and long bursts, lasting from 2s to several hundred of seconds [35]. Their origin is a mystery, they could come from the explosion of a supermassive supernova or appear after the collision of two objects, such as neutron stars or black holes.

GRBs are characterized by three phases (as seen in Fig. ??):

- A few hours before the prompt emission, no light is visible, the medium being supposed to be opaque to the photons, and the acceleration of hadrons within them in interaction with the photons, could produce a detectable flux of neutrinos.
- During the prompt emission, an intense luminosity in the range of gamma rays is emitted, and the interaction of ultra-relativistic protons would induce the production of neutrinos
- After the prompt emission, during a period that can range from a few hours to several weeks called afterglow, photons of various wavelengths, ranging from the gamma ray domain to the radio domain, are emitted, and neutrinos could be produced in this phase.

The *Fireball model* is the reference framework used to research for GRBs, which is explained using total energy released and the variable time of the GRB during the collision [36]. As a result, shock wave are emitted and travel at near to the speed of light along the stars. By converting entropy into kinetic energy, these shock waves or fireballs grow with constant energy. In addition to the fireball, two jets are emitted in opposite directions in the accretion disk's hemispheres, and the matter is accelerated in the jets progressively reaching higher velocities, producing shells with different velocities. The interaction of shells with the external medium, or shell-to-shell coupling, results in the conversion of kinetic energy into internal energy, which is translated into  $\gamma$ -ray radiation or energy transference to baryons via a baryon-to-photon coupling.

**1.3.5.1.2 Active Galactic Nuclei - AGNs** Because of their extreme luminosity in the radio domain, *active galactic nuclei* were identified in 1963. These objects are often

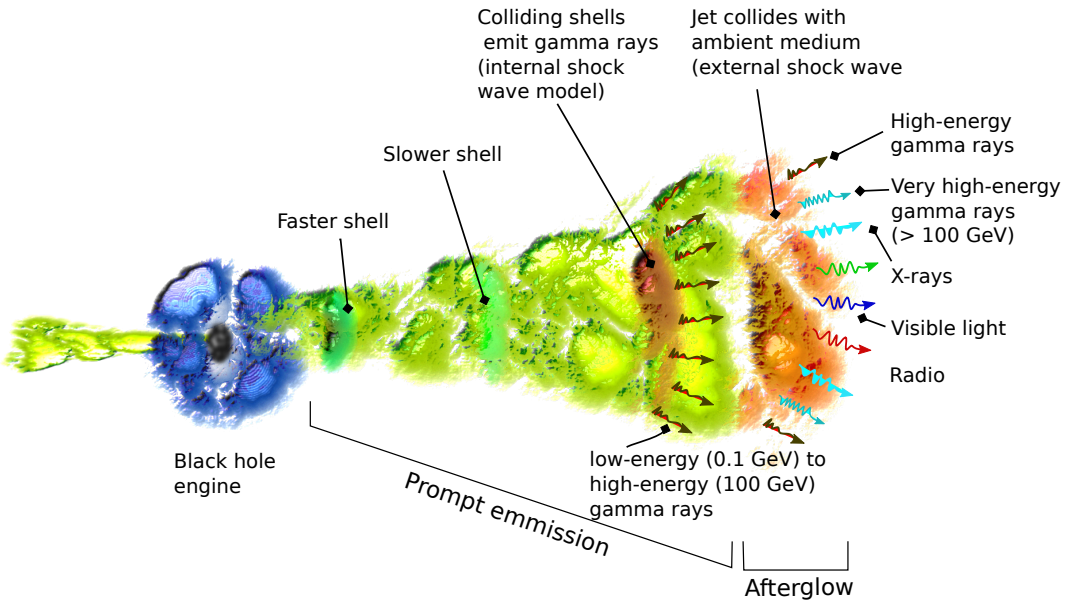


Figure 1.7: Schematic description of the fireball model of GRBs.

found in galaxie cores, and their emission covers approximately the whole electromagnetic spectrum. AGNs would be made up of a supermassive black hole (more than  $10^6$  solar masses) surrounded by a spinning matter accretion disk. Two jets of relativistic particles are released perpendicular to this accretion disk, observable in radio astronomy as enormous lobes (Fig. ??). Although leptonic models appear to be better equipped to explain gamma ray emissions, especially during extremely active and changeable states, other theories imply that the emissions are caused by hadrons. If protons are present in the jets, gamma rays and neutrinos will be produced via  $p - p$  [37, 38] and  $p - \gamma$  [39, 40] interactions if their density is high enough.

Furthermore, gamma ray emissions might be caused by synchrotron radiation released directly by the protons present, which must be accelerated to very high energies on the order of  $10^{19}$  eV in order to contribute significantly to the AGN flux density [41, 42]. This contribution reveals that high-energy neutrinos are generated, which may quickly escape the powerful magnetic fields produced by the plasmas around the supermassive black hole.

### 1.3.5.2 Galactic neutrinos sources

There are many galactic objects that, although being weaker than extra-Galactic sources, are potential candidates for neutrino sources. Among these are Galactic Center, supernovae and micro-quasars. In the following paragraphs, we will provide some details about these sources.

**1.3.5.2.1 Galactic Centre** Galactic Centre (GC) sources in the Milky Way Galaxy are being considered for high-energy neutrino detection. The emission of CRs from the GC direction expands the assumptions of neutrino fluxes in the TeV to PeV energy range from pion or neutron decay owing to proton-proton collisions from the same shock-accelerated, GC population with ambient photons [43]. HESS J1745-290, the Galactic supermassive black hole, and the SNR SgrA East revealed by HESS are the most investigated sources

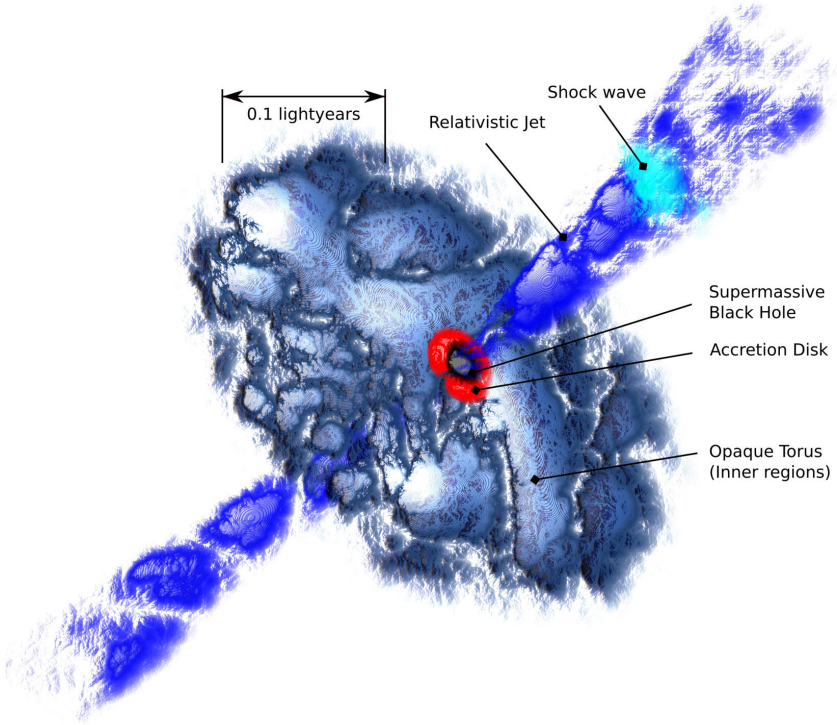


Figure 1.8: Schematic description for an active Galactic Nuclei AGNs.

of TeV  $\gamma$ -rays in the direction of the GC. For energies greater than 1 TeV and 5 TeV, the predicted number of neutrino events from the GC during a five-year period is between 2 and 3 respectively for a  $\text{km}^3$  detector [44]. In simpler terms, because these particles originate from the same source, we can use the fluxes of  $\gamma$ -rays and neutrons to adjust the predicted neutrino flux.

**1.3.5.2.2 Supernovae remnants SNRs** Supernovae are the debris of stars that exploded after they died. These explosions are fairly rare phenomena in our own galaxy, occurring once every century on average. They are very energetic, emitting large amounts of energy in the form of gamma rays and neutrinos. These neutrinos, however, are not energetic enough (typically  $E \sim 10$  MeV) to be detected by neutrino telescopes. Despite this, high-energy neutrinos can be created in the very brief period following the explosion. A supernova can produce a neutron star, a pulsar, a binary system, or even a black hole. Supernova remnants (SNRs) are the remains of exploding stars.

SNRs are consisting of hot gases propelled into space by the power of the supernova explosion. These relics might be thousands of years old and hundreds of light years across. All of these components provide various particle acceleration scenarios. Supernovae produced by massive stars (Type II supernovae) can generate shock waves capable of speeding protons beyond 10 TeV. Some models estimate [45] up to 100 events in a  $\text{km}^2$  detector from a supernova source  $\sim 10$  kpc away, more details on the observations might be found in [46, 47]. SNRs are suggested as CR accelerators [48]. This assumption is based on energy losses of CRs from the Galaxy, which may be compensated for by assuming that each new SNR converts a small proportion of its kinetic energy into CRs [49]. Significant amounts of protons are converted into neutrons by electron absorption and subsequent neutrino emission in such processes. During core-collapse supernovae, all of the gravitational energy released

is expelled as intense neutrino fluxes from the newly formed neutron star. In contrast to photons, which take hours or days to escape from the star envelope, this neutrino signal is released quickly.

**1.3.5.2.3 Micro-quasars** Micro-quasars are X-ray binary systems (XRBs) consisting of a compact core object, for instance a neutron star or a black hole, as part of an accretion system of materials from a nearby star. The physics principles that explain the mass accretion of matter into black holes are believed to be the same as those which explain the mass accretion of matter into other systems such as AGNs and GRBs. When the companion star's mass exceeds ten solar masses, they are categorized as "High-Mass X-ray binaries" (HMXBs), otherwise they are classified as "Low-Mass X-ray binaries" (LMXBs). The mass transfer mechanism may be described using "Roche lobe" overflow and stellar wind dynamics (44). The gravitational energy released by the falling matter into the system creates collimated relativistic jets. In the binary system, these jets are ejected perpendicular to both sides of the accretion disc. The hadronic component of the jets is unknown at the moment [50]. Some models predict the neutrino emission from micro-quasar jets [51, 52].

When considering HMXBs, neutrinos and  $\gamma$ -rays can be produced through the interaction of hadrons in the relativistic jet and aggregates of the stellar wind whose huge micro-quasars are composed of. Some common micro-quasars (HMXBs) have already been observed utilizing high and very-high  $\gamma$ -ray energies, including the LS5039 and LSI+61°303, discovered by HESS and MAGIC and validated by Fermi-LAT, or the CyG X-1 discovered by MAGIC and AGILE, and CyG X-3 discovered by AGILE and Fermi-LAT [50].

## 1.4 Exotic particles

Exotic particles are theoretical particles that some parts of modern physics believe they exist and have quite strange behaviors. This implies that these particles are uncommon and difficult to produce without the use of a particle accelerator. The term *exotic* is frequently used to describe inexperienced states of matter or particles. The graviton, for example, is an elementary particle that has never been seen and hence appears to be totally theoretical at this moment. Dark matter, which has never been directly detected but is supposed to match the standard model of physics, is considered exotic since it varies from normal observable material.

Exotic particles, unlike protons and neutrons, have a different number of constituent particles than predicted. Protons and neutrons, as previously defined, have three quarks. However, physicists discovered a few years ago that there may be variations: tetraquarks, a four-quark state that has long been predicted to be permitted by quantum chromodynamics. In 2021, CERN identified the signal of such a "exotic hadron" [53]. Several types of detectors have been and continue to be utilized to detect various hypothetical dark matter particles. The answer to the universe's missing mass question is critical in theoretical physics, astrophysics, and cosmology. In any case, distinguishing between ordinary and exotic states and particles is a significant distinction in physics, particularly in distinguishing what we currently know and can see from more unusual states and particles that require further investigation.

Among the exotic particles, we will concentrate on the following in the next subsections:

- *Nuclearites*: they are known as Strange Quark Matter (SQM) nuggets. SQM is composed of about similar quantities of up, down, and strange quarks and is enveloped by an electron cloud, constituting a form of atom. SQM might contribute to the universe's cold dark matter.
- *Magnetic monopoles (MMs)*: which were predicted theoretically by Dirac (1931) and are required by theoretical physics' Grand Unification theories.
- *Q-balls*: Supersymmetry theories anticipated Q-balls to be a coherent state of squarks, leptons, and the Higgs field. Q-balls, for example, might be a candidate for cold dark matter, which has been considered as a solution to the problem of missing mass in the cosmos.

### 1.4.1 Nuclearites

Nuclearites are hypothetical particles derived from the strange quark matter (SQM) theory; we consider it necessary to discuss SQM before addressing nuclearites.

#### 1.4.1.1 Strange Quark Matter (SQM)

Nuclear matter is thought to make up the majority of the visible universe. The bulk of the baryons, the protons and neutrons, are easily capable of creating either enormous, ultra-dense clusters of neutron stars or extremely small, ultra-dense atomic nuclei. In the middle mass range (between 263 and  $\sim 3 \times 10^{56}$ ), there is a large *nuclear desert* where no form of nuclear matter has been detected. The total baryonic mass budget, which by itself contributes a very negligible amount to the overall matter density of the universe, cannot even be explained by the visible cosmos, which consists of visible stars and hot inter-cluster gas. The existence of novel states of matter in which stable entities can emerge by combining the two flavors (up and down) of quark matter seen in ordinary matter with the third quark flavor, the strange quark, is consistent with the Standard Model of particle interactions. The two forms of matter do, however, vary considerably in their structural composition. The hadronic bags' composition, which keeps the quarks free inside the bag-like enclosures while prohibiting their escape, makes a distinction.

It is highly improbable to identify stable bags containing more than three up and down quarks, according to experience. For instance, the deuteron has two different quark bags that stand in for the proton and the neutron in its stable form. The quarks in the deuteron would have spontaneously reassembled into this state if a quark bag large enough to house all six of these quarks had a lower energy than the deuteron; matter as we know it would not exist as a result. A. R. Bodmer [54] investigated the possible results of the addition of strange quarks to the quark bag of up and down types in 1971 and came to the conclusion that such long-lived exotic forms of matter might exist within compact stars, where they would be compressed significantly more than ordinary nuclei. Notwithstanding the prospect of stabilization under pressure, S.A. Chin and A.K. Kerman [55], as well as independently L.D. McLerran and J.D. Bjorken [56], put up some general arguments for why strange matter ought to be stable. Their major justification was that there wouldn't be any empty states to take in the down quarks produced by the strange quark's weak decay; this is the same theory that explains why the neutron is stable inside nuclei but decays into a proton in only about 11 minutes outside of them. If the size of the nucleus increases beyond the attractive range of the short-range internuclear forces, the long-range electrostatic repulsion between the protons will eventually split it up. In contrast, the energy is

distributed equally among the various quark flavors in a hadronic bag, which causes the up, down, and strange quarks to exist in almost equal amounts and start causing a (near) cancellation of charge.

The multi-quark hadronic bags could perhaps simply cover the size range between both the nucleus and the neutron star because they aren't bound by the same size limits that apply to a typical nucleus. Therefore, the notion of a strange universe cannot be completely dismissed. The strangeness can manifest on a wide range of scales, from the creation of heavier than typical isotopes of ordinary elements to bigger strange "nuggets," compact stars made up mostly (or entirely) of strange matter, and even entire "dark galaxies.". The investigation of the potential astrophysical effects of the presence of this other sort of matter and its (close) encounter with the regular nuclear matter objects, on this planet as well as elsewhere in the Universe, is the main driving force behind this endeavor.

A new type of matter thought to exist and be more stable than the ground state of matter has been postulated for roughly 38 years. In fact, E. Witten demonstrated in 1984 that SQM, which is composed of the strange quark in addition to the up and down quarks, is both possible and more stable than standard nuclear matter composed just of up and down quarks. In the context of the *MIT bag model*<sup>2</sup>, SQM is a combination of the three quark flavors up, down and strange encapsulated in a structure known as a *bag* [57, 58]. In fact, Farhi and Jaffe [59] carried out an extensive calculation and show that this new type of matter is possible by using uncertainties resulting from strong interaction computations.

It follows that quark matter made up of  $u$  and  $d$  quarks cannot be stable since ordinary nuclei exist. According to Witten [60], adding a third flavor to a system of two flavors of quarks reduces the energy per baryon by around 90% for a straightforward bag of non-interacting, massless quarks. Consequently, strange quark matter is approximately 100 MeV per baryon more strongly bound than non-strange quark matter. SQM in bulk is a bounded system large enough to eliminate surface effects. According to Farhi and Jaffe [59], SQM is a degenerate Fermi gas containing  $u$ ,  $d$ ,  $s$  quarks and electrons (or positrons) at zero temperature and pressure, having chemical equilibrium maintained by weak interactions:

$$\begin{aligned} d &\longleftrightarrow u + e^- + \bar{\nu}_e, \\ s &\longleftrightarrow u + e^- + \bar{\nu}_e, \\ u + s &\longleftrightarrow d + u, \end{aligned} \tag{1.8}$$

Equilibrium chemical potentials are determined by:

$$\mu_d = \mu_s = \mu_u + \mu_e, \tag{1.9}$$

without the addition of neutrinos, which normally exit the system. With QCD coupling  $\alpha_c = 0$ , and assuming that just the strange quark has a mass  $m_s$ , the thermodynamic potentials would be as follows:

---

<sup>2</sup>MIT for Massachusetts Institute of Technology, is the name of the institute of the inventors of the model.

$$\begin{aligned}
\Omega_e &= \frac{\mu_e^2}{12\pi^2}, \\
\Omega_u &= \frac{\mu_u^2}{12\pi^2}, \\
\Omega_d &= \frac{\mu_d^2}{12\pi^2}, \\
\Omega_s &= \frac{1}{4\pi^2} \left( (1 - \lambda^2)^{\frac{1}{2}} (1 - \frac{5}{2}\lambda)^2 + \frac{3}{2}\lambda^4 \ln(\frac{1 + (1 - \lambda^2)^{\frac{1}{2}}}{\lambda}) \right),
\end{aligned} \tag{1.10}$$

where  $\lambda \equiv \frac{m_s}{\mu_s}$ . The charge neutrality of the bulk system requires:

$$\frac{2}{3}n_u - \frac{1}{3}n_d - \frac{1}{3}n_s - n_e = 0 \tag{1.11}$$

#### 1.4.1.2 Nuclearites interaction

A. De Rújula refers to strange balls or any peculiar lumps of strange quark matter interacting with the Earth as "nuclearites" in his article [61]. We adopt this nomination for the rest of this report. The structure of SQM can be described in terms of a bag model [12]. The chemical potential equilibrium of the quark species requires a number of  $s$  quarks slightly lower than the number of  $u$  or  $d$  quarks. Thus, nuclearite core should have a positive electric charge which would be balanced by a number of electrons surrounding the core. The Coulomb nuclear repulsion protect nuclearites with galactic velocities from direct nuclear interaction with the atoms they may encounter in their path. As nuclearite cross a medium, it displaces the atoms from their path and create a high temperature plasma and radiate a visible light as a black-body radiation from an expanding cylindrical shock wave as sketched in Fig. ??.

Nuclearite core radius  $R_N$  is mass dependent, for masses higher than  $1.5 \times 10^{-9} g$  corresponding to  $8.4 \times 10^{14} \text{ GeV}/c^2$ , it is written as

$$R_N = \left( \frac{3M_N}{4\pi\rho_N} \right)^{\frac{1}{3}},$$

where,  $M_N$  is the mass of the nuclearite and  $\rho_N = 3.6 \times 10^{14} \text{ g/cm}^3$  is the estimated strange quark matter density. Assuming the same expression for the radius for lower nuclearite masses, Fig. ?? shown  $R_N$  versus  $M_N$ .

For a massive nuclearite, the energy loss is mainly due to the elastic and quasi-elastic collisions with atoms constituting the traversed medium. The energy loss per unit of length is

$$-\frac{dE}{dx} = \rho\sigma v^2, \tag{1.12}$$

where  $\rho$  is the density of the traversed medium,  $v$  the non-relativistic velocity of the nuclearite and  $\sigma$  the effective cross section of the nuclearite defined as [62]

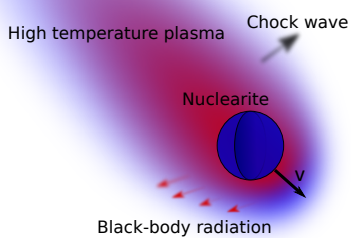


Figure 1.9: Schematic view of the effect of nuclearite crossing a medium. The blue sphere represent a nuclearite traveling at a speed of  $v$  generating a high temperature plasma. In a transparent media, nuclearites induce visible light from an expanding chock wave having a cylindrical shape around the nuclearite core.

$$\sigma[\text{cm}^2] = \begin{cases} \pi \times 10^{-16} & \text{if } M_N < 1.5 \times 10^{-9} \text{ g} \\ \pi \times \left(\frac{3M_N}{4\pi\rho_N}\right)^{2/3} & \text{if } M_N \geq 1.5 \times 10^{-9} \text{ g} \end{cases}, \quad (1.13)$$

where  $M_N$  is the nuclearite mass and  $\rho_N = 3.6 \times 10^{14} \text{ g/cm}^3$  the density of SQM objects. In Eq. ?? the mass limit corresponds to a nuclearite with a radius of about  $10^{-10} \text{ m}$ . As the chemical potential of the s quark in SQM is slightly larger than for u and d quarks, finite SQM objects are always positively charged, thus the effective cross-section for nuclearites with  $M_N < 1.5 \times 10^{-9} \text{ g}$  is controlled by their electronic cloud.

Nuclearites would travel with the typical velocity of gravitationally trapped objects in our Galaxy. Therefore, nuclearites are assumed entering the Earth atmosphere with a velocity of  $\beta_0 = 10^{-3}$ . Before they reach the detector they would propagate through a large amount of material and interact with its constituents. For nuclearites of mass  $M_N$  penetrating a distance of  $L$  in a medium of density profile  $\rho(x)$ , their velocity changes as [62]

$$\beta_L = \beta_0 \times \exp\left(-\frac{\sigma}{M_N} \int_0^L \rho(x) dx\right). \quad (1.14)$$

To simulate the propagation of nuclearites along the Earth atmosphere, the following parametrization of its density can be used

$$\rho(x) = a \times \exp\left(-\frac{x}{b}\right) = a \times \exp\left(-\frac{H - L(x)}{b}\right), \quad (1.15)$$

where  $a = 1.2 \times 10^{-3} \text{ g/cm}^3$ ,  $b = 8.57 \times 10^5 \text{ cm}$ ,  $H = 50 \text{ km}$  is the height of the atmosphere and  $L(x)$  is the penetrating length in the atmosphere. For the propagation in water, a constant density of  $\rho(x) = 1 \text{ g/cm}^3$  is assumed.

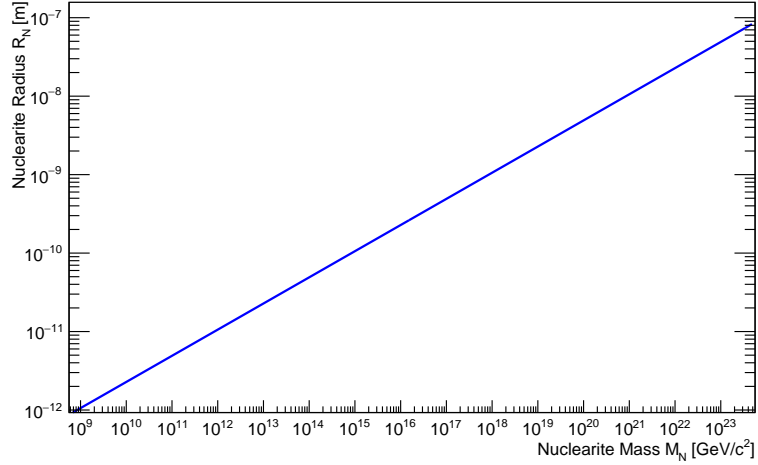


Figure 1.10: Nuclearite core radius as a function of the nuclearite mass. For masses higher than  $8.4 \times 10^{14} \text{ GeV}/c^2$  the core has a radius larger than 1 and all the surrounding electrons are inside the core.

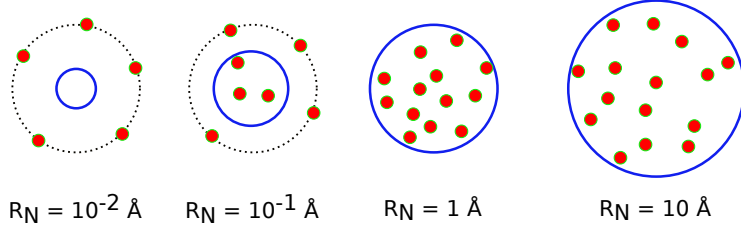


Figure 1.11: A sketch view of nuclearite for different values of the radius  $R_N$ , red point represent electrons and the blue circle the nuclearite core. Starting from 1 and higher, all the electron must be inside the nuclearite core.

Any experimental search for nuclearites has an acceptance of the detector for an isotropic flux of nuclearites that depends on their mass. Only nuclearites with sufficiently large mass ( $> 2.5 \times 10^{22} \text{ GeV}/c^2$ ) can traverse the Earth at typical Galactic velocities [63]. As the flux of nuclearites should decrease when their mass increases. Downward going nuclearites of large masses are expected to cause an overall saturation of a detector that use Cherenkov light as detection technique, producing events with a high number of hits that could not be processed.

A summary of the detection techniques and experimental results can be found in [64, 65] for these particles. Transparent medium (e.g., liquid scintillators or water) have been used in nuclearite searches. Nuclearites as non-relativistic objects do not produce TCherenkov light. They are expected to give rise to a thermal shock through collisions with the atoms of water. The temperature of the medium surrounding the nuclearite path rises up to the order of a few keV. Thus, a hot plasma is formed that moves outward as a shock wave, emitting blackbody radiation and producing many photons in the visible band. A detailed description of the luminous efficiency  $\eta$  defined as the fraction of dissipated energy appearing as light is given in [62]. The authors estimate that in pure water, a fraction of about  $3 \times 10^{-5}$  of the total energy loss is provided in form of visible light. The number of visible photons radiated per unit of path length is estimated as

$$\frac{dN_\gamma}{dx} = \frac{\eta}{\pi} \times \frac{dE/dx}{\text{eV}}. \quad (1.16)$$

### 1.4.2 Magnetic monopoles

Theoretically, a magnetic monopole (MM) in magnetism is the equivalent of the electron in electricity. The prior comparison is still not very persuasive because there has been no experimental proof of MMs as of yet. MMs are assumed to be completely stable, and they must interact strongly with the surrounding magnetic field, which would provide the possibility to search for these particles experimentally.

Paul Dirac has suggested in 1931 the existence of MMs and he has established a relation gathering the electric charge  $e$  and the “basic” magnetic charge  $g$  [9]. If such particle exist it implies the quantization of the electric charge, and this, was the aim of the idea. In analogous way to the Coulomb electric field created by an electric charge, a magnetic monopole of charge  $g$  is assumed to generate a magnetic field  $\vec{B}$  given by:

$$\vec{B} = \frac{g\vec{r}}{r^3}, \quad (1.17)$$

When a charged particle of charge  $e$  interact with a magnetic monopole, the next classical equation of motions is fulfilled:

$$m\vec{r} = e\vec{r} \wedge \vec{B}, \quad (1.18)$$

In order to characterise the quantum mechanism of the charged particle interacting with the magnetic monopole; we need to define the potential vector  $\vec{A}$  such as  $\vec{B} = \vec{\nabla} \wedge \vec{A}$ . We define the action  $S_{int}$ , the interaction term of the charged particle with an external electromagnetic field:

$$S_{int} = \frac{e}{\hbar c} \int_1^2 dt \frac{d\vec{r}}{dt} \cdot \vec{A} = \frac{e}{\hbar c} \int_1^2 d\vec{r} \cdot \vec{A}. \quad (1.19)$$

this action depends only on the path that would be crossed by the particle. Thus we can define the wave function of the particle as follows:

$$\psi(\vec{r}) = \psi_0(\vec{r}) e^{i \frac{e}{\hbar c} \int_0^{\vec{r}} d\vec{r}' \cdot \vec{A}}, \quad (1.20)$$

where  $\psi_0(\vec{r})$  is a wave function that fulfill the free Schrödinger equation. The potential vector  $\vec{A}$  can't be defined continuously on a sphere surrounding the magnetic monopole. Only the relative phase between two paths are interesting in our case.

Let  $\Gamma$  and  $\Gamma'$  be two different paths with the same starting and arriving points. The relative phase would be then:

$$(S_{int})_\Gamma - (S_{int})'_{\Gamma} = \frac{e}{\hbar c} \oint_{S_{\Gamma-\Gamma'}} d^2 \vec{S} \cdot \vec{B}$$

$$= \frac{e}{\hbar c} \Phi_{\Gamma-\Gamma'}$$

By applying the Stokes theorem, the relative path is written as the magnetic flux over a surface limited by the closed path  $\Gamma - \Gamma'$ . Even if is function of well defined magnetic field, the relative action is always multi-valuated. Now, if we consider that the path  $\Gamma'$  is able to sweep once the closed surface that surrounds the monopole and return to its initial position, the action changes as:

$$\Delta S_{int} = \frac{e}{\hbar c} \Phi_{sphere} = \frac{e}{\hbar c} \frac{g}{r^2} \int_0^\pi r^2 \sin \theta d\theta \int_0^{2\pi} d\phi = \frac{4\pi e g}{\hbar c}, \quad (1.21)$$

$\theta$  and  $\phi$  are the zenith and azimuth angles respectively in the spherical coordinate system. The relative phase, is then defined without ambiguity only if  $e^{i\Delta S_{int}} = 1$ , implying:

$$eg = \frac{n\hbar c}{2}, \quad (1.22)$$

$$eg = \frac{n}{2} \quad (1.23)$$

It is crucial to understand whether the energy loss of these particles permits the use of various search techniques and media. The energy loss is  $(g/e)^2 \simeq 4700$  times the energy loss of the minimal ionizing electric charge when MM is accelerated to relativistic velocity. As a result, magnetic monopoles have a significant energy loss, this imply that any type of particle detector may easily search for them.

A monopole with a magnetic charge  $g$  interact in the same way as an equivalent electric charge  $(Ze)^2 = g^2\beta^2$ . The energy loss due to the ionisation processes is described by the Bethe-Bock formula as enhanced by Ahlen. For a particle with an electric charge  $Ze$ , the ionisation energy loss may be written as:

$$\left( \frac{dE}{dx} \right)_e = \frac{4\pi N_e Z^2 e^4}{m_e c^2 \beta^2} \left[ \ln \frac{2m_e c^2 \beta^2 \gamma^2}{I_e} - \beta^2 - \frac{\delta_e}{2} - B_e \right], \quad (1.24)$$

$$\left( \frac{dE}{dx} \right)_m = \frac{4\pi N_e g^2 e^2}{m_e c^2 \beta^2} \left[ \ln \frac{2m_e c^2 \beta^2 \gamma^2}{I_m} - \frac{1}{2} + \frac{K_m}{2} - \frac{\delta_m}{2} - B_m \right], \quad (1.25)$$

where  $K_m = 0.406$  for MM with  $g = g_D$ ,  $\beta = v/c$ ,  $\gamma = \sqrt{1/(1-\beta^2)}$ ,  $N_e$  and  $m_e$  are the electrons density and mass respectively,  $I_{e,m}$  and  $\delta_{e,m}$  refers to the mean ionisation potential and the density effect correction for electric and magnetic projectiles.

Physicists have been on the hunt for a particular particle more than any other, this elusive particle is the magnetic monopole. Although it is known by its more popular term "electric

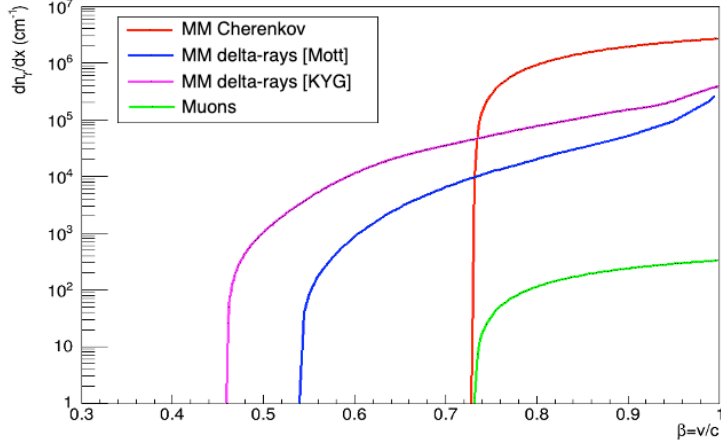


Figure 1.12: Number of TCherenkov photons emitted per cm in the sea water from a MM in red, and from delta-rays for both Mott and KYG cross-section model as a function of the velocity of the monopole. Direct TCherenkov emission from a single muon is also shown with the green line for comparison.

charge”, the notion of an electric monopole is well-known in physics since it occurs in the form of particles with positive or negative charges, such as electrons and protons. Through the interplay of electric fields, which are defined as going from positive to negative, opposite electric charges attract and similar charges repel. Magnetism appears to be similar to electricity in that it has a magnetic field that runs from north to south. When looking for the magnetic equivalent of the electron, being the magnetic monopole, this comparison falls apart, furthermore, no experimental evidence of MMs has ever been established. MMs are so expected to exist from a theoretical standpoint, discovering one will be a huge step forward in high-energy physics.

MMS get their qualities from physics principles at very high energies, which are considerably beyond the capabilities of any particle accelerator experiment. They are completely stable, they do not decay into other particles, and they interact quite strongly with the electromagnetic field, allowing for the possibility to investigate their existence experimentally.

One of the ways used for hunting MMs is by their light emission due to the traversed medium polarization in a similar manner to muons. Particles exceeding the TCherenkov threshold  $\beta_{th} = 1/n$  in a medium of a refraction index  $n$  induce a coherent light in form of a cone known as the TCherenkov radiation. It is possible to write down the amount of photons produced by direct TCherenkov radiation from an MM with a magnetic charge  $g$  in a tiny window of path length,  $dx$ , and in the range  $d\lambda$  of wavelength, for  $\beta_{th}$ , as follows,

$$\frac{d^2n_\gamma}{d\lambda dx} = \frac{2\pi\alpha}{\lambda^2} \frac{ng^2}{e} \left(1 - \frac{1}{n^2\beta^2}\right)$$

$n_\gamma$  represent the number of the photons produced and  $\alpha = 1/137$  is the constant of the fine structure.  $e$  the electric charge and  $\beta$  is the MM velocity. Beside to the direct TCherenkov radiation, MMs can knock off atomic electrons ( $\delta$ -ray electrons) that may have velocities above the TCherenkov threshold, contributing to the total light yield (Fig. ??).

Recently, ANTARES has reported an updated results on the search of magnetic monopoles

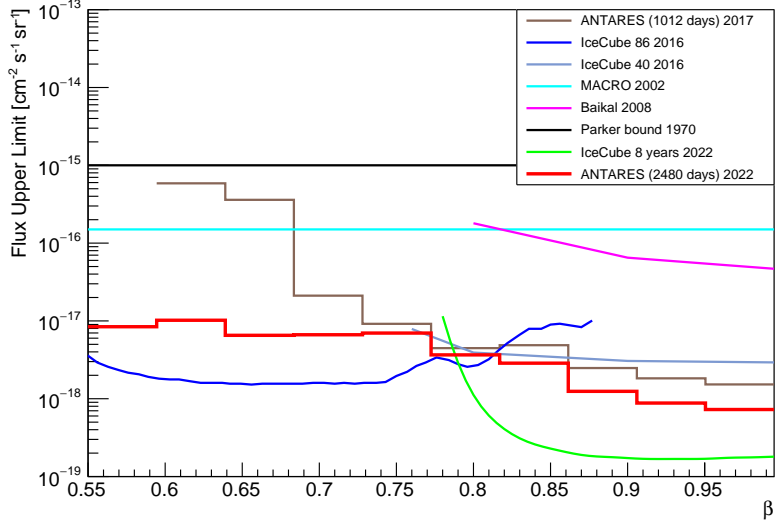


Figure 1.13: The upper limit on the flux of MMs at 90% C.L. as reported by the ANTARES Collaboration (red solid line) for ten years of data taken (corresponding to 2480 days). The results from other experiments are also shown.

using ten years of collected data [9]. In that work, the authors considered the model of Kasama, Yang and Goldhaber (KYG) [66] for the cross-section of MMs, while their previous work [67] was based on the Mott model [68]. The search revels no candidate event was observed and a limit on the flux of these particles is reported at 90% C.L. with comparison with results from other experiments. Fig. ?? shows the reported results along with the others. The results obtained are competitive between ANTARES for relatively low velocities of MMs and for IceCube in the high speed region.

After more than a century of theoretical and experimental work, the existence of magnetic monopoles remains an open question in physics. A magnetic monopole is a hypothetical particle that carries a magnetic charge, analogous to how an electron carries an electric charge. The concept of magnetic monopoles was first introduced in the 19th century by the physicist Pierre Curie, but the search for them has been ongoing for much longer. Several theories predict the existence of magnetic monopoles, including grand unified theories (GUTs) and string theory. In GUTs, the magnetic charge is related to other fundamental forces and particles, while in string theory, magnetic monopoles are considered a natural consequence of the theory's extra dimensions.

Experimental efforts to detect magnetic monopoles have been ongoing for several decades. One of the most famous experiments was conducted by Blas Cabrera in 1982, where he searched for magnetic monopoles using superconducting magnets. Despite many other experiments with different techniques and set-ups, no magnetic monopoles have been detected to date. However, the search for magnetic monopoles continues to be an active area of research, and new experimental techniques and theoretical ideas continue to be proposed. For example, in 2020, a team of researchers proposed a new method for detecting magnetic monopoles using topological insulators.

In conclusion, while the search for magnetic monopoles has yet to yield any definitive evidence of their existence, the theoretical motivation and experimental efforts have continued for over a century. It remains an important and intriguing area of research in physics.

### 1.4.3 Q-balls

Q-balls are soliton-like solutions that naturally occur in certain scalar field theories and in Supersymmetric extensions of the Standard Model (SSM). The notion of Q-balls was raised in 1985 when Sidney Coleman published a paper addressing the possible existence of a new class of non-topological solitons in the frame of a self-interacting system. They are a soliton solutions for a vast class of Abelian gauge field theories. Once they are formed, Q-balls are absolutely stable. These objects are symmetrically spherical and they carry a charge  $Q$  with respect to an internal symmetry. The main interest of this solution is that, for the same charge, it represents a lower energy configuration than ordinary matter. Its existence and stability are consequences of the conservation of a Noether charge and the existence of internal cohesion forces. In its ground state, it is a localized and coherent cluster of field, energetically favorable in front of as many free mesons. It is a bound state that is not obtained by disturbing the vacuum.

Lets consider the simple  $SO(2)$  invariant theory of two real scalar fields given by Lagrangian density [69]:

$$\mathcal{L} = \frac{1}{2}(\partial_\mu\phi_1)^2 + \frac{1}{2}(\partial_\mu\phi_2)^2 - U(\phi) \quad (1.26)$$

where  $\phi = \sqrt{\phi_1^2 + \phi_2^2}$  and the symmetry of the  $SO(2)$  group is given by:

$$\phi_1 \longrightarrow \phi_1 \cos(\alpha) - \phi_2 \sin(\alpha), \quad (1.27)$$

$$\phi_2 \longrightarrow \phi_1 \sin(\alpha) + \phi_2 \cos(\alpha) \quad (1.28)$$

And the associated conserved current and conserved charge are as follows:

$$j_\mu = \phi_1 \partial_\mu \phi_2 - \phi_2 \partial_\mu \phi_1, \quad (1.29)$$

$$Q = \int d^3x j_0. \quad (1.30)$$

Now, lets constraint the solution with the minimum energy conditions:  $U(\phi) = 0$  which represent the absolute minima for the potential;  $\phi = 0$  represent the ground state with unbroken  $U(1)$  symmetry. In this case, a new particle representing the field  $\phi$  with a charge  $Q = \pm 1$ . The existence condition is such that the minimum of  $U/|\phi|^2$  is at some value  $\phi_0 \neq 0$ . This is given by [69]:

$$\text{Min}[2U/\phi^2] \equiv 2U_0/\phi_0^2 < \mu^2 = U''(0) \quad (1.31)$$

Squark condensates would create Q-balls, possibly stable states with high baryon numbers (Q-balls with masses more than about  $10^{15}$  GeV are stable). Candidates for the universe's dark matter include stable Q-balls. The discovery of Q-balls is within the capability of the proposed high-energy gamma-ray, cosmic-ray, and neutrino observatories due to reasonable values of Q-ball charge and the SUSY breaking scale.

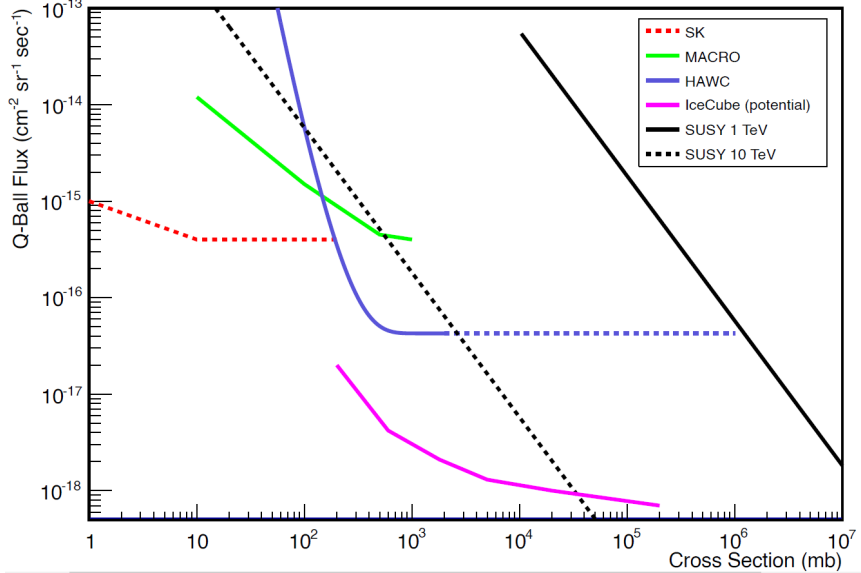


Figure 1.14: Limits that are already in place and those that could be added in the future for neutrino, gamma-ray, and cosmic-ray detectors on the flux of Q-balls as a function of cross section.

$$M_Q = \frac{4\pi\sqrt{(2)}}{3} M_S Q^{3/4} \text{GeV} \quad (1.32)$$

$$\sigma = \pi R_Q^2 = \frac{\pi}{2} \frac{Q^{1/2}}{M_S^2} \approx \frac{10}{M_S^2} \sqrt{Q/10^{14}} \text{ mbarns} \quad (1.33)$$

where  $M_S$  denotes the SUSY breaking scale in TeV and  $Q$  denotes the Q-baryon ball's number (charge). It should be noted that the cross section is completely geometrical and extremely huge. Q-balls will be stable when it is energetically impossible for them to decay into an equivalent amount of protons, which happens when  $Q > 5.010^{14}(M_S/\text{TeV})^4$ . Because of their high mass, the predicted flow of Q-balls at Earth would be modest (assuming they contribute to the universe's dark matter) [69]:

$$F \approx \frac{\rho_{DM} v}{4\pi M_Q} \approx 7.2 \times 10^5 \left( \frac{\text{GeV}}{M_Q} \right) \text{ cm}^{-2} \text{sec}^{-1} \text{sr}^{-1}. \quad (1.34)$$

where the virial velocity,  $v$ , is assumed to be 300 km/s and  $\rho_{DM} = 0.3 \text{ GeV/cm}^3$ . Q-ball fluxes of  $\sim 10^{16}$  or fewer are possible for stable Q-balls and interesting SUSY breaking scale values. Large effective areas, which are currently typical in cosmic-ray, gamma-ray, and neutrino investigations, are necessary for such a low flux.

A Q-ball's interaction with ordinary matter would result in a spectacular signal in the proper detector. When a Q-ball interacts with a proton, the proton is absorbed (raising the Q-ball's baryon number) and an anti-proton is released. As a result, the energy released into the detector at each collision with a nucleus will be around 1 GeV/nucleon, the bulk of which will be in the form of pions.

In cosmology, Q-balls are interesting because they can be produced during the early universe, possibly through a phase transition. Depending on their properties, they may be stable and could potentially make up some or all of the dark matter in the universe. Additionally, Q-balls could be responsible for a number of interesting phenomena, including baryogenesis (the generation of matter-antimatter asymmetry) and the production of ultra-high-energy cosmic rays.

While there is currently no direct evidence for the existence of Q-balls, their properties and potential implications makes them an intriguing subject of study in both particle physics and cosmology.

In conclusion, Q-balls can carry conserved charges, such as baryon number or lepton number, which are associated with fluxes. The charge of a Q-ball can be quantized, taking on certain discrete values. The size and charge of Q-balls are determined by the details of the underlying theory. In particular, it has been shown that Q-balls cannot carry arbitrarily large charges in theories with a continuous symmetry. The stability and energetics of the system also place constraints on the size of Q-balls. For example, Q-balls that are too small may be unstable and decay quickly.

One important result in the study of Q-balls is the Coleman-Mermin-Wagner theorem, which states that continuous symmetries cannot be spontaneously broken in two dimensions. This implies that Q-balls cannot form in two-dimensional theories with continuous symmetries. The Coleman-Mermin-Wagner theorem was first proven in the context of classical statistical mechanics by Mermin and Wagner in 1966 [70], and was later extended to quantum field theory by Coleman in 1973 [71].

Another important result is the Friedberg-Lee-Sirlin theorem, which states that Q-balls cannot carry arbitrarily large charges in theories with a continuous symmetry. The Friedberg-Lee-Sirlin theorem was proven in 1976, and places an upper bound on the charge of Q-balls in certain theories [72].

Finally, it should be noted that Q-balls are a hypothetical construct that have not been observed in experiments. However, they arise naturally in certain models of particle physics and cosmology, and continue to be an active area of research. The limits on Q-balls that have been found in various studies depend on the mass and charge of the Q-ball, as well as the conditions under which it was formed. We report below some of the recent limits on Q-balls:

In 2020, the LHCb collaboration at CERN searched for Q-balls in proton-proton collisions at high energies. They set a lower limit on the mass of stable Q-balls of about  $19 \text{ TeV}/c^2$  for certain models of supersymmetry. In 2019, the ATLAS collaboration at CERN searched for Q-balls in proton-proton collisions at high energies. They set a lower limit on the mass of stable Q-balls of about  $17 \text{ TeV}/c^2$  for certain models of supersymmetry.

In 2018, a study by Kusenko and Shaposhnikov derived constraints on the properties of Q-balls that could form in the early Universe. They found that the charge of a stable Q-ball must be less than about  $10^{12}$  times the charge of the electron.

These limits suggest that Q-balls, if they exist, are likely to be very massive and difficult to produce in current particle accelerators. However, the possibility of their existence continues to be an active area of research in particle physics and cosmology.

## 1.5 Conclusion

In this chapter, we have explored the standard model of particle physics, which describes the fundamental particles and forces that make up the universe. The standard model has been remarkably successful in explaining the behavior of particles at the smallest scales, and it is the foundation upon which much of modern particle physics is built. We have also discussed several astrophysical messengers of the Universe, including cosmic rays, neutrinos, gamma rays, and gamma-ray bursts. These messengers provide crucial information about the nature of the universe and the processes that govern it, and they have led to many important discoveries in astrophysics.

In addition, we have touched upon some exotic particles, including nuclearites of strange quark matter, magnetic monopoles, and Q-balls. These particles are not yet confirmed by experimental evidence, but they are intriguing possibilities that could have significant implications for our understanding of the universe.

Overall, the Standard Model of particle physics and the astrophysical messengers of the Universe provide us with a rich and complex picture of the cosmos. As we continue to explore the universe and push the limits of our understanding, we can expect to discover new particles and phenomena that will challenge our current models and expand our understanding of the Universe.

# Chapter 2

## The ANTARES Neutrino telescope

### 2.1 Introduction

The idea of neutrino detectors goes back to the 1950s, when Clyde Cowan and Frederick Reines first detected neutrinos using the intense flux of these particles from a nuclear reactor [73]. Later, scientists detected solar neutrinos and atmospheric neutrinos [74–76]. Neutrinos are produced when cosmic rays interact with their surroundings, yielding particles with no electrical charge and negligible mass. Scientists have wondered about the source of cosmic rays since they were discovered, and finding cosmic neutrinos could provide clues about the origin of the mysterious rays. Neutrinos are a type of subatomic particle that exhibit low interaction cross-sections with matter, rendering them less likely to participate in everyday physical interactions compared to other particles. As a result of their unique characteristics, they are often described as “social misfits” within the particle world. They are produced in some of the most violent, but unknown events in the universe, they travel to Earth at close to the speed of light and in straight lines, which allows them to reveal information about their origin. Supernovas, active galactic nuclei and black holes are some of the possible sources for these ghostly particles.

Until recently, scientists had only detected neutrinos beyond Earth from the sun or from a supernova in the Large Magellanic Cloud in 1987. No neutrinos from distant cosmic sources had been seen. But in April 2012, IceCube recorded two neutrinos with extremely high energies - almost a billion times that of the ones found in 1987 - that could only have come from a high-energy source outside the solar system. After looking deeper into the data, scientists found a total of 28 high-energy neutrinos with energies greater than 30 teraelectronvolts (TeV), reporting their finding in the journal Science [77].

Due to the extremely weak interaction of neutrinos with other particles, a substantial quantity of matter is required to effectively detect them. When neutrinos smash into protons or neutrons inside an atom, they produce secondary particles that give off a blue light called TCherenkov radiation. You need a large, transparent detector shielded from daylight to see them. Thus, scientists build them deep underwater or embedded in ice. The Deep Underwater Muon And Neutrino Detector (DUMAND) project was a proposed underwater neutrino telescope in the Pacific Ocean near the island of Hawaii. The observatory would have stretched nearly 0.25 cubic miles (1 cubic km) of ocean more than 3 miles (5 km) beneath the surface. Started in 1976 but canceled in 1995, DUMAND paved the way for successor projects.

The latest neutrino telescopes will enable more than just new astrophysics. Scientists are starting to use them to look for dark matter, the unknown substance that makes up roughly 85% of the total matter in the Universe. In addition, being able to detect high-energy neutrinos will enable new particle physics that even the best particle accelerators can't achieve.

## 2.2 Neutrino telescopes

Optical astronomical telescopes use optical lens and mirrors to determine, respectively, the intensity and the spectral density of light arriving from a certain direction at the Earth. The analogue task of a neutrino telescope is the detection of neutrinos determining their direction and energy. While visible photons can be collected and directed with mirrors no analogue mechanism exists for neutrinos. This implies that the phase space (area and direction) of neutrinos cannot be changed. Hence, the strategy is to detect single neutrinos and for each single neutrino to determine its direction and energy from the interaction characteristics and from energy and momenta of secondary particles produced in the neutrino interaction.

Over the last few decades, scientists have developed neutrino telescopes to detect these elusive particles. These telescopes are typically located deep in the ocean or ice, where they can detect the faint signals produced by neutrino interactions.

Here are some of the most significant neutrino telescopes and their key features:

1. **DUMAND (Deep Underwater Muon and Neutrino Detector):** Proposed in the 1970s, DUMAND was the first deep-sea neutrino detector [78]. It used photo-multiplier tubes to detect the faint flashes of light produced by neutrino interactions in water. The idea was to deploy a neutrino telescope at a depth of 4800 meters in sea water used as a detection medium. In 1987, DUMAND-I has deployed a first prototype detection line consisting of seven optical detector held to a boat. This line allowed to measure the cosmic muons flux and, thus, it confirms the feasibility of the technique. Later, nine lines have been deployed holding 24 detectors in a second phase named DUMAND-II. However, In 1995 the United States Department of Energy (DOE) stops funding the project due to a failure in data acquisition after 10 hours of operation caused probably by a short circuit induced from a leakage in the connectors. In despite of its failure, DUMAND shows the possibility to construct a telescope that uses TCherenkov photons to detect particles, and this motivated scientists to pursue research and development in the field of deep underwater detectors.
2. **AMANDA (Antarctic Muon And Neutrino Detector Array):** Located at the South Pole, AMANDA used a series of optical sensors buried in the ice to detect neutrino interactions. It began operation in 1996 and was upgraded in 2000 to become the IceCube neutrino observatory.
3. **BAIKAL (Baikal Neutrino Telescope):** The Baikal telescope is located in Lake Baikal, the world's deepest freshwater lake. It consists of strings of optical sensors suspended in the water, which detect the Cherenkov radiation produced by neutrino interactions [79].
4. **ANTARES (Astronomy with a Neutrino Telescope and Abyss environmental RESearch):** Located in the Mediterranean Sea, ANTARES consists of a

series of optical sensors attached to a string anchored to the sea floor. It began operation in 2006 and was designed to study high-energy neutrinos from astrophysical sources. The detector successfully completed its mission and was entirely dismantled in May 2022.

5. **KM3NeT (Cubic Kilometer Neutrino Telescope):** Currently under construction in the Mediterranean Sea, KM3NeT will consist of several strings of optical sensors anchored to the sea floor. It is expected to be completed in 2023 and will be one of the largest neutrino telescopes in the world.
6. **IceCube:** The largest neutrino telescope in the world, IceCube is located at the South Pole. It consists of over 5,000 optical sensors embedded in a cubic kilometer of ice. It began operation in 2010 and has made several important discoveries, including the first detection of high-energy neutrinos from outside our galaxy.

Each of these telescopes uses different techniques to detect neutrinos, but they all rely on the Cherenkov radiation produced by the particles that are generated when neutrinos interact with matter. This radiation produces faint flashes of light, which can be detected by sensitive instruments.

The development of these telescopes has opened up a new era of neutrino astronomy, allowing scientists to study the most energetic processes in the Universe and to probe the mysteries of dark matter and dark energy. As these telescopes are being improved, we can expect to make even more groundbreaking discoveries in the years to come.

## 2.3 The ANTARES detector description

ANTARES (Astronomy with a Neutrino Telescope and Abyss environmental RESearch) was the first completed deep-sea neutrino telescope, it was an European project gathering more than 150 scientists and engineers from 22 institutes in seven countries. ANTARES was located in the Mediterranean Sea  $42^{\circ}50'$  North and  $6^{\circ}10'$  Este, 40 km far from the south of the coast of Toulon in France. The site has been chosen based on the result of several studies including marine conditions, optical noise, sedimentation and bio-activity. The detector was a set of PMT triplet distributed vertically along a string named detection line which was anchored to sea bed with a dead weight called a Bottom String Socket (BSS) at 2475 meters of depth and kept vertical by a buoy at its top end. The detector is connected with a shore station using an electro-optical cable, transmitting multiple queries to collect data and handle the detector control. Fig ?? shows a schematic view of the ANTARES detector. More technical details of the apparatus may be found in [80].

ANTARES was built using the experience of the previous underwater projects previously discussed: DUMAND in the Pacific Ocean and the BAIKAL experiment in Russia. Antares have had a sky coverage of 3:5 sr, comprising the Galactic Center region. The detector, during its construction was running with different configurations between 2006 and 2008. From may 2008 the telescope had began to operate with its full configuration comprising 12 lines collecting experimental data. The science program of ANTARES addresses the search for high energy sources of neutrinos such as active galactic nuclei (AGN), gamma ray bursts (GRBs), micro-quasars or supernova remnants (SNRs), as well as the search for the signal produced by the annihilation of dark matter particles that might have accumulated in the core of dense objects like the Sun. However, Antares was also capable for searching

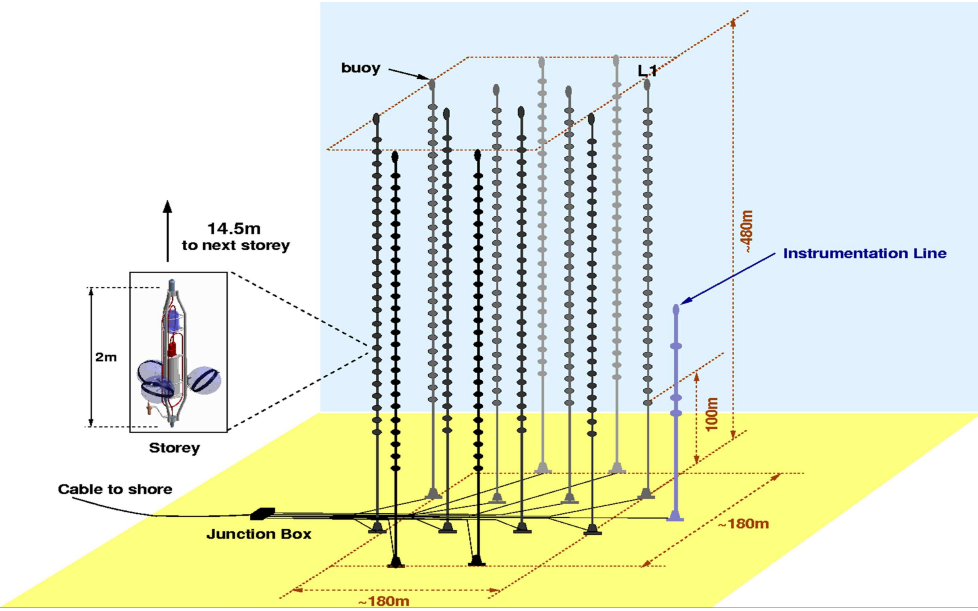


Figure 2.1: Schematic view of the ANTARES detector. The triplet of optical modules constituting a floor is also shown. Each of the 12 detector lines is connected to the Junction Box. The cable to shore transmits power and data to and from the detector.

for exotic form of matter such as magnetic monopoles and nuclearites of strange quark matter.

### 2.3.1 Optical Modules

The main sensor element in Antares is the Optical Modules (OMs), whose task is to collect the physical signals. An OM is consisting of a 10" Hamamatsu photo-multiplier tube (PMT) of 14-stage (Hamamatsu R7081-20) enclosed in a spherical glass with a diameter of about 42.3 cm and thickness of 1.5 cm that resists to high pressure of the external water of nearly 250 bars and the humidity of the deep of the Mediterranean sea. The PMTs are optically coupled with the sphere by using a special gel for which 60 cm absorption length and 1.4 refractive index were measured in the laboratory for wavelengths in the blue domain of the light spectrum. The glass contains also the high voltage power supply and the calibration system. And is transmissible to 95% in the blue band (principal region of TCherenkov light). The hemisphere in the back of the PMT is painted black to absorb parasite induced photons and to minimize the risk of intern reflections. The bulb of the PMT is surrounded by a  $\mu$ -metal cage to reduce the influence of the Earth's magnetic fields.

The PMTs are covering a field of view of about  $70^\circ$  around the PMT optical axis and they have an effective area of about  $440 \text{ cm}^2$ . The quantum efficiency of each PMT depends on the wavelength, optimized to the TCherenkov spectrum and the transmission properties of sea water, which peak in the blue part of the visible spectrum. The OMs are linked to the electronics container through a penetrator.

When a photons hit the PMT cathode it induce the so-called primary photon, that is amplified using the 14 stages dynods and produces an analogue signal at the back-end electronics and then read out by the two analogue ring sampler (ARS) working in *token ring* mode to reduce the dead time. The output signal is provided with a time stamp

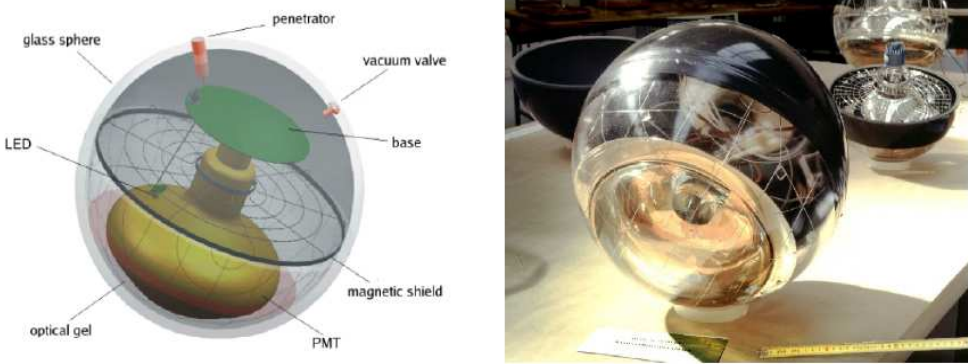


Figure 2.2: Schematic view of an Optical Module showing its different components (left). Picture from an OM at the integration site (right).

and transmitted for further processing. An analogue Pulse Shape Discriminator (PSD) performs the selection between two ARS modes: the *single photo-electron mode* (SPE) using signal integration and the *waveform* (WF) mode within small time by sampling signal. The selection is based on the amplitude of the signal, the time above threshold and the occurrence of multiple peaks within a time gate. Only the charge and time information is recorded for SPE events, while a full waveform analysis is performed for all other events.

### 2.3.2 Storeys

Storeys are the main constituent of an ANTARES line. A storey is a group of three OMs attached to a mechanical structure consisting of titanium frame called *optical module frame* (OMF). At the middle of the OMF is the so-called local control module (LCM) which contains the local readout and slow control electronics housed in a hollow cylinder. All the electronics commands, the clock signal, the slow control, the HV supply and the readout, arrive at the OMs via the electronics boards housed in the LCM. In order to maximizing the detection of Cherenkov radiation from up-going muons and reduces the very high background of atmospheric muons, the OMs are tilted 45° downward and pointing 120° away from each other to ensure the overlapping of the field of view of the individual OMs which would lead to correlations between any two or all three OMs. An other reason to point OMs downward is to avoid deposit of dust on the PMTs photosensitive surface. In such chosen conditions, the average transmission loss after one year was measured around 2%. Some of the storeys contain additional instruments such as a pressure-resistant glass cylinder, a positioning hydrophones used for acoustic positioning, compasses and tilt-meters, and the LED optical beacon for the in-situ time calibration used for calibration purposes (more details in section ??).

### 2.3.3 Lines

Twelve independent lines (or strings) corresponding to 885 photo-multiplier tube consist the ANTARES optical part. Each line is equipped with 25 storeys spaced by 14.5 meters, while the first storey is placed at 100 meters above the sea bed. The lines are anchored to the soil via a Bottom String Socket (BSS) that contains also a String Control Module (SCM) and the String Power Module (SPM) to provide data and power connection to the line. A distance that varies from 60 to 75 meters separate one line from an another one. a group of five storeys form a *sector*. Fig. ?? shows the detector shape, each dot refers to a

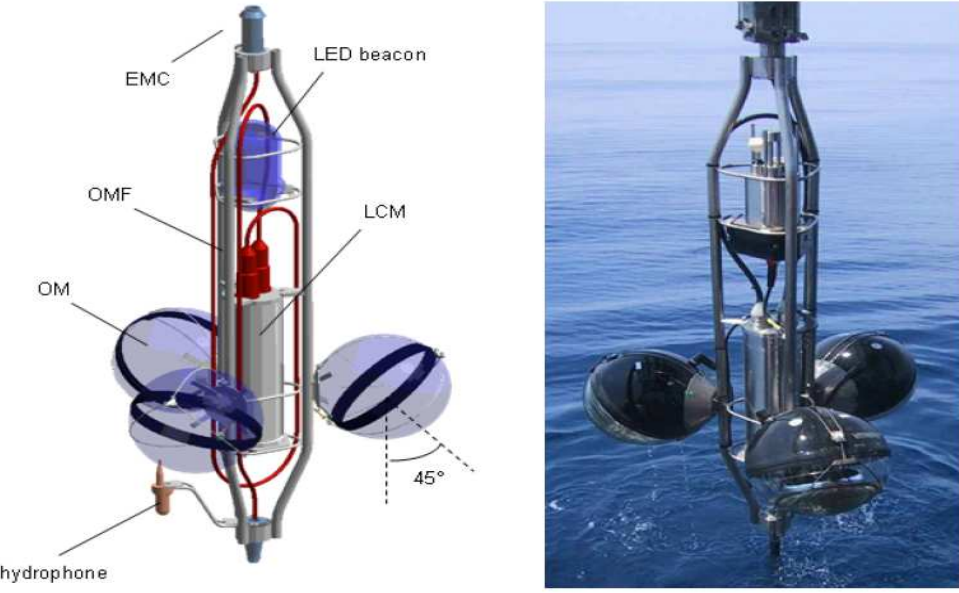


Figure 2.3: On the left, a scheme of a storey is presented: the structure holds three OMs, the electronics LCM and (in some cases) the Optical Beacons used for time calibration or the hydrophones for detector positioning. On the right a picture of a real storey during its deployment.

line.

All the signals recorded by lines are sent to the *junction box* (JB). The JB is a one meter high pressure container providing communication between the lines and the shore station, and housing the power transformer and acts as a line over-current protection. The main electro-optical cable (MEOC) is a 40 Km cable successfully deployed at “Les Sablettes” beach of Toulon in October 2001 connecting physically the JB to the shore

#### 2.3.3.1 Instrumentation line

Beside the twelve detection lines, Antares have an additional line called Instrumentation line (IL). It is equipped with different sensors to collect constantly environmental parameters supporting the efficient operation of the optical detector such as water transparency and the sea current profile, and also to perform interdisciplinary studies, such as a seismic monitoring of the sea floor or measurement of the oxygen levels in the sea water.

## 2.4 The ANTARES data acquisition system

The main tasks of the data acquisition (DAQ) system [81] are to digitize the signals coming from the PMTs, ensure the transport of the data to the shore station, perform the triggering and store the filtered data on the storage support. The DAQ system also prepare the detector for data taken and provide an interface for run settings.

The majority of collected signal (up to 92%) are due to a photo-electron (pe) charge resulting from a single photon that extracted an electron at the PMT photo-cathode level. These signals have the same characteristics, in such a way that the signal form become useless. Thus, only the time and charge are saved for usage in physical analyses, the time

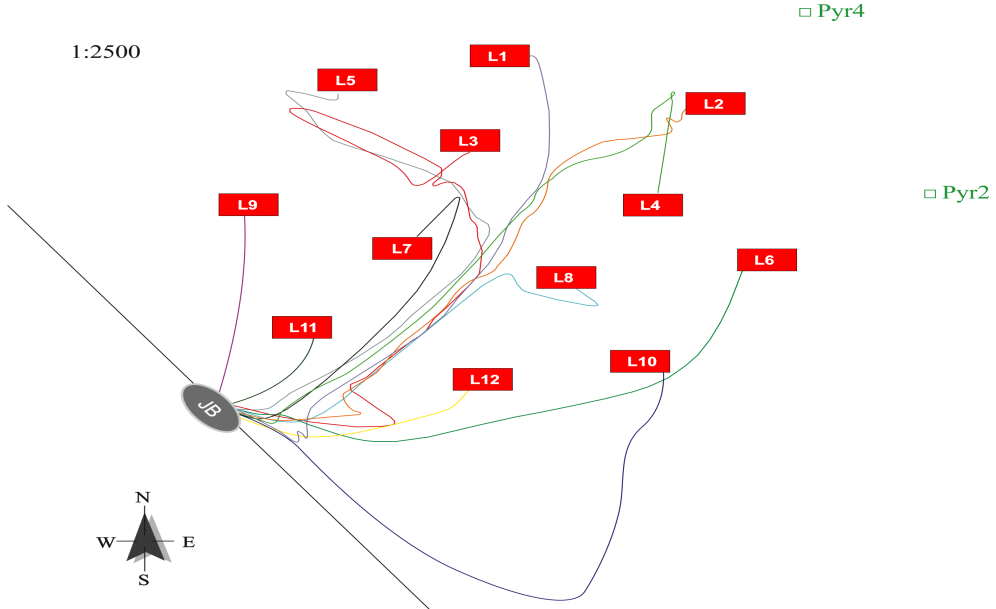


Figure 2.4: Distribution of the Antares lines in the sea bed. The bleu dots are referring to a line, the outer lines form an octagonal shape. The JB gather the lines signals and send them to shore farms.

is given by the internal clock of the LCM when the signal exceed the so-called L0 threshold set to 0.3 pe and the amplitude is the integration of the anode charge over 33 ns (8 ns before and 25 ns after the passage of threshold).

At the detector level, all signals with an amplitude exceeding the L0 threshold set to 0.3 photo electrons (p.e.) are digitized at the LCMs and then sent to the shore PC farm following the concept of *all-data-to-shore*

## 2.5 Detector calibration

In order to carry out physical analyses, it is relevant to calibrate the detector to get an accurate values for measured parameters. In ANTARES, time and charge calibration are performed using dedicated systems, the positioning calibration are also required due to the change in direction and speed of sea current.

### 2.5.1 Time calibration

The absolute time calibration is required to relate events with astrophysical phenomena, while an accurate relative timing is required to achieve the best angular resolution of the detector. A set of an-shore calibrations are made before the deployment of the OMs, while the in-situ calibrations are made after the OMs being deployed in the deep sea. This calibration is made by different system described bellow.

The time offsets between different OMs affect the relative time resolution of the PMTs. This has a major effect on the track reconstruction that exploit the arrival time information of the Tcherenkov photons on the PMTs. Uncertainties on the OMs relative time comes from the Transit Time Spread (TTS) in the OM, which is equal to 1.3ns. The chromatic and the light dispersion resulting of time smearing of about 1.3ns for 40m and the residual

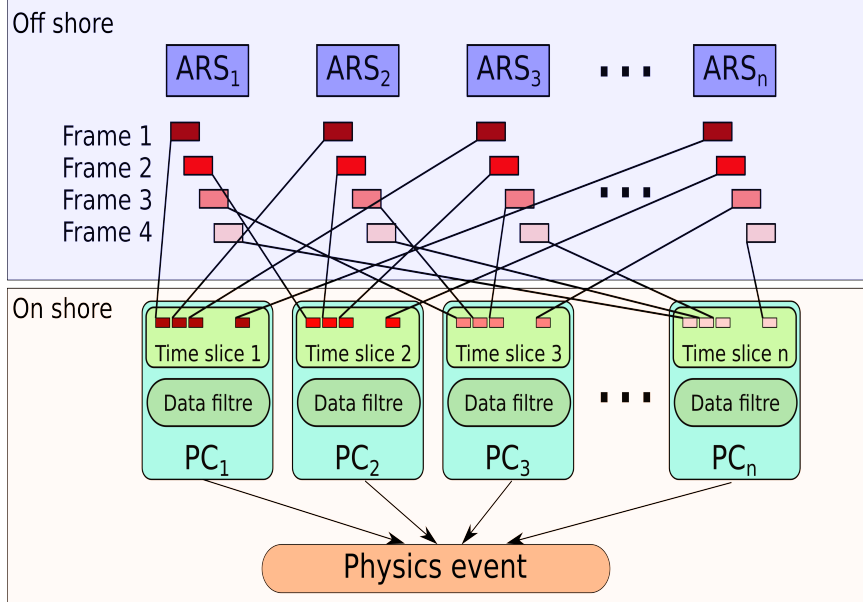


Figure 2.5: On-shore calibration in the dark room - A common laser signal is distributed to the whole sector where the time offsets for each detection unit is computed.

time offset which is estimated to be no bigger than 0.3 ns are both a source of uncertainties on the relative time.

The absolute time resolution relays on the time offset between the master clock and the UTC time provided by the GPS. It is equal to 100ns. The absolute time is used to study the correlation of the transit source such as *active galactic nuclei* flares and *gamma ray bursts*. This time is also used to transform the local referential frame to Equatorial and Galactic coordinates systems.

### 2.5.1.1 On-shore calibration

At the dark room, and by using a laser and a clock system, a couple of on-shore tests are performed before lines immersion aiming to determine the relative time offsets between the detection units. The entire sector (groups of 15 OMs) is flashed using optical fibers simultaneously by very short laser pulses with 1 kHz of green light ( $\lambda = 532$  nm) in the dark room, the PMT of the first storey is taken as a reference. Each optical fiber is coupled to a Lambertian diffuser which spreads out the laser light over the full PMT photo-cathode area.

### 2.5.1.2 In situ calibration

After being deployed, all devices are aimed to operate in a good condition; this task is ensured by the in situ calibration. The in situ time calibration uses multiple techniques we describe in the next paragraph.

An internal LED is placed inside the OMs (it can be seen in Fig ??). The LED sends light pulses with a wavelength of  $\lambda = 472$  nm allowing to measure the transit time of the corresponding PMT. The uncertainty on the transit time is less than 0.5 ns according to the results of the calibration. A second in situ time calibration is ensured by the so-called LED Optical Beacon (LOB) constituting of 36 LEDs emitting light in  $\lambda = 472$  nm with a

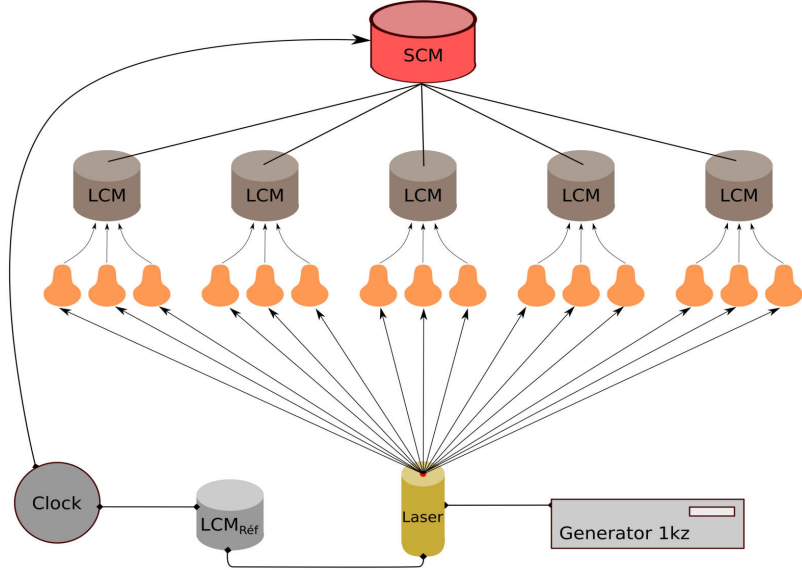
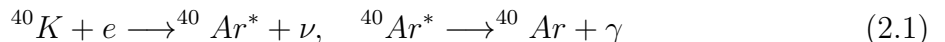


Figure 2.6: On-shore calibration in the dark room - A common laser signal is distributed to the whole sector where the time offsets for each detection unit is computed.

maximum power of 160 pJ. For each line, four LOBs are fixed in the storey 2, 9, 15 and 21. This system allows for the time offset measurement between the OMs of the same storey. Antares uses another system to calibrate the lower storeys, The Laser Beacon (LB), It uses two lasers placed in the BSS of line 7 and line 8 that emit a light pulse with a power of 1  $\mu$ J and a wavelength of  $\lambda = 532$  nm. The LB is used to calibrate the interline time by the mean of measuring the time offset between the lines.

The decay of potassium 40 ( $^{40}K$ ) is also used for the in situ time calibration. Actually, the radioactive  $^{40}K$  isotope produces visible photons in two ways. The first mode is by decaying into calcium plus an electron and a anti-neutrino. The electron may be energetic in such a way to overcome the Tcherenkov threshold, giving rise to an optical background in the detector. The other way that  $^{40}K$  would produce light is by the mean of compton scattering of photons with an energy of 1.46 MeV given birth to two consecutive reactions:



By studying the arrival time of the photons derived from a  $^{40}K$  decay on two OMs of the same storey, an in situ calibration is made. Fig. ?? illustrate the time difference  $\Delta t$  in nanoseconds between the hits of two OMs, the plot constitutes of a base line around 1100 due to the time difference between random hits and a peak of Gaussian form due to the photons coming from the same  $^{40}K$  decay process.

### 2.5.2 Charge calibration

The amplitude of the signal generated by a muon is a critical parameter for accurately reconstructing the muon's energy and performing meaningful physics analyses. To convert the signal amplitude into a quantity of photo-electrons (p.e.), the ANTARES detector relies on calibrated values of charge. In order to maintain the accuracy of the charge calibration,

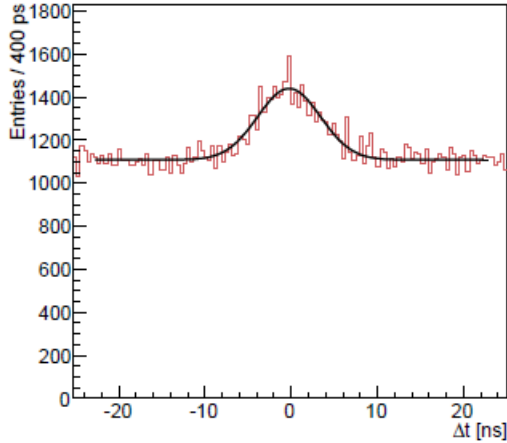


Figure 2.7: Difference of the time between the OMs of the same storey. The base line is due to the difference between the random hits while the Gaussian around zero are due to the hits coming from the photons generated from the same decay process.

regular checks are performed to correct for any changes in the gain of the photomultiplier tubes (PMTs) that can impact the observed signal amplitude. This approach ensures that an effective threshold of 0.3 p.e. is maintained across all the channels of the detector [80]. By maintaining a consistent threshold level and calibrating the signal amplitudes, the ANTARES detector can accurately detect and measure high-energy muons and other subatomic particles, enabling important advancements in the field of astrophysics and particle physics.

### 2.5.3 Position calibration

As previously mentioned, the ANTARES detector lines consists of flexible strings that suspend multiple storeys equipped with optical modules (OMs). Due to the strong and varying sea currents in the detector site, the position of the OMs can be altered by several meters from their nominal position. Precise knowledge of the relative position of each OM is crucial to accurately reconstruct particle tracks. In order to achieve this, ANTARES employs two independent systems for position calibration: an acoustic system and a combination of compasses and bi-axial tilt meter sensors. These systems allow for the precise determination of the three-dimensional position and orientation of each OM, thereby enabling accurate track reconstruction with high precision. The use of multiple calibration systems ensures redundancy and enhances the overall accuracy and reliability of the detector's position calibration, which is crucial for achieving high sensitivity in the detection of high-energy particles.

The acoustic system includes one transceiver/receiver ( $T_x/R_x$ ), an acoustic signal of 40-60 kHz is sent from an emitter and received by hydrophones fixed on each sector (set of five storeys). By measuring the traveling time of this signal, the position of each hydrophone is obtained using the triangulation and least-square minimisation techniques. The tilt angles with respect to the horizontal plane (pitch and roll) and the orientation of storeys are with respect to the Earth Magnetic North are obtained using a tilt-meter and a compass sensor respectively. These informations allows to reconstruct every two minute based on a model which predicts the mechanical behavior of the line facing the influence of the sea current.

Finally the position of each OM is deduced using the reconstructed line information and the known geometry of the storeys.

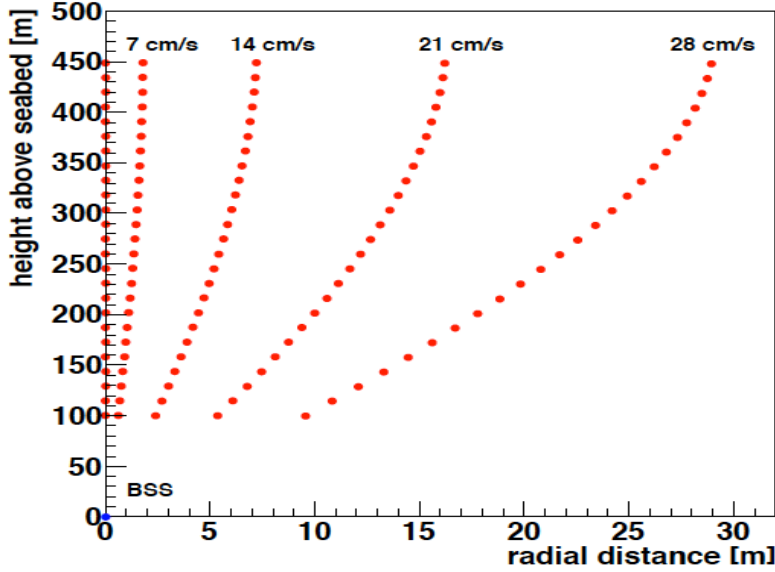


Figure 2.8: Calculated positions (height and radial displacement) of the storeys of a line (red circles) with respect to its anchor for different sea current velocities.

#### 2.5.4 ANTARES filters

In order to filter its data, Antares uses several trigger algorithms . Actually, beside the physical signal, the detector is susceptible to record a high rate of background events (roughly 70 kHz per PMT depending on the L0 threshold) due to the bioluminescence and  $^{40}\text{K}$  decays. On the basis of the space and time correlation, The triggering system allows the rejection of background signals and provide events with high accuracy with a physical signal. A program called *DataFilter* working as a standard hardware trigger system running on shore and process all the raw data after being sent to the PC farm.

The triggering system is relying on three types of hit clusters:

- **L0 hits** are defined as the hits passing the so-called L0 threshold set to 0.3 p.e.
- **L1 hits**, they are defined based on two constraints:
  - An L0 hit could be an L1 hit if its amplitude passes the predefined *high-threshold* set either to 3 p.e. or 10 p.e. depending on the data taken period.
  - A coincidence of at least two L0 hits recorded by two different OMs in the same storey in a time window of 20 ns
- **T3 cluster** is a cluster of L1 hits. At its turn, this cluster is filled based on one of two conditions:
  - A coincidence of two L1 hits within 80 ns in two adjacent storeys.
  - A coincidence of two L1 hits within 80 ns in two next to adjacent storeys.

Based on previous hits and cluster definitions; Antares used six triggering algorithms in an effort to filter the data:

- The 3N or 3D trigger: Requires at least five L1 hits in a time window that correspond to the passage of a muons.
- T3 (2T3) trigger: A manifestation of at least one (two) T3 hit(s).
- the GC trigger: the GC or Galactic Center trigger looks for one L1 hit and four L0 hits in the direction of the Galactic center.
- K40 trigger: Based on the in situ calibration, this trigger requires two L0 hits on two different OMs of the same storey in a time window of 50 ns. This trigger is down-scaled by a factor of about 1000.
- TST: Or the Transit Source Time trigger; it is triggered when an alert is sent by the related  $\gamma$ -ray satellites such as SWIFT and FERMI. When this trigger is launched, two minutes of data is stored without any filtration.

### 2.5.5 Optical background

Optical background in the ANTARES detector refers to the signals that are produced by ambient light, bioluminescence, and other sources of noise in the optical modules that can mimic the signal from Cherenkov radiation produced by a passing muon or neutrino. To reduce the optical background in the detector, the ANTARES collaboration has implemented several techniques, including:

- The usage of a high-pass filter in the signal processing chain to remove low-frequency noise and reduce the contribution of bioluminescence.
- The usage of a coincidence requirement in the Level-1 trigger, which requires a certain number of adjacent optical modules to have signals that exceed a certain threshold. This helps to reject random noise signals that can mimic the signal from Cherenkov radiation.
- The usage of a dedicated optical beacon system, which allows the precise calibration of the optical modules and helps to monitor their stability over time.
- The usage of a veto system, which consists of additional optical modules located outside the main detector volume and facing upwards. These veto modules can detect upward-going muons, which are produced by cosmic-ray interactions in the atmosphere, and can be used to reject downward-going muons that can mimic the signal from neutrino interactions in the detector.

Actually, Beside the light that would be generated by the passage of muons in the telescope, the PMTs are faced to light coming from other sources, in particular those related to the detection environment. A high rate of photons comes from the potassium 40 ( $^{40}\text{K}$ ) decay yielding light by the mean of the  $\beta$  decay and by the bio-luminescence organisms.

When a  $^{40}\text{K}$  decays, it would emit TCherenkov photons visible to the PMTs. Indeed, The sea water contains around 400 ppm of potassium, including a fraction of  $\sim 0.0117\%$  of the radioactive isotope  $^{40}\text{K}$ , which principally decay to  $\text{Ca}^{40}(89.3\%)$  by emitting an electron with a maximum energy of 1.311 MeV. This energy is above the threshold required to initiate a Cherenkov radiation corresponding to about 1.13 MeV for an electron. The equation of the decay is shown in the Eq. ??



The rate of the background detected by the PMTs and resulting from the  ${}^{40}\text{K}$  decay is of the order of  $30 \pm 7$  kHz.

Bioluminescent organisms constitutes an other source of background at the ANTARES site. Bacteria, shrimp, or even some fish emit light for different reasons. The rate of bioluminescence fluctuate in time due to the organisms activities and other sea parameters like sea current and water temperature, the rate is around 30 kHz on the PMTs. Fig. ?? shows the background rate (or baseline rate) measured for several days by different storeys, the baseline rate slightly fluctuate around 60 kHz for the whole period. While, Fig. ?? shows the baseline for a hundred of seconds for three reference OMs, in this figure, the peaks are mainly due to the passage of bio-luminescent organisms near of the nearby PMs. The low fluctuation of about 2-3 kHz seen in ?? are resulting on the electronic background of the PMTs.

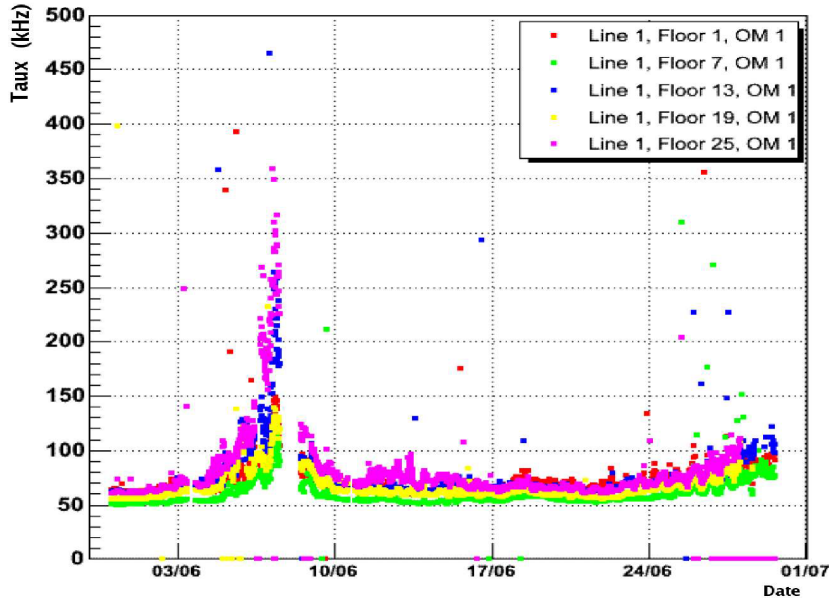


Figure 2.9: Baseline rate for a period of almost one month for OM1 of five storeys of line 1 of ANTARES.

### 2.5.6 Atmospheric background

The majority of the light reaching the OMs ( $\sim 60$  kHz) is derived from the optical background discussed in the previous subsection. Only a small fraction, about 10 Hz, is due to muons. Most of these muons are produced in the decay of charged and neutral mesons originating from the interaction of cosmic rays in the atmosphere, yielding to hadronic showers, hence, we speak about atmospheric muons.

From all the particles that would be produced in the atmosphere by the mean of all processes, only muons and neutrinos have the ability to reach the ANTARES site and radiate a characteristic signal. Fig. ?? shows that the vertical flux of atmospheric muons decreases exponentially with the crossed depth in sea water, this is due to the energy loss as

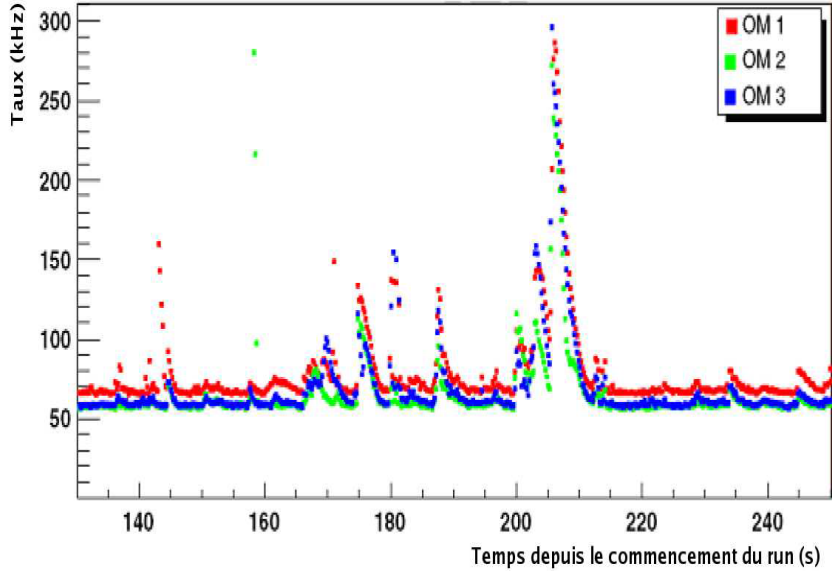


Figure 2.10: Baseline rate for a period of a hundred of seconds for the three OM of one storey.

a Bremsstrahlung,  $e^+e^-$  pair production and photo-nuclear interactions. The contribution of all these processes is shown in figure ??.

As stated before, The ANTARES OMs are declined  $45^\circ$  downward relative to the corresponding line axis. The aim is to favor the up-going particles. The interaction of cosmic rays with the atmosphere produces atmospheric neutrinos; the production is dominated by the decay of pions and kaons up to energies reaching  $10^5$  GeV, beyond this energy, the dominant production process is governed by the charmed mesons decay. These neutrinos could easily pass over the Earth, and they are troublesome for the search of punctual sources of neutrinos. We present in Fig. ?? the differential flux for atmospheric muons derived from the interaction of atmospheric neutrinos at a depth of 2400 m as a function of cosines of the zenithal angle of the incident particle. In that figure, a positive cosine refers to an up-going particle while the negative cosines indicate a down-going particle. As it can be seen, there is a deference of six orders of magnitude between the flux of down-going atmospheric muons and those coming from the decay of atmospheric muons.

## 2.6 Conclusion

In conclusion, this chapter has provided a detailed overview of the ANTARES neutrino telescope, its design, and its operation. While the detector was dismantled in May 2022, it has made significant contributions to the fields of astrophysics and particle physics during its operational lifetime. The unique features and configurations of the telescope's components allowed for the detection of high-energy neutrinos from cosmic sources, providing valuable insights into the most powerful phenomena in the Universe.

The data acquisition system, described in detail in this chapter, was crucial in collecting and analyzing the data collected by the detector. The calibration process used to ensure the accuracy of the data was critical to the success of the research carried out using the ANTARES neutrino telescope.

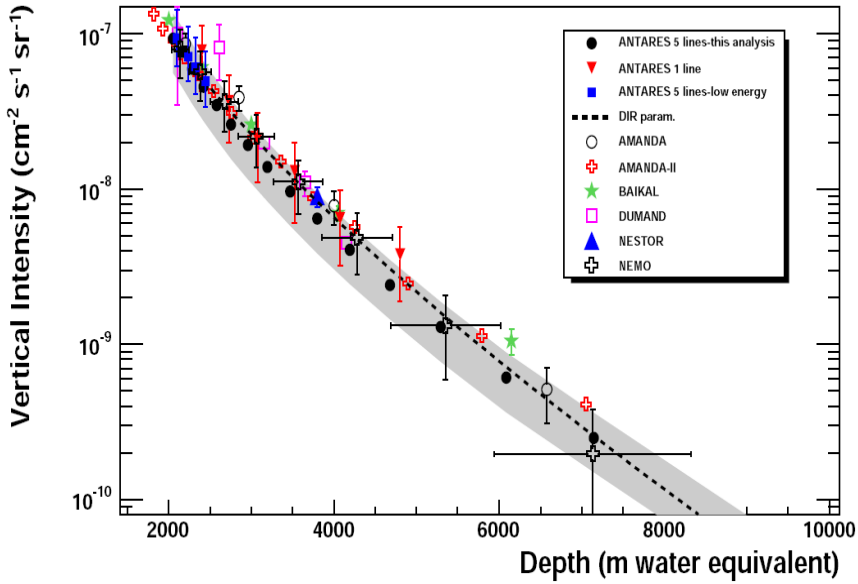


Figure 2.11: Vertical flux of muons resulting from experimental measurements in different ANTARES configuration, as a function of the penetrated depth in water. The expected flux from the parametrisation of Bugaev (dashed line). Other results from underwater detectors are shown : AMANDA, AMANDA-II, Baikal, DUMAND, NESTOR, MEMO.

The dismantling of the ANTARES neutrino telescope does not diminish the importance of the research conducted using the instrument. The contributions made by the detector have advanced our understanding of the universe and the processes that occur within it. The legacy of the ANTARES neutrino telescope will continue to influence the field of astrophysics and particle physics for many years to come.

In summary, the dismantling of the ANTARES neutrino telescope marks the end of an era, but the valuable insights gained from its research will undoubtedly continue to impact the field of astrophysics for years to come. The contributions made by the detector serve as a testament to the ingenuity of the scientific community and highlight the importance of investing in scientific research and development.

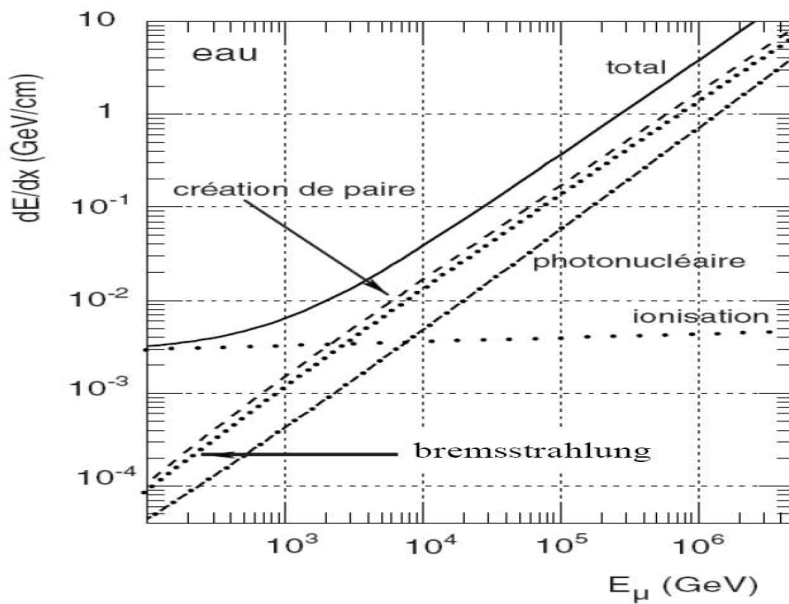


Figure 2.12: Theoretical energy loss per unit of length as function of the energy of a muon propagating in water.

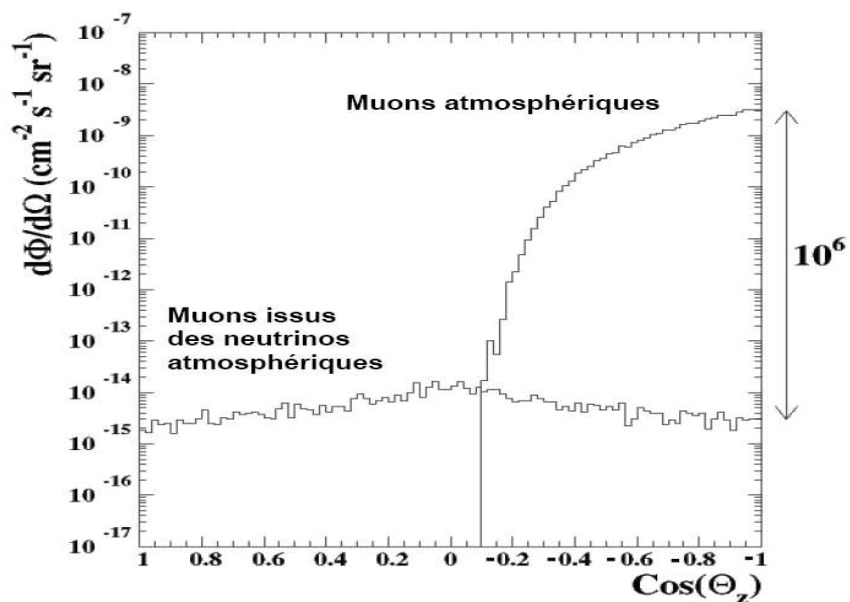


Figure 2.13: Differential flux for atmospheric muons and muons induced by the interaction of the atmospheric neutrinos at a depth of 2400m as a function of the cosines of the zenithal angles of the incident particle.

# Chapter 3

## Search for nuclearites with nine years of ANTARES data

As described in Chapter ??, the ANTARES detector is a deep underwater detector designed for neutrinos detection. However, other physical analyses are possible to be carried out with the ANTARES data. Among several, multi-messenger, dark matter and exotics analyses are examples of analyses that are already performed in ANTARES.

In this chapter, A description of the nuclearites analysis with the ANTARES neutrinos telescope is detailed. As far as the nuclearites signal into the detector is not well known, a Monte Carlo simulation of these particle is needed in order to simulate their behavior and to characterize the signal that would be expected in the detector. De Rugula and Glashow pointed out a way to detect these particles by the main of their light dissipation in transparent media, in particular sea water. In their work they addressed the possible detection of nuclearites through black body radiation as they traverse a transparent media like water. The focus of this chapter lies in the application of this approach to search for these particles within ANTARES, with a particular emphasis on the techniques employed and the results acquired.

### 3.1 Analysis strategy

An organised strategy has been used to identify the nuclearites signature in Antares. The blinding policy of the collaboration is taken into account by this strategy. The five steps that constitute the analysis are as follows:

- The important first step is to determine the set of runs with a low factor of the parameters characterizing optical activities from the analysis period since the analysis is exposed to the optical background.
- Simulate the detector's response to the passage of the nuclearites of various masses. The collaboration has already used the mupage code to simulate the atmospheric muons which serve as the primary background for cosmic nuclearites.
- Validate the distribution's agreement between a sample of real data and Monte Carlo simulations, and define the parameters which will be used to separate nuclearite events from atmospheric muons events.

- Calculate the sensitivity for nuclearites in ANTARES after optimizing the model rejection factor to get the optimal cuts on the discrimination variables.
- Perform the unblinding request for all data recorded between 2009 and 2017, and if no candidate events are discovered, the final limits on the flux are computed for each nuclearite mass.

## 3.2 Monte Carlo simulation of nuclearites

Before simulating the behavior of targeted particles within a detector, it is essential to conduct investigations to confirm that such particles can penetrate the detector at the required depth and produce a significant amount of light to activate the device and leave a clear trace. The initial step in this study involves determining the threshold mass, which refers to the minimum mass of nuclearites possessing sufficient energy to produce a signal at the end of the PMT electronics.

The propagation of nuclearites through the Earth's atmosphere and sea water as well as the simulation of the predicted signal at the detector level were all included in the Monte Carlo program that was developed to simulate nuclearites in ANTARES. The program is written in Fortran77 and reads from a file containing nuclearites' parameters (mass, initial velocity at the entrance in the atmosphere) and a standard ANTARES geometry structure to determine the positions of each of the detector's 12 strings and individual floor. It provides an ASCII output file with the charge, time, and position of the collected signals. With a detector crossing time up to three orders of magnitude longer than that of relativistic muons or MMs, nuclearites would provide clearly detectable signals. The simulation program was tested, enhanced, and employed to generate the simulated events in the ANTARES detector.

### 3.2.1 Nuclearite mass threshold in ANTARES

Nuclearites are assumed to fall on Earth with Galactic velocities. This is a pure assumption as object surviving from astrophysics processes are free to move in the space and they are more likely forced to move at the same velocity as the Galaxy. The first step of this analysis is to characterize nuclearites at the ANTARES level. This means to determine the arrival velocities of these particles under the previous assumptions. However, the particle would arrive into the detector from different incident angles. Obviously, the path crossed until the detector is incident angle dependent and the particle would lose a significant amount of its energy before it reaches the apparatus. In our case, we are looking for the so-called down-going nuclearites, this means nuclearites arriving to the detector from the top. In the case in which a nuclearite arrives vertically to the detector, its path would have the shortest distance to the detector in both Earth's atmosphere and sea water as shown in figure ???. This corresponds to a null incidence angle.

For a nuclearites arriving vertically from the top to the detector, We computed the number of visible photons radiated per centimeter by a nuclearite as a function of its mass at different levels of the detector, top, middle and lower part (see Fig. ??). As it can be seen, for masses  $< 5 \times 10^{12} \text{ GeV}/c^2$  the number of visible photons that would be generated is less than 1 photon per centimeter for the top part of the detector while for masses  $\sim 10^{13} \text{ GeV}/c^2$  is slightly lower than  $10^3$  photons/cm. In order to choose the mass threshold for detecting nuclearites at the ANTARES depth, we adopt masses generating more than  $10^3$

photons/cm, and based on the simulation of nuclearites in ANTARES described in the next section, the best value of mass to get non ambiguous signal of nuclearites is  $4 \times 10^{13}$  GeV/c<sup>2</sup>.

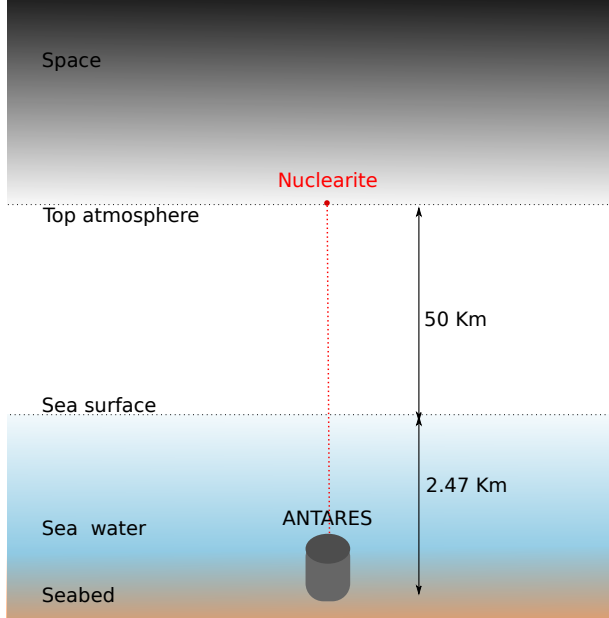


Figure 3.1: Schematic view illustrating the Model used to characterise the nuclearites arrival speed to the ANTARES detector.

After establishing the minimum mass required to detect nuclearites with a clear and unequivocal signature in the proximity of the detector, it is then possible to choose the appropriate set of experimental *runs*<sup>1</sup> to be processed.

### 3.2.2 Run selection

Our analysis cover the period from 2009 till 2017, during this time, the detector was completely deployed and fully operational with its 12 detection lines. however, the detector was running with its partial configuration (i.e. before June 2008). ANTARES, was constantly recording experimental data; the collection of data for a period of time is known as a *run*. For runs before 2012, the duration of data gathered was around 3 hours per run, while for subsequent years it was approximately 12 hours. The reason pushing us to select runs for our analysis is that the experimental data recorder by the detector comprises all of the physical signals around the detector, in particular signal derived from <sup>40</sup>K decay and bioluminescence. practically, the speed of nuclearites is too slow in comparison to other relativistic particles, as a result, it is difficult to recognize our signal in the presence of a low speed signature caused mostly by bioluminescence. It is preferable to conduct the analysis with a clean data-set by deleting runs with a high rate of biological activities as well as those with a large number of sparking runs.

The set of runs used for our analysis are refereed to as *silver runs*, to be considered so, they should satisfy a set of conditions based on the run parameters which are calculated during the data acquisition and stored on the database for each particular run. The burst fraction is calculated over the entire run it represent the average value over all the PMTs of

---

<sup>1</sup>A run (plural runs), for this analysis, mean a period of data taken of the ANTARES detector

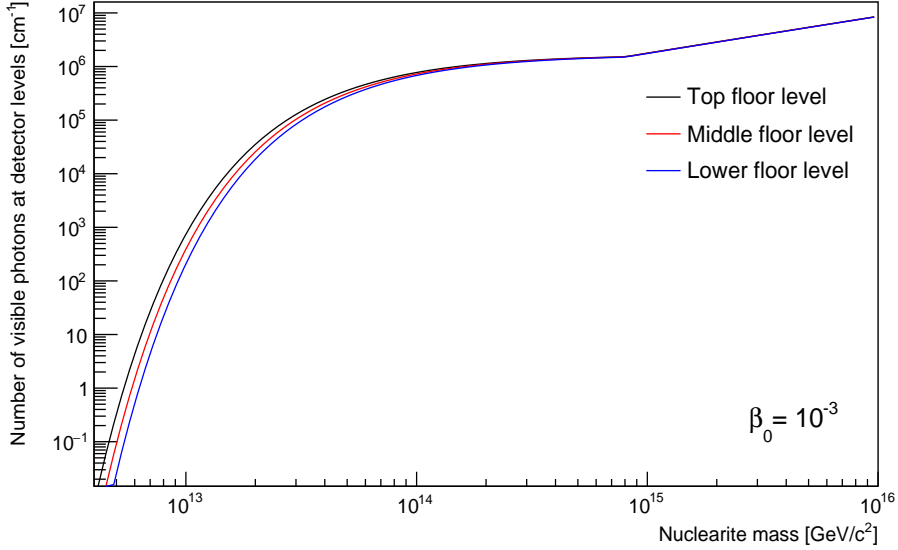


Figure 3.2: Number of visible [300-600 nm] photons per centimeter generated by vertically incident nuclearites at different detector levels. For masses higher than  $8.4 \times 10^{14} \text{ GeV}/c^2$  all electrons must be inside the quark bag. The cross section starts to increase with the nuclearite mass due to the change in the cross section, resulting in more generated visible photons.

the fraction of the number of TimeSlices where the rate was higher than the baseline plus 20%. The mean rate is defined as the average rate of all ARSSs that measured a rate higher than 10 kHz. To be silver, a run should have a baseline rate less than 120 kHz (minimum constant rate) and a burst fraction (due to bioluminescence) less than 40%.

Each runs in the period 2009-2017 satisfying the above conditions is then selected to be processed. 100 down word going events are simulated per run. The methods used to simulate the events are explicitly explained in the next subsection.

### 3.2.3 Event simulation

A generation volume in the shape of a 548 m-radius hemisphere filled with water has been used to simulate downward-moving nuclearites events that penetrate at the depth of the ANTARES telescope. The hemisphere's radius was chosen so that the closest storey would be two light-attenuation lengths far from the surface of the hemisphere. According to Fig. ??, the suggested shape envelops the detector's instrumented volume symmetrically. Each simulated event consists of a nuclearite generated with a random position across the generation volume's surface and a random zenith and azimuth angle that determines the nuclearite's direction,  $(\theta, \varphi)$ . See Fig. (Fig. ??) for reference. Using Eq. ??, the speed of the particle at the point of generation is calculated while accounting for the path that would be crossed through the atmosphere and the water just above the previously generated position on the hemisphere given that nuclearites are falling on Earth with Galactic velocities ( $\beta = 10^{-3}$ ).

The particle is propagated along its direction with steps  $dt$  set to 2 ns after the position, direction, and velocity have been established. The position and speed, as well as the energy loss, the expected number of visible photons and the number of hits for each OM, are

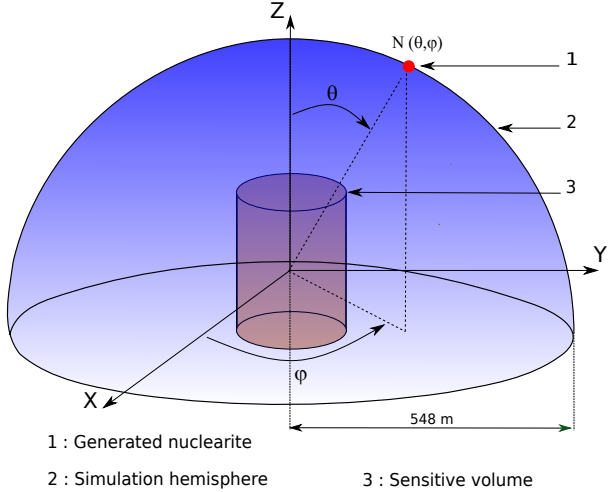


Figure 3.3: Geometry utilized in the Monte Carlo simulation to generate the nuclearites events. Nuclearites are produced on the hemisphere’s surface with a random position and direction they then spread in all directions to the detector (sensitive volume) using randomly generated direction angles  $\theta$  and  $\varphi$ .

evaluated at each iteration using the formulas introduced in section ?? and the simulation tools for light propagation and PMT digitization. The simulation is interrupted when the particle departs the simulation hemisphere or when the optical energy loss of the particle (averaged across the time step) is insufficient to generate sufficient visible photons (lower than 3 eV).

The main background source for neutrino telescopes is atmospheric muons. They are formed during the decay of charged mesons that are the result of primary cosmic ray interactions with atmospheric nuclei. The primary background for nuclearite events is composed of downward-moving atmospheric muon events. They are generated using the MUPAGE event generator [82], and are propagated in bundles down to five km of water equivalent. The basis of MUPAGE is a set of parametric formulas that determine the flux and angular distribution of bundles of muons in water or ice. The muon multiplicity and the multi-parameter dependent energy spectrum are taken into consideration by the generator. Reference [82] contains more information on the MUPAGE code.

The last phase of the simulation chain aims to transform each PMT hit into a data stream with the same format and environmental exposures as real data. To accomplish this objective, the light generated by physics events is combined with the ambient optical background created by bio-organisms and the decays of  $^{40}\text{K}$ . (nuclearites or atmospheric muons). Local variations in environmental circumstances might also have an impact on how particular optical modules respond. As a result, the time evolution of the data acquisition is accurately reproduced, as mentioned in [83]. The information related to the recorded hits, such as the hit number, hit amplitude, hit time, and the position of the PMT which recorded the hit, are stored in the ROOT files produced by the trigger processing of the Monte Carlo events using a dedicated program named *TriggerEfficiency*, analogous to the data stored in the raw data files. Data and Monte Carlo comparisons were initially carried out using a portion of 10% of the chosen data (runs with a number ending with 0) for a variety of parameters, including the distribution of snapshot duration and the number of L0 and L1

hits.

### 3.2.4 Triggers and event selection

The front-end electronics boards could produce a signal at the anode when photons of any provenance fall on the optical sensor of the PMT photocathode. This signal can then be converted into a digital format, capturing time and charge and store the data in a structure known as a *hit*. All the hits leaving a charge greater than a minimum threshold of 0.3 photoelectrons (p.e.) are classified as L0 and sent to the shore in order to determine potentially relevant events that are kept on disk using a dedicated trigger algorithm [81]. A single hit with a high amplitude that exceeds a predetermined high-threshold requirement (set to 3 p.e. or 10 p.e. depending on the data acquisition conditions) or a coincidence of two L0 hits from the same floor within a time interval of 20 ns are both classified as L1 hits.

To filter its data, ANTARES uses a variety of trigger algorithms. The standard muon triggers T3 and 3D are employed in this research to identify the nuclearites signal. The T3 trigger is defined as the occurrence of at least two L1 hits in 3 consecutive storeys within a coincidence time window, while the 3D trigger needs at least five causally related L1 hits within  $2.2 \mu\text{s}$  of one another. If the two floors are adjacent, the coincidence time window is set to 100 ns, and if they are not, it is 200 ns.

A preliminary analysis has been conducted to assess whether ANTARES filters could capture nuclearites and other low-speed particles. The expected number of visible photons per centimeter as estimated by Eq. ?? is shown in Fig. ?? as a function of nuclearite mass. Three positions of the ANTARES detector at various levels (top, middle, and bottom of the detector string) are taken into consideration. Nuclearites are presumed to reach the detector vertically in that figure, with an initial velocity of  $\beta = 10^{-3}$  at the top of the atmosphere. Nuclearites that have a mass of  $10^{13} \text{ GeV}/c^2$  produce fewer than  $10^3$  photons per centimeter. A muon emits  $\sim 350$  Cherenkov photons per cm<sup>2</sup> (within the sensitivity range of PMTs) as a point of comparison. As a result,  $4 \times 10^{13} \text{ GeV}/c^2$  is thought to be a threshold mass for nuclearites detection as it produces a considerable light yield.

All PMT pulses that occurred during  $2 \mu\text{s}$  of the first triggered hit and  $2 \mu\text{s}$  of the final triggered hit are recorded when an event is triggered. A *snapshot* is the term used to describe this collection of data. When two or more events have some hits that overlap, the events are combined to produce a larger snapshot. Both T3 and 3D triggers are envisaged to acquire a succession of overlapped snapshots for nuclearites since they would usually pass through the detector at low velocities. The number of snapshots recorded for each nuclearite event for the masses taken into consideration is shown in Fig. ???. Compared to low mass events, higher mass nuclearite events exhibit less snapshots. this is mainly because of how fast the particle is moving inside the detector. The particle generates light as it passes through the detector, and this light may cause the detector to be triggered. For the same occurrences, low mass nuclearites continuously trigger the device. As a result, for this low mass nuclearite event, the DAQ system captures more snapshots.

The nuclearite mass and its direction of arrival determines the overall efficiency of the ANTARES triggers. The percentage of events with mass  $> 10^{14} \text{ GeV}/c^2$  recorded by the T3 or the 3D triggers ranges from 60% to nearly 100% when averaged across an isotropic flux from the upper hemisphere. For lower masses, the efficiency falls down. The overall efficiency, which is shown in Table ?? for each nuclearite mass, is calculated by dividing the

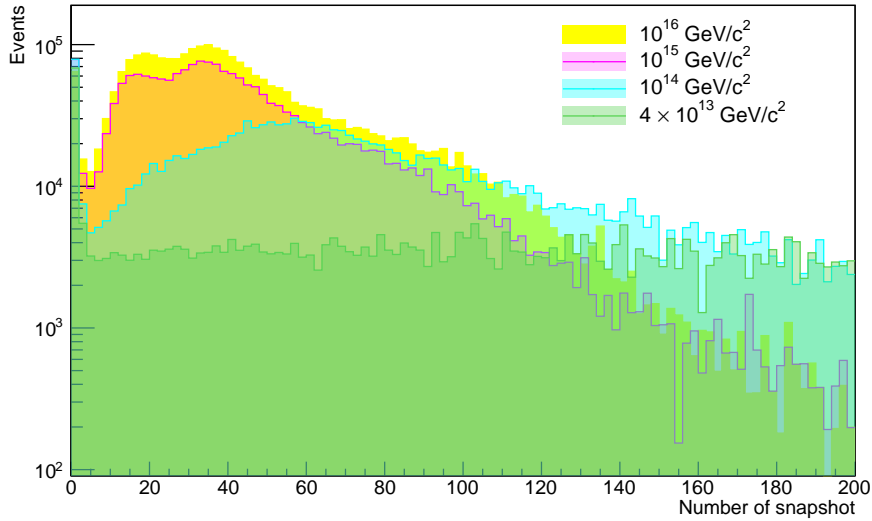


Figure 3.4: Distribution of the number of snapshots for nuclearite events which have been triggered for the masses in consideration. Since they traverse the detector more rapidly than low velocity events with a high number of snapshots per event, nuclearites with higher masses have less snapshots per event.

total number of triggered events by the total number of generated events. For nuclearites with a mass of  $4 \times 10^{13} \text{ GeV}/c^2$ , the trigger efficiency rises from 25% of produced events to almost 97% for higher masses. The energy loss of these particles from the generating surface of Fig. ?? before they reach the sensitive volume of the detector and the fact that clipped particles are not bright enough both contribute to the low trigger efficiency for low masses. When nuclearite masses are high, these effects vanish. We display the trigger efficiency (TE) for the T3 and 3D triggers as well as their combination as a function of the number of L1 hits for all nuclearite masses that were considered throughout the analysis period in Fig. ???. T3 trigger, as defined, often filtrate nuclearite events with low L1 hits, whereas 3D trigger typically filtrate events with high L1 hits. Both triggers are responsive to cases involving high number of L1 hits. It is important to note that an event has the potential to trigger both T3 and 3D at the same time, and the TE depicted in Fig. ?? accounts for this. The TE plot indicates that nuclearite analysis may indeed be performed using standard muon triggers. We employ the events triggered by the “T3 and/or 3D” triggers, which integrate events representing nuclearites in all masses and offer a significant amount of statistics, in order to conduct a consistent non ambiguous study on the nuclearites signature in ANTARES.

### 3.3 Event selection and analysis

In order to avoid any biased results, a fraction of 10% of real data has been used to compare experimental data to the Monte Carlo simulation and to compute the sensitivity of the detector to nuclearites. As the detection of nuclearite signals could be impacted by bioluminescence, a strict anti-bioluminescence cut is applied. A selection is made for each data taking period of several hours, which is called “run”. To be considered for this analysis, a “run” should not have more than 20% of the detector elements affected by bioluminescent bursts at any moment. After applying this filter, 839 days of lifetime in

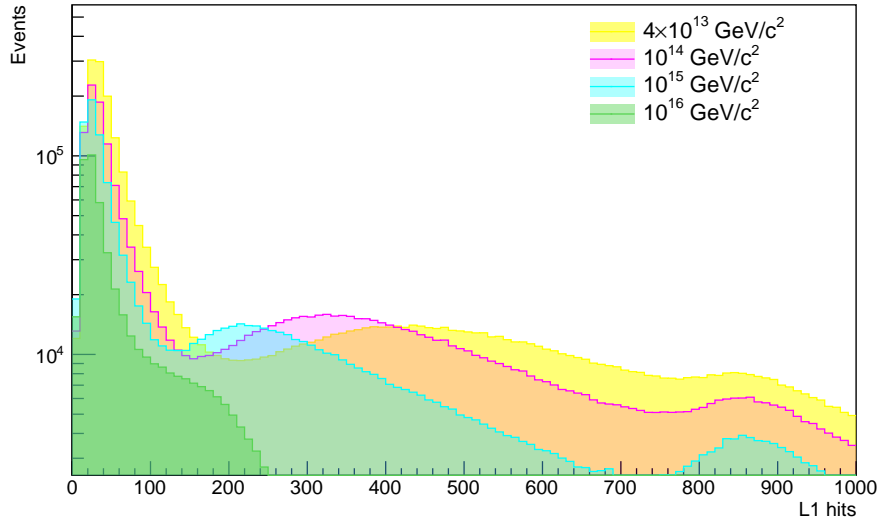


Figure 3.5: Number of L1 for nuclearites with the simulated mass. The amount of events is mass dependent and it is encasing with the mass.

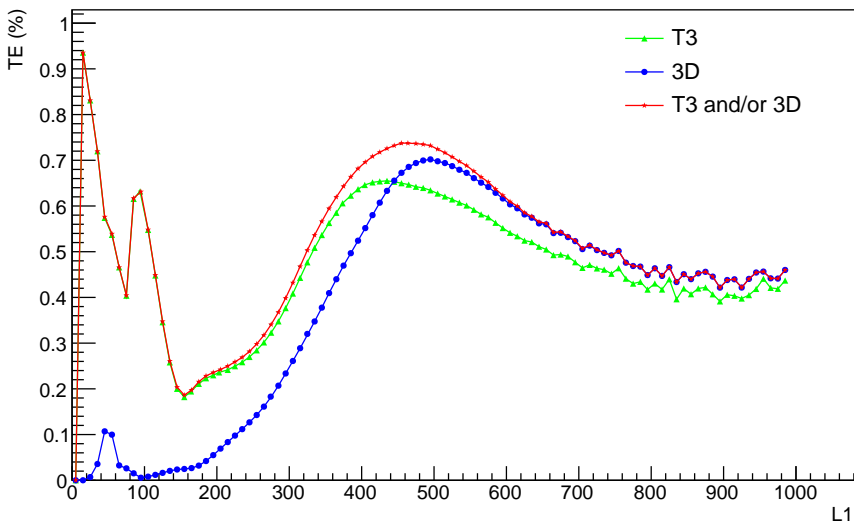


Figure 3.6: As a function of L1 hits, the trigger ratio for T3, 3D, and “T3 and/or 3D” triggers for combined events of the considered nuclearite masses in the period 2009-2017. The ratio for a particular trigger is calculated by dividing the number of triggered events with the considered trigger individually by the total number of triggered events with all the included triggers.

the period 2009-2017 are selected.

### 3.3.1 Discrimination variables

Only events that satisfy the predefined T3 or the 3D trigger conditions from a set of pre-selected runs are included in this analysis. To isolate nuclearite signals, two discrimination variables are utilized. The first variable, denoted as  $\log_{10}(nhits3)/nfloor$ , is a dimensionless quantity that is proportional to the total amount of photons reaching the Optical Modules (OMs) of the detector. For a given event,  $nhits3$  represents the number of hits with a charge of at least three photoelectrons, while  $nfloor$  is the number of floors in the detector that record at least one hit for the event. The second discrimination variable is the event duration,  $dt$ , which denotes the transit time of the event in the detector and is calculated as the time between the first and last hits in the event. Nuclearites, being slow and heavy particles, are expected to have a significantly larger transit time in the detector than background relativistic particles. The distributions of both discrimination variables are shown in Figure ?? and Figure ?? for atmospheric muons and nuclearites of varying masses, respectively.

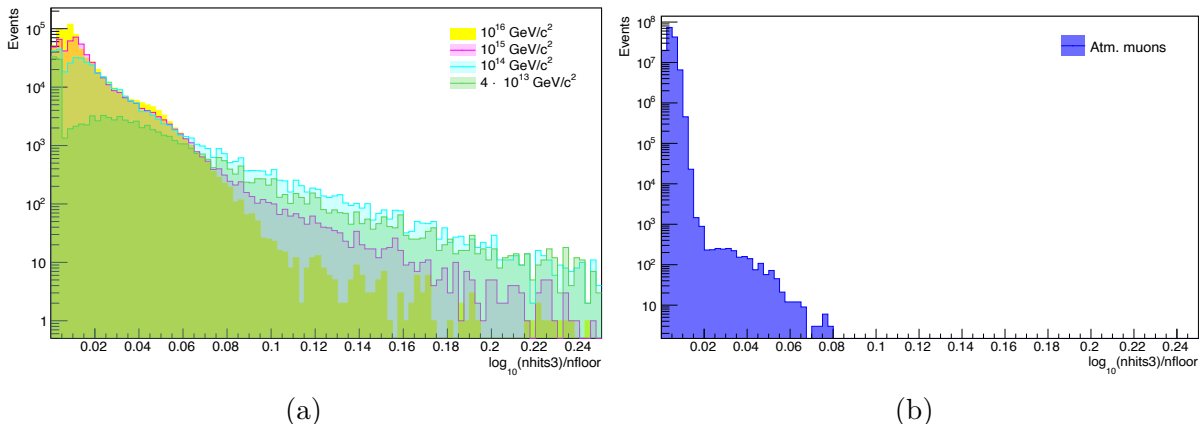


Figure 3.7: Distribution of the  $\log_{10}(nhits3)/nfloor$  variable form simulated nuclearites events (??) and for atmospheric muons events (??). Nuclearites are characterized by large values of  $\log_{10}(nhits3)/nfloor$  compared to muons which have a low luminous weight in the apparatus.

Due to their low speed and high masses, nuclearite events would generate a high number of visible photons around the detector in a relatively long period. They are expected to have high values for the  $\log_{10}(nhits3)/nfloor$  variable as  $nfloor$  is constrained by the total number of the detector floors. However, high energy atmospheric muon events characterized by low number of L0 hits affect our signal region in the  $\log_{10}(nhits3)/nfloor$  variable and they must be removed. Fig. ?? illustrates  $\log_{10}(nhits3)/nfloor$  versus  $\log_{10}(L0)$  for simulated atmospheric muon events.

**Preliminary quality cut on L0** A preliminary quality cut requiring at least 300 L0 hits for each event has been applied to clean our sample. This cut removes events firing with high amplitude the few PMTs present in a restricted region of the detector because of (for instance) a cascade of secondary particles induced by an atmospheric muon. Table ?? summarizes the efficiency of the L0 cut for atmospheric muons and different masses of nuclearites. The efficiency is defined as the number of events after applying the L0 cut to

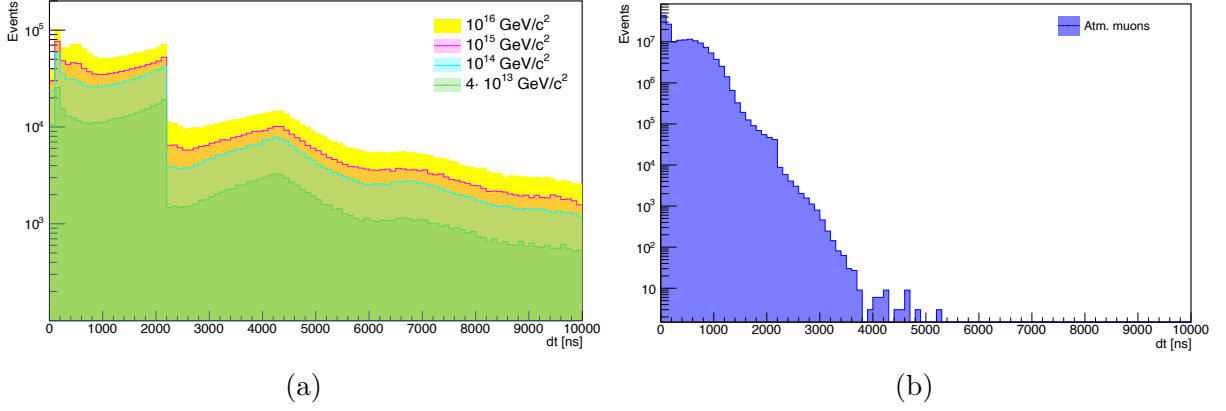


Figure 3.8: The  $dt$  distribution for simulated nuclearites events of various masses (??) as well as for simulated atmospheric muons (??). Unlike to muons, which cease at about 5000 ns, nuclearites have large values of the  $dt$  variable that reach milliseconds. In practice, this is caused by the nuclearites' slow speed inside the detector.

the total number of triggered events. The L0 cut removes 84% of simulated atmospheric muon events.

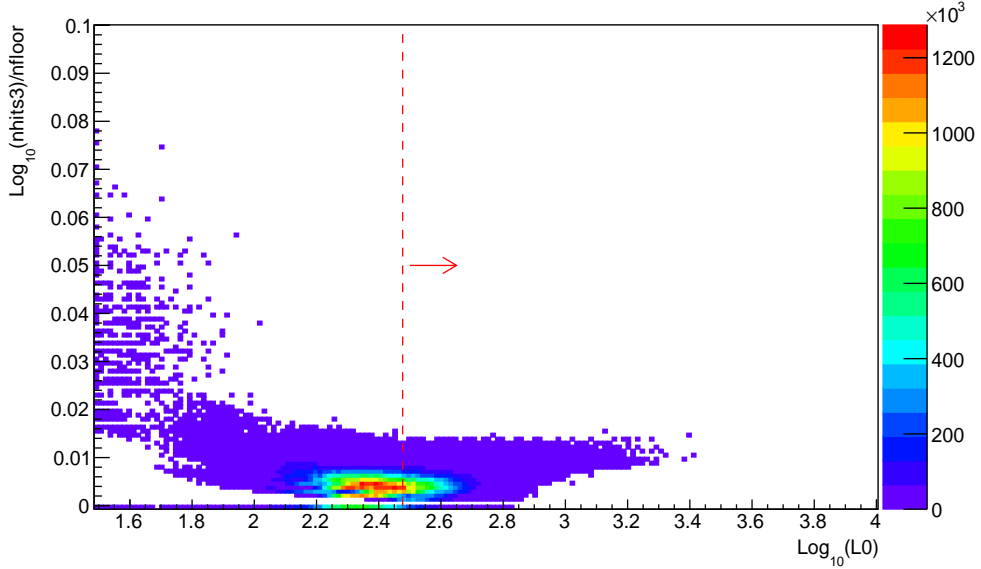


Figure 3.9: Distribution of  $\log_{10}(nhits3)/nfloor$  versus  $\log_{10}(L0)$  for simulated atmospheric muons, the palette of colors represents the number of events for 839 days of livetime. The cut at 300 L0 hits (red dashed line) allows to reject the events with high values of  $\log_{10}(nhits3)/nfloor$  characterized by a low number of L0 hits. Only 16% of simulated atmospheric muons events survives the L0 cut.

### 3.3.2 Selection efficiency

In order to discriminate nuclearite events from the background, variables that reflect the behavior of these particles in the detector were used. These particles are expected to generate a high number of visible photons at the vicinity of the detector. This could result in a high number of fired floors with a high amplitude during a relatively long period. Fig. ?? illustrates the  $\log_{10}(nhits3)/nfloor$  variable and shows the L0 cut effect on both data

and atmospheric muons for 839 days of livetime. From the right plot, most nuclearite events for different masses have a high value of this variable compared to muon events which stops at around  $\sim 0.015$ , while a good agreement between the 10% of open experimental data and MC simulation is observed. The signal of these particles is also characterized by a long snapshot duration.

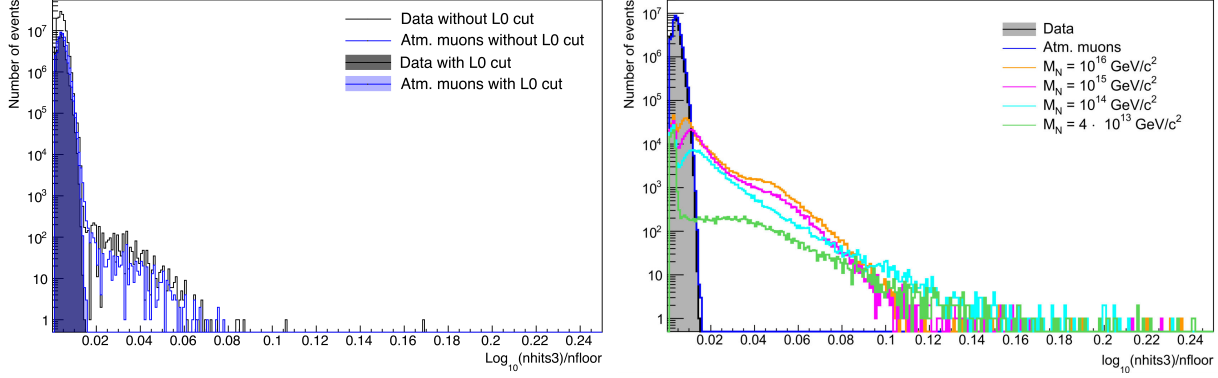


Figure 3.10: Left: Distribution of the discrimination variable  $\log_{10}(nhits3)/nfloor$  without and with the cut  $L0 \geq 300$  on the total number of PMT hits using 839 days of livetime. The black histogram corresponds to real data, while the blue one refers to simulated atmospheric muons. Right: The same distribution with the  $L0 \geq 300$  cut for data, simulated atmospheric muons and simulated and triggered nuclearites (other colors).

In order to reduce the background, events are selected based on both parameters characterizing the signal. Fig. ?? shows  $\log_{10}(nhits3)/nfloor$  versus  $dt$  (measured in ns) for each nuclearite mass. Most simulated nuclearite events show a long duration,  $dt$ , typically higher than  $3 \times 10^3$  ns, combined with high values of  $\log_{10}(nhits3)/nfloor$ . The scatter plots in Fig. ?? show that both variables are well suited to discriminate between nuclearites and background from cosmic ray muons. By applying the appropriate cuts, the region dominated by the noise could easily be discriminated from the region relevant for our signal. However, in order to maximize the performance of these cuts, an optimisation is required. The methods used to optimize the cuts are discussed in the next subsection. Table ?? shows the selection efficiency of the optimized cuts for each nuclearite mass.

Nuclearite mass ( $\text{GeV}/c^2$ )	$10^{16}$	$10^{15}$	$10^{14}$	$4 \times 10^{13}$	Atm. muons
Trigger efficiency (%)	97	88	61	25	9.5
L0 cut efficiency (%)	40	42	31	17	15
Selection efficiency (%)	20	20	28	75	0
Final efficiency (%)	7.8	7.4	5.3	3.2	0

Table 3.1: Selection efficiencies as a function of the nuclearite masses at the different steps discussed in the text. The trigger efficiency in the first row is respect to the number of simulated events, while the values in the following rows is respect to the previous one.

### 3.3.3 Variables optimisation

In order to achieve the best sensitivity of ANTARES to nuclearites without any bias, the Model Rejection Factor (MRF) is used [84] to optimize the cuts on the discrimination variables taking into account the statistical fluctuations in the simulated atmospheric muons

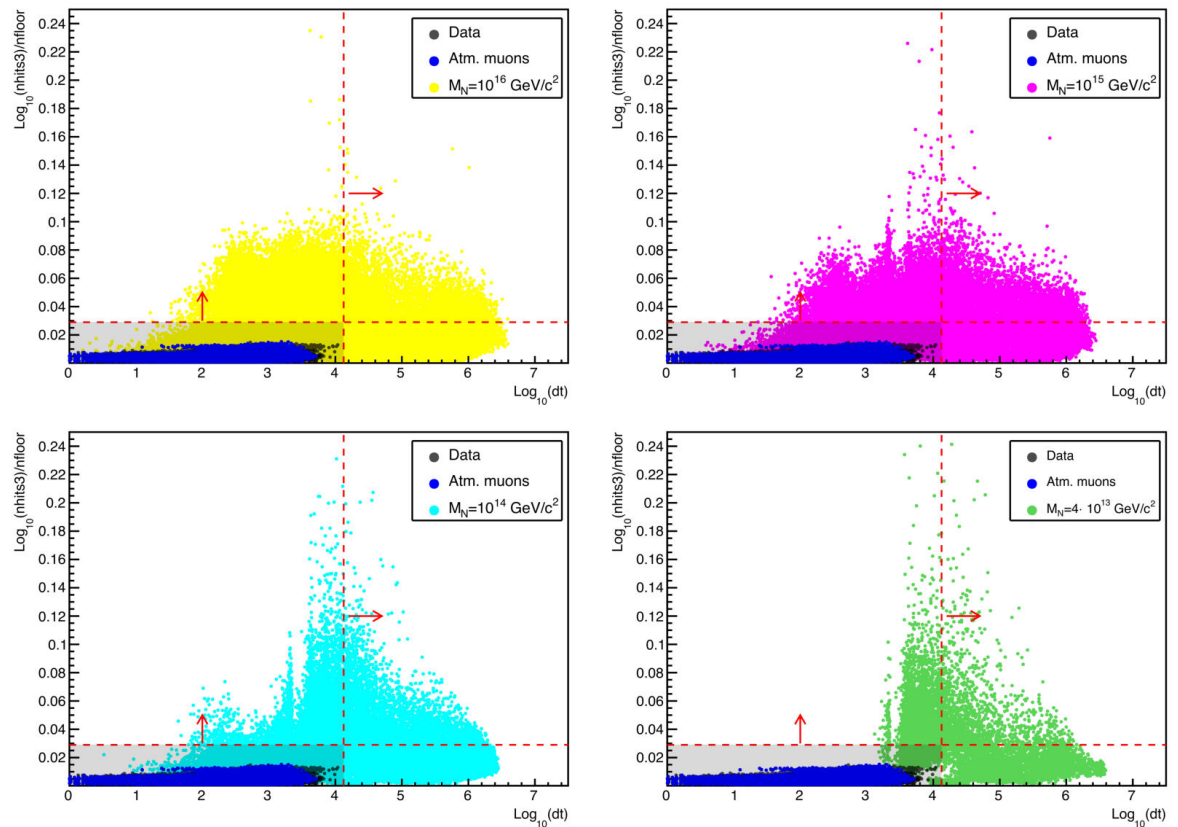


Figure 3.11: Scatter plot of  $\log_{10}(\text{nhits3})/\text{nfloor}$  versus  $\log_{10}(dt)$  for events with at least 300 L0 hits. Real data in black, atmospheric muons in blue, and for different nuclearites masses. The red dotted lines represent the optimized cuts on both discrimination variables.

distributions. The Model Rejection Factor technique consists of varying the cuts with small steps until the minimum of MRF is reached, this minimum corresponds to the values that gives the best sensitivity.

The sensitivity at 90% confidence level (C.L.), denoted as  $S_{90}$ , is computed using the Feldman-Cousins method [85], assuming events with a Poissonian distribution:

$$S_{90} = \frac{\bar{\mu}_{90}(n_b)}{S_{eff} \times T}, \quad (3.1)$$

$$\bar{\mu}_{90} = \sum_{n_{obs}=0}^{\infty} \mu_{90}(n_{obs}, n_b) \times \frac{n_b^{n_{obs}}}{n_{obs}!} \times e^{-n_b}, \quad (3.2)$$

$$S_{eff} = \frac{n_{Nuc}}{\Phi_{Nuc}}, \quad (3.3)$$

where,  $n_{obs}$  is number of observed events and  $n_b$  the number of expected background events from all the dataset.  $T$  is the duration of data taking corresponding to the 2009-2017 period in seconds,  $n_{Nuc}$  represents the number of nuclearites remaining after applying the optimized cuts, and  $\Phi_{Nuc}$  represents the flux of generated nuclearites.

The best values on  $dt$  and  $\log_{10}(nhits3)/nfloor$  are those minimizing the MRF for each nuclearites mass. Fig. ?? shows an example of the MRF for the higher nuclearites mass as function of the selection parameters. The values that minimise the MRF for the four values of the simulate nuclearite masses are reported in the first two rows of Table ???. The event fraction passing all the selection criteria is reported in the third row, while the number of remaining background events after the selection cuts and the value of the MRF are in the rows 4 and 5, respectively.

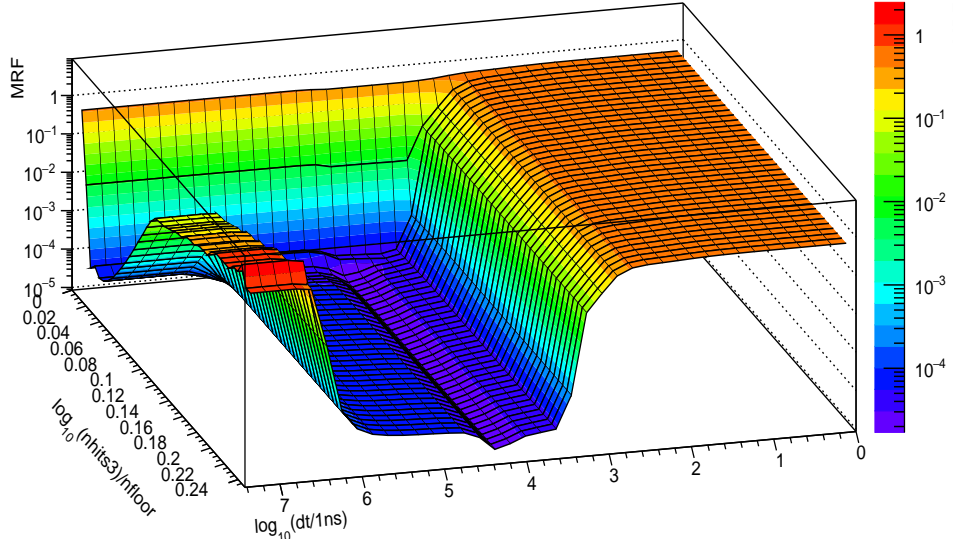


Figure 3.12: MRF as function of  $\log_{10}(nhits3)/nfloor$  and  $dt$  for the higher nuclearites mass ( $10^{16} \text{ GeV}/c^2$ ).

## 3.4 Analysis results

### 3.4.1 Systematic uncertainties

The De Rujula and Glashow study, [62], provides the light production per unit length of the track and the particle crossing time in the detector, which are the primary parameters used in experimental searches for nuclearites. The luminous efficiency  $\eta$  calculated for transparent water in the [550-330] nm wavelength range was utilized in the current research, [62]. This wavelength range falls well within ANTARES PMTs' sensitivity range. The energy distribution of photons follows the black-body distribution, which for nuclearites arriving in the detector with masses above the threshold of  $4 \times 10^{13}$  GeV/c<sup>2</sup> has a peak at wavelengths shorter than 300 nm. The intensity of Cherenkov emission produced by relativistic particles is proportional to  $1/\lambda^2$ , and also in this case short wavelengths dominate. When the two different spectra are folded in our simulations with the water transmission [86] and the quantum efficiency the PMTs as a function of the wavelength [87], the differences between the two different spectra in the photoelectron yields on the PMTs are within 30-40%. The minimum nuclearite mass ( $4 \times 10^{13}$  GeV/c<sup>2</sup>) considered in the analysis ensures that the number of emitted photons per cm are of the order of  $10^6$  at each detector depth: as a consequence, the trigger and selection efficiencies are not affected by the variation in the emission spectra of visible photons.

The uncertainties for the signal produced by atmospheric muons are derived from the statistical fluctuations in the signal region for both discrimination variables; this is recovered by extrapolating the distributions using a Landau type function (see ref. [88] for further details). Systematic uncertainties on the effect of atmospheric muon events are mainly due to the detector description and to the knowledge on the environmental parameters. These are mainly related to the uncertainties on the angular acceptance of the optical modules and on the light absorption and scattering lengths in the sea water [86, 87]. Hence, an overall of +35% -30% effect on the expected atmospheric muon rate results from  $\pm 15\%$  as a maximum of uncertainty on the optical module acceptance and  $\pm 10\%$  on the light absorption in water along the entire wavelength spectrum [89]. The computation of the number of observed events  $n_{obs}$  and the number of expected background events  $n_b$  given in equation ?? incorporate systematic uncertainties using the method described in [90].

### 3.4.2 Unblinding results

After unblinding the remaining 90% of data not used for testing the optimisation procedure, no event is present in the region beyond the optimised cuts. Since no event is found, the upper limit on the flux of nuclearites at 90% CL is computed as

$$\phi_{90} = \frac{\mu_{90}(n_{obs}, n_b)}{S_{eff} \times T}, \quad (3.4)$$

where the confidence interval at 90% CL  $\mu_{90}(n_{obs}, n_b)$  is computed from the unified approach of Feldman-Cousins [85].  $S_{eff}$  is defined in equation ?? and  $T$  is the livetime of the analysis.

The 90% CL flux upper limit values reported in Table ?? include both statistical and systematic uncertainties.

Nuclearite mass ( $\text{GeV}/\text{c}^2$ )	$10^{16}$	$10^{15}$	$10^{14}$	$4 \times 10^{13}$
Best cut on $\log_{10}(dt/1\text{ns})$	$\geq 4.27$	$\geq 4.27$	$\geq 4.27$	$\geq 4.35$
Best cut on $\log_{10}(nhits3)/nfloor$	$\geq 0.029$	$\geq 0.024$	$\geq 0.024$	$\geq 0.024$
Remaining nuclearites (%)	6.9	7.0	4.7	2.8
Remaining background	1.05	0.35	0.35	0.31
MRF	$1.6 \times 10^{-5}$	$2 \times 10^{-5}$	$2.7 \times 10^{-5}$	$4.12 \times 10^{-5}$
Flux upper limit 90 %CL ( $\text{cm}^{-2} \times \text{sr}^{-1} \times \text{s}^{-1}$ )	$6.6 \times 10^{-18}$	$8.1 \times 10^{-17}$	$1.1 \times 10^{-17}$	$1.6 \times 10^{-17}$

Table 3.2: Values of the optimized parameters and the results of the MRF and upper limits for the different nuclearite masses for 839 days of livetime.

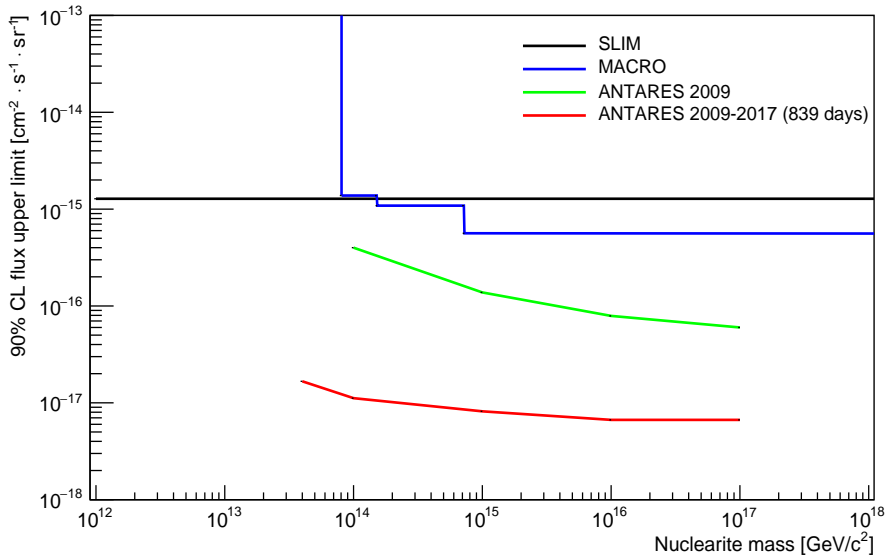


Figure 3.13: Upper limit on the flux of nuclearites with Galactic velocities ( $\beta = 10^{-3}$ ) in red line, using 839 days of livetime in the period 2009-2017 with the ANTARES detector. The green line corresponds to a previous ANTARES result obtained with a smaller data sample [91]. Results from other experiments, MACRO [92] and SLIM [93], are also shown.

The obtained upper limit (UL) on the nuclearite flux for  $T = 839$  days of livetime of the ANTARES detector is shown in Fig. ???. For masses higher than  $10^{16} \text{ GeV}/\text{c}^2$ , nuclearites emit more light. Therefore, the limit of the last test point can be taken as a conservative limit also for higher nuclearite masses, up to the value of  $\sim 10^{17} \text{ GeV}/\text{c}^2$  where detector saturation effects start to occur.

### 3.5 Conclusion

This study uses information gathered by a neutrino telescope to search for an exotic particle. The device was designed to detect relativistic particles, however this research demonstrates it has the ability to record signals from other sources. With galactic velocities, nuclearites with considerable mass ( $4 \times 10^{13} \text{ GeV}/\text{c}^2$ ) can reach the ANTARES detector and produce light in the wavelength range of its PMTs. Assuming a velocity of ( $\beta = 10^{-3}$ ) at the entrance in the Earth's atmosphere, nuclearites with masses ranging from  $4 \times 10^{13} \text{ GeV}/\text{c}^2$  to  $10^{16} \text{ GeV}/\text{c}^2$  were simulated in ANTARES. On an abstract hemisphere that was exploited as a generation volume enveloping the detector symmetrically from the top,

nuclearite were generated. 100 nuclearites events with randomly generated positions are taken into account for each simulated run. The particle's direction is similarly determined by two randomly generated angles ( $\theta, \varphi$ ). The nuclearite now proceeds in its generated direction from its generated position with fixed intervals of 2 ns, examining the PMT's responsiveness as well as the particle's speed, energy loss, and expected number of visible photons at each iteration. When the particle leaves the hemisphere or when its optical energy loss deteriorates to the point that no more visible photons can be produced, the simulation comes to an end.

Using two discrimination variables, the hypothetical particle is distinguished from any background sources. The background distribution in the signal region has been cleaned using a preliminary cut on the number of L0 hits. With a low number of fired floors and a high number of  $nhits3$ , atmospheric muons were able to be removed using this L0 cut. The limits on nuclearites flux as a function of the nuclearite mass at 90% C.L. are established using nine years of data acquired by ANTARES using the Feldman-Cousins approach, and the cuts on the discrimination variables that allow for this selectivity are optimized using the Model Rejection Factor technique.

These results represent an important step forward in the search for nuclearites and demonstrate the power of advanced data analysis techniques in particle physics research. The success in isolating the nuclearite signal from background sources provides a strong foundation for future studies and underscores the potential of the ANATRES telescope for the detection of these mysterious particles. Further investigation and analysis will be necessary to confirm the existence of nuclearites and fully understand their properties, but the results presented here represent a significant milestone in this ongoing scientific endeavor.

The results of this research enhance previously reported results and constitute the strictest limits ever established for nuclearites traveling at Galactic velocities. The first ones obtained by a neutrino telescope, they are too. The outcomes of this research have been published in the the Journal of AstroParticle and Cosmology (JACP) [94]. Given that there are still five years of unexplored data from ANTARES, this work can be extended to include more data. Adding a new discrimination variable that permits more significant isolation would be another technique for improving the analysis. In its complete form, the successor, KM3NeT, would have a better effective area and more accurate angular resolution. It is incredibly encouraging to start looking at the signature of these particles in KM3NeT considering ANTARES was able to capture them.

# Chapter 4

## A Collaborative Effort: Contribution of Morocco in the construction of the KM3NeT neutrino telescope

### 4.1 Introduction

KM3NeT, which stands for Cubic Kilometre Neutrino Telescope, is a neutrino detection project that consists of two types of detectors: ARCA and ORCA. ARCA (Astroparticle Research with Cosmics in the Abyss) is a high energy KM3NeT detector located approximately 100 kilometers off the coast of Sicily at a depth of roughly 3500 meters that focuses on neutrino astronomy and astrophysical neutrino source detection. The other detector, ORCA (Oscillation Research with Cosmics in the Abyss), is dedicated to low energy research. It is located at a depth of 2450 m, some 40 kilometers from the France city of Toulon, and its principal interest is the study of atmospheric neutrinos.

We will provide a quick overview of the KM3NeT/ORCA detector in this chapter. However, the physics behind the neutrino detection process and the technology employed for KM3NeT/ARCA are identical. The size and vertical and horizontal spacing of the detector components of the two types of detectors are the only differences between them. The detector layout, construction, neutrino detection process, and other detector characteristics will be discussed. And, since Morocco contributes in the detector assembly via two sites devoted to integrating the so-called Digital Optical Module (DOM) in Rabat and the Base Module (BM) in Oujda, we will highlight the operations carried out in the two locations. The last part will mention current work involving the reconstruction of magnetic monopoles (MMs) with the ORCA detector.

### 4.2 KM3NeT/ORCA design

As previously mentioned in the introduction, the ORCA detector is specifically designed to detect atmospheric neutrinos with energies between 3 and 100 GeV, that is the range where oscillation effects are most perceptible. The spacing of the detector components, which is optimized for this energy range, results in a much denser instrumentation than the ARCA detector and, as a result, a much lower energy threshold. Exploring the neutrino mass

ordering is the primary objective of the ORCA project [95]. Notwithstanding, the detector can also investigate a variety of physics beyond the Standard Model.

KM3NeT is the successor of the ANTARES neutrino telescope. Taking advantage of the experience gained by 15 years of operation of ANTARES, its predecessor. ORCA will eventually consist of 115 Detection Units (DUs), each of whose bases is roughly arranged on a circle to form a cylindrical structure known as a Building Block. This structure specifies the detector active volume, which corresponds to the amount of seawater that highly sensitive light detectors can successfully monitor (In KM3NeT, the detection of neutrinos relies on the Cherenkov effect). Figure ?? presents an artistic representation of the arrangement of the ORCA building blocks.

18 Digital Optical Modules (DOMs) are vertically affixed on a structure called DU, which is fastened to the ocean floor. The DOMs are spaced at regular intervals. In order to deliver the stretching force, the DU has an anchor at the bottom and a buoy at the top, which ensures stability and prevents the DOMs from floating horizontally. In practice, it is uncommon to find a precisely vertical orientation because of water currents, and variations can be as much as a few degrees. Real-time information regarding the precise shape of each DU is provided by a group of acoustic and optical position monitoring devices, which may then be taken into account in high-level data processing. Launcher of Optical Modules (LOM), a specialized DU deployment tool, was created to improve accuracy and lower the cost of the DU deployment procedure, enabling the deployment of several lines in a single sea operation as lines are compressed. A wide range of technology advancements are included into KM3NeT, making it considerably more efficient and effective. The KM3NeT detectors must operate steadily and detect neutrinos with good resolution for at least 15 years in order to fulfill their scientific objectives. For the anticipated scientific objectives to be achieved, detector sizes ranging from megatonnes (ORCA) to gigatonnes (ARCA) are needed due to the intrinsic properties of neutrinos, such as the extremely low interaction cross section.

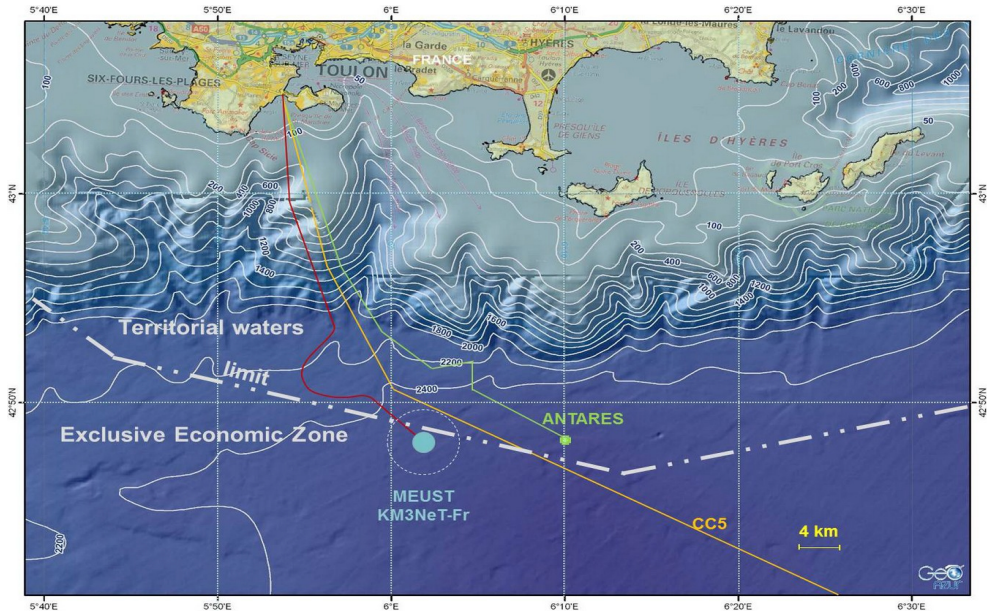


Figure 4.1: A map showing the KM3NeT/ORCA location in the Mediterranean Sea referred as “MEUST KM3NeT-Fr” on the map. The acronym MEUST stands for the Mediterranean Eurocentre for Underwater Sciences and Technologies

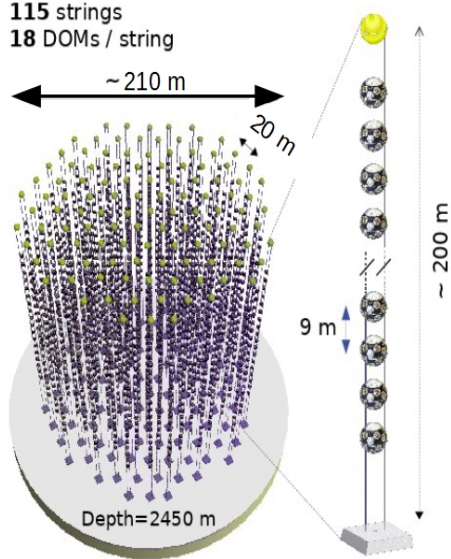


Figure 4.2: Layout of the KM3Net/ORCA detector showing the ORCA detector dimensions. A detection unit is seen on the right. The footprint, which is only a creative picture and does not accurately reflect the relative locations of the strings, is on the left.

#### 4.2.1 Digital Optical Module, the KM3NeT eyes

The Digital Optical Module (DOM), a pressure-resistant glass orb housing photomultiplier detectors (PMTs), calibration tools, and sophisticated electronics for the neutrino interaction-induced light detection, is the main detecting component of the KM3NeT telescopes. Fig. ?? displays the internal elements of a DOM. To determine the current DOM position, the piezo transducer receives acoustic signals from the sea bottom emitter. The inter-DOM time calibrations are performed using the LED nanobeacon. To stabilize the DU structure, there is adequate buoyancy in the air inside DOMs. Sensors for pressure, temperature, and humidity aid in keeping an eye on the situation within the DOM. Every DOM is outfitted with 31 Hamamatsu R12199-02 photomultipliers that are optimized for Cherenkov light detection and offer almost the whole  $4\pi$  solid angle coverage in order to detect light at the pitch-black depths of the abyss. Figure 2.5 displays a zoomed-in instance of a single PMT together with a built DOM. Due to the detector's concentration on up-coming particle detection, the bottom hemisphere contains more PMTs than the top one. One distinctive aspect of the KM3NeT technology is the multi-PMT unit. The other neutrino telescopes that are now in operation, such as IceCube, employ a single PMT with a wide diameter photocathode and often offer less accurate data, particularly with regard to the direction of photon arrival. The higher capacity of background rejection based on single-photon counting capability and coincidence logic is the second benefit of a photocathode area segmentation. The multi-PMT architecture further extends the possible lifetime of the project and minimizes the effects of a single PMT failure on detection efficiency. In the next sections we will present technical information about the DOM integration and testing methods.



Figure 4.3: Components for the Digital Optical Module are specified. Borrowed from [90].

#### 4.2.2 Photons propagation at the ORCA site

KM3NeT detectors uses the Cherenkov radiation to detect photons released when a neutrino interacts in their sensitive volume. When a charged particle moves through a dielectric media faster than the speed of light, Cherenkov radiation is produced. This occurrence is the result of the charged particle passing through and locally disrupting the electric field, which causes medium polarization. When the polarizing particle moves with a velocity  $v > c/n$ , where  $n$  is the refractive index, the excited atoms generate photons that are able to produce a wave front owing to constructive interference. Chapter ?? contains a detailed description of the Cherenkov radiation.

Cherenkov photons that are moving through the ocean are absorbed and dispersed. Light intensity is decreased by absorption, and photon paths are distorted by scattering, which minimizes the information available regarding the principal neutrino direction. An exponential distribution can represent both values.

$$I(\lambda) = I_0 e^{-x/l}. \quad (4.1)$$

### 4.3 Background sources

Due to their surroundings, KM3NeT detectors are exposed to a variety of background sources. ORCA (and also ARCA) catches events from bioluminescent species as well as from the  $^{40}\text{K}$  decay in the sea water. High energy atmospheric muons are another source



Figure 4.4: A close-up of a Hamamatsu R12199-02 photomultiplier (left) and an integrated ready-to-use digital optical module are shown on the (right).

of background events in the ORCA site.

### 4.3.1 Bioluminescence events

A chemical process that results in light within an organism's body causes bioluminescence. Light is emitted by a wide variety of marine species, including bacteria, algae, jellyfish, worms, crabs, sea stars and fish, it is a very widespread way of communicating in the deep waters. One DOM experiences an elevated hit rate from bioluminescence that can continue for many seconds. According to studies, the bioluminescence activity is primarily seen close to the detector structures, is connected to marine currents, and is seasonal.

A high rate veto can be used to reduce this noise. The data collection electronics in the DOM will veto any data collected on a PMT whose measured rate is more than 20 kHz and prevent it from being transferred to shore.

### 4.3.2 Potassium-40 decay events

For deep-sea neutrino telescopes, radioactive elements dispersed in seawater and their decay products are a significant source of background light. Potassium-40 ( $^{40}\text{K}$ ) is the most prevalent isotope in this group. Actually, there are around 400 milligrams of potassium per kilogram of saltwater, with a  $^{40}\text{K}$  abundance of 0.012%. There are two primary decay processes for this isotope:



Whenever  $^{40}\text{Cl}$  is the end product, the electron is released with an average energy of 560.2 keV and an endpoint of 1.3 MeV [113], which is significantly higher than the electron Cherenkov emission threshold of 250 keV. In the second procedure, a gamma photon with an energy of 1.4 MeV is released, which can then cause pair creation or electron ejection by Compton scattering. Each PMT is affected by the mentioned processes at a flat noise rate of around 7–8 kHz. Due to the randomness of the  $^{40}\text{K}$  generated PMT hits, it is simple to reject them by requiring the concurrence of impulses in at least two DOMs within a specific amount of time.

### 4.3.3 Atmospheric muons events

The atmospheric muons are the principal cause of background radiation for underwater neutrino telescopes. When primary cosmic rays collide in the upper atmosphere under the same hadronic processes as atmospheric neutrinos, atmospheric muons are produced via air showers. The decaying of the pion and kaon mesons serves as the principal component of the muon flux. A reduced integrated muon flux occurs at the Earth's surface as a result of the atmosphere length increasing from the vertical to the inclined direction, which causes higher energy loss of the sloped particles. The angled trajectory also has a higher probability of pion decay, which will increase the muon flux at intermediate energies. The longer-lived pions are more likely to interact before dying than the shorter-lived kaons, therefore when the energy increases, the percentage of muons from kaon decays similarly increases.

## 4.4 ORCA base module integration in Oujda

### 4.4.1 Introduction

A base module (BM) is a component that is located at the bottom of each detection unit (DU). Its role is to allow just one connection between a row of 4 DUs and the junction box node and four detection unit. To this end, ORCA has four types of BMs labeled A, B, C and D. The last one (D type) is also divided into two type depending on whether its DU contains the calibration unite (CU) or not.

Morocco contributes to the km3net building through two sites. The first one located here in Oujda is dedicated to integrate the base module while the second one is based in Rabat and it is used to integrate the digital optical module. At the time being, a group of researchers and technical stuff are currently waiting for the second BM after the successful assembling of the first base module in Oujda. There are, at this time, four sites that are integrating ORCA base module for KM3NeT: CPPM Marseille, LUPM Montpellier, IFIC Valencia and Mohammed First University in Oujda. Furthermore, a new site is in preparation at Demokritos at Athens.

### 4.4.2 ORCA Base Module

In the ORCA detector, 4 DUs needs to be connected to the node with just one connection. To meet this requirement, each DU is connected to a specific base module and the row of 4 DUs may have a Calibration unit at its end. There are five configurations for the ORCA base module depending on their position in the row and whether a CU is connected to the rows or not, as shown in the ORCA layout of figure ???. In the following, we explicitly describe the different types of the BM:

- Type A: is the type of BM connected in the first DU in the row, it collect the slow control (SC) data coming from the 4 DUs and multiplex it on a single optical fiber, and by using an optical component named *Interleaver* the fiber is connected to the node. In this configuration, the optical signal incoming to the BM is split with 80/20 ratio. 20% for the BM itself and 80% for the rest of the row.
- Type B: in this configuration the incoming signal is split into 70/30 ratio, 30% for the BM in consideration and the remaining 70% for the rest of the row.

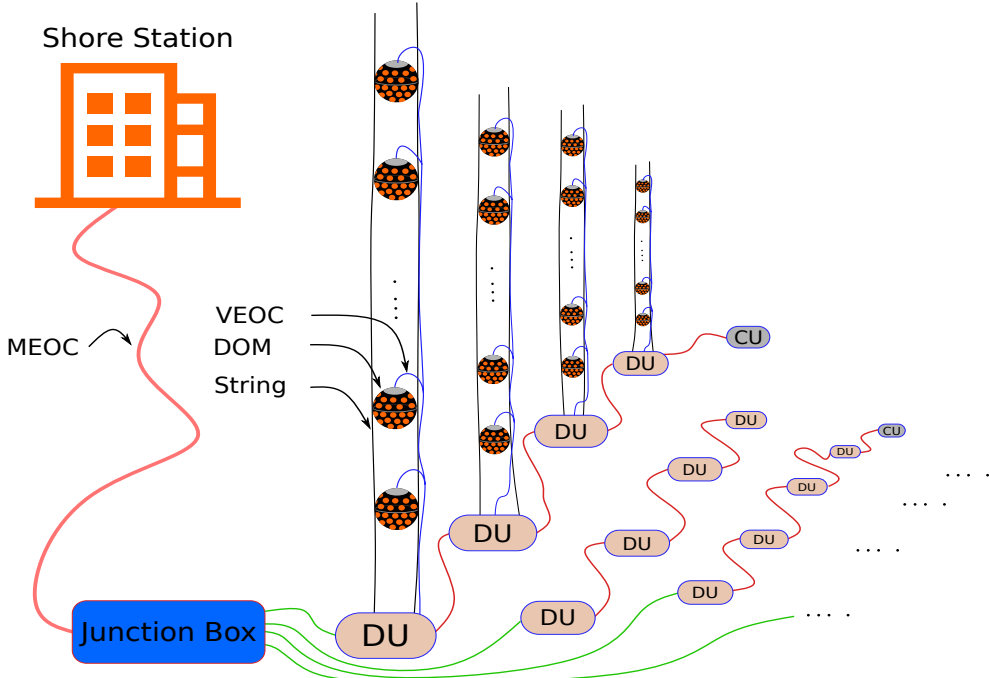


Figure 4.5: Schematics of the ORCA layout showing four DUs in a daisy chain configuration. Each daisy chain can be terminated with a calibration unit (CU). The base modules in the DUs are (from left to right) of type A,B,C and D.

- Type C: in this configuration the incoming signal is split into 60/40 ratio, 40% for the BM in consideration and the remaining 60% for the rest of the row.
- Type D with CU: in this case the incoming SC optical signal is split into 20/80 ratio, 80% for the BM in consideration and the remaining 20% for the rest of the row.
- Type D without CU: The incoming SC optical signal is fully dedicated to the BM.

#### 4.4.3 Base Module mechanics

Due to the nature of the environment where the BM will be placed, the BM mechanics should meet some requirements. To resist to the pressure surrounding this component, a choice of a titanium cylindrical container is made. This container is provided by an experienced company. Figure ?? show a schematic drawing of the container.

The container had to meet these specifications:

- Resistivity with a safety factor of 1.5 to the operational pressure (250 bars).
- Capable of withstanding corrosion for 15 years.
- Already approved product.
- Each product is pressure tested before delivery, and a certificate is included.
- Permit the base module to be connected to the DU, the seafloor infrastructure, and external instrumentation (hydrophone, LBL).

The BM cylindrical container is closed using connector flange and blind flange. To ensure water tightness, each flanges is connected to the container with two O-rings and three M6

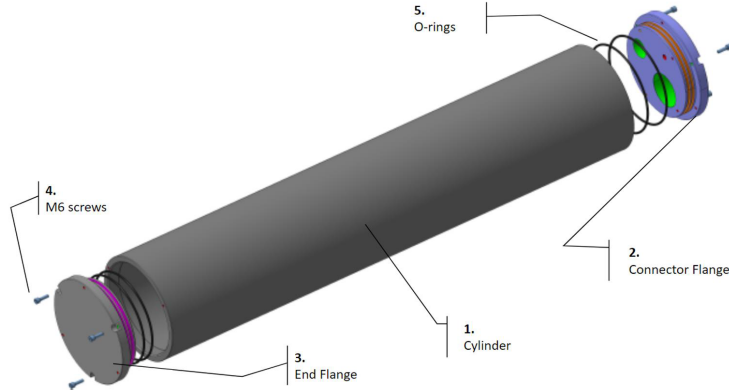


Figure 4.6: The BM container. It is supposed to resist to the high pressure at a depth of around 2500 meters in the Mediterranean sea.

screws. The standard flange is equipped with 3 holes to house the interlink penetrator, the *Vertical Electro Optical cable* (VEOC) penetrator and the hydrophone connector, see Figure ?? for the BM container flanges. This product is originally qualified from the pressure point of view. Nevertheless, some pressure tests have been done in order to qualify the flange after the machining of the holes.

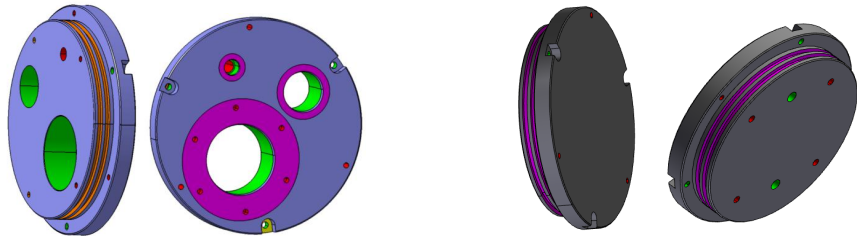


Figure 4.7: View of the ORCA base module flanges in schematic form. The connector flange with the three penetration holes is shown on the left for the two side of the front flange, and the end flange is shown on the right from both sides.

#### 4.4.4 Base module components

ORCA BM is made up of a variety of parts, but it can be segmented into three parts: the optical part, which holds the optical components, the electronic part, which contains the electronics required to carry out SC actions, and the distribution part, which distributes the electronic signals among the DU DOMs. The third part of the BM is the power unit, whose function is to supply the base module with electrical power (see Fig. ??).

##### 4.4.4.1 Optical part of the BM

- Erbium Doped Fiber Amplifier - EDFA

EDFA (*Erbium Doped Fiber Amplifier*) is a high power erbium doped amplifier. It is an active component that needs a 5VDC power supply and can communicate Rx/Tx with the shore station. This optical amplifier is used to increase the SC signal coming from the shore station and provide it to the DU optical modules. The main requirement for this component is to release an output power of 0 dBm whatever

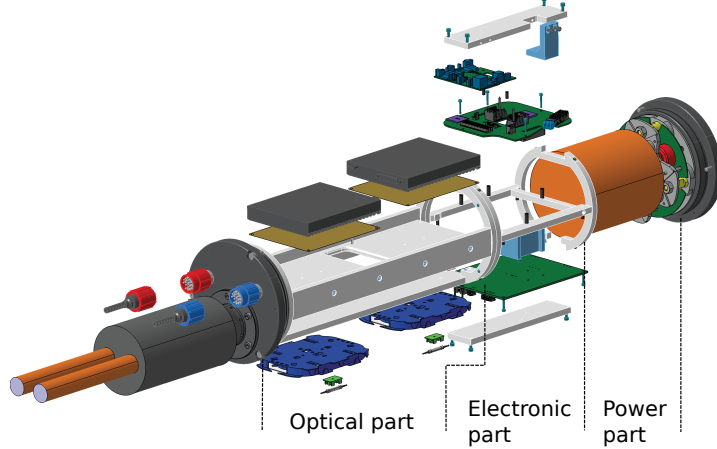


Figure 4.8: The optical part, electrical part, and power part of the BM are depicted in a schematic representation as well as other internal elements.

the input power is. ORCA BM uses the EDFA type C of this optical amplifier while there is other types of offshore EDFA (type L, M, X and type Y). Fig. ?? is showing a real picture of the EDFA.



Figure 4.9: Real picture of the EDFA type C ready for the integration on the first BM at Oujda.

- The Interleaver

The interleaver is a passive component that is installed only on the BM type A, its role is to interface the sets of 18 DOMs of the DU into a single optical fiber to the node.

- The DWDM multiplexer

DWDM (*Dense Wavelength Division Multiplexing*) multiplexer combine the output from several optical transmitters for transmission across a single optical fiber. It is a passive component and a BM type dependent due to the difference in the wavelength.

- The splitters

This is a passive component used to separate and distribute the optical signal inside the base module. There are two types of splitters: Several 1:2 type which split the signal in 2 with different branch ratio (10/90, 20/80, 40/60, 30/70). One 1:16 type which splits the SC signal.



Figure 4.10: Real view of two type splitters. On the top, 1:2 splitter and on the bottom 1:16 splitter.

- The Add & Drop

it is a passive 3 ways component which select and distribute a specified wavelength out from the input fiber. See Fig. ?? for a real view of this component.



Figure 4.11: Add and drop component, it is designed to only add or drop optical signals with a particular wavelength.

- The SFP transceiver (tunable DWDM version- TSFP)

Convert the Slow Control light signal received from shore into electronic signal for the base module CLB board. In the opposite direction convert the electronic signal into light signal to the shore. The working wavelength is not fixed but tunable.

#### 4.4.4.2 The electronic part of the BM

The CLB board, the FMC board, and the BCI make up the bulk of the electronic components of the BM.

- The CLB board

The main electronic board in the readout chain of the KM3Net telescope is the so-called CLB (*Central Logic Board*). The CLB board was originally designed for the DOM and later adapted for the BM. It integrate the White Rabbit protocol that provide a global time for KM3NeT with 1 ns resolution to synchronize the DOMs

and BMs. The CLB perform the read-out of several instruments, such as the tilt-meter, the compass and the temperature sensor integrated on the same CLB. The main elements on the CLB is a Kintex FPGA that integrate the TDCs and the White rabbit protocol and allows the reconfiguration of the firmware of the CLB.

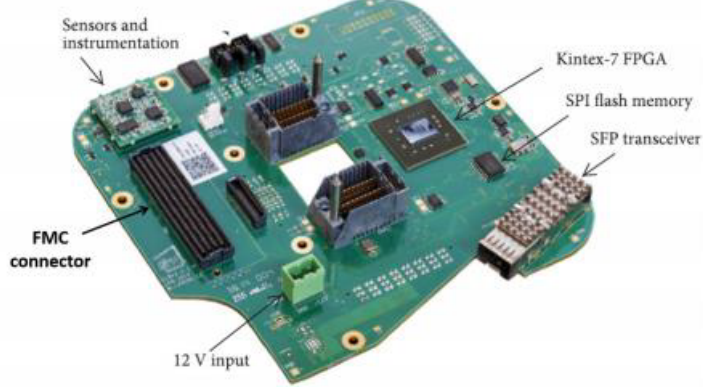


Figure 4.12: A picture of the CLB board. On the picture, we can see clearly the main element of the CLB:Kintex FPGA.

- The FMC board

The *FPGA Mezzanine Card* (FMC) board serves as an interface between the SC of the the BM and the CLB which was originally designed for the DOM and communicates using the I<sup>2</sup>C protocol. It is mounted in mezzanine of the CLB and allows serial communication with RS232 protocol. The FMC is shown on Fig. ???. Moreover, the FMC is also an interface to power and communicate with the hydrophone and the LBL.



Figure 4.13: Real picture of the FMC board. Its mounted in mezzanine of the CLB and the connector are labelled.

- The BCI

The CLB in a DOM is powered by the power board that is not present in a BM. The BCI (*BPS to CLB Interconnection*) board is then an interface between the BPS (Base Power Supply) and the CLB in order to provide the latest with the set of sub-voltages generated in the BPS from its 385VDC input. Fig. ?? shows a photo of the BCI.

All the boards and electrical components inside the base module are floating. The only link to the ground is done through the BPS board. This “sea ref” is an RC bridge with a resistance of 10MΩ and a capacity of 1nF (see Fig. ??). This point is connected to the

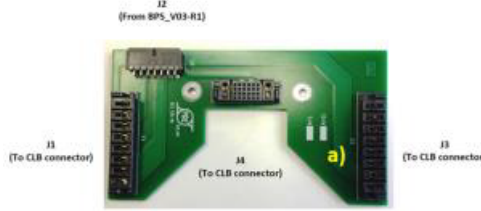


Figure 4.14: Real picture of the BCI board. The connector labels mention their destinations, three of them (J1, J3 and J4) are connected to the CLB and the fourth one (J2) is connected to the BPS to get the power supply needed by the CLB.

internal frame of the base module which is itself connected to the sea through the connector flange.

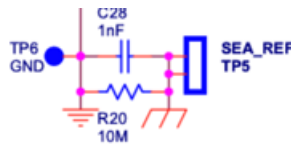


Figure 4.15: The RC bridge used for the grounding of the electronics components of the BM.

#### 4.4.4.3 Power part

One could subdivide this part into two main parts. The first one is the AC/DC converter and the second one is the BPS (*Base Power Supply*) power board.

- The AC/DC converter

The main task of the AC/DC (*Alternative current to direct current*) converter is to convert the 400VAC arriving from the node into 385VDC to provide electric power to the BM and to its DOMs. It is a dedicated that fulfill the KM3NeT requirement. A new version of the converter is installed to the DU starting from the ORCA-DU8, this version includes a tunable start-up delay in order to avoid too big in-rush current at the level of the node(s) while the switch is put ON.

The AC/DC converter communicates with the CLB only in TX mode to provide the following measurements on temperature, input voltage, input current and the output voltage. The component is mounted horizontally to the end flange with a thermal pad in between to ensure thermal dissipation from the item to the seawater.

- The BPS board

The 385 VDC output voltage provided by the AC/DC converter constitutes the input power of the BPS power board. It has to provide the following functions: Switch ON and OFF the 385 VDC power of the DU DOMs, generate all the sub-voltages required inside the BM for the electronic boards (EDFA, CLB) and instruments connected to the BM (hydrophone, LBL) and Communicate with the shore (via the path FMC/CLB) a set of functional parameters.

## 4.5 Integration of Digital Optical Module in Rabat

In addition to the integration of the ORCA BM at Oujda, Rabat, as stated before, participate also to integrate one of the important component of the KM3NeT: the *Digital Optical Module* (DOM). A DOM is a pressure-resistant glass sphere holding 31 Hamamatsu PMTs of 80 mm covering the three dimension axes, it is the main element of the km3net. Fig.?? shows an image of the first DOM integrated at the Rabat site.



Figure 4.16: A picture of a DOM fully integrated in the Rabat site. The penetrator, and the PMTs are clearly seen. Other half-DOM in the integration phase are also visible behind the integrated DOM.

### 4.5.1 Production strategies for the DOMs

A modular production strategy has been adopted in order to produce more than 6000 DOMs. The integration process has been standardized across all integration sites in order to achieve the KM3NeT's baseline production rate.

The KM3NeT collaboration needs a reasonable sized laboratory facility, a dark box (and/or dark room), modest equipment, and a moderate number of human resources to carry out the production of DOMs. Eight optical module production facilities with a total monthly capability of about 100 optical modules are available at the moment, A map of the existing integration sites is displayed in Fig. ??.

The first set of seven DOMs have been successfully integrated at the Rabat DOM integration site, the most recent structure to join the DOM integration group (see Fig. ??).

A second set of 18 DOMs will be delivered and assembled in the last months of 2022, according to the plan.



Figure 4.17: A map showing the integration site of the km3net. At the time being there is eight integration facilities for the DOM: Amsterdam, Erlangen, Starsbourg, Nantes, Napoli, Athens, Catania and Rabat.



Figure 4.18: Picture of the first set of seven DOMs fully integrated in Rabat. They have been placed into the shipping container and are waiting to be sent to the DU integration site.

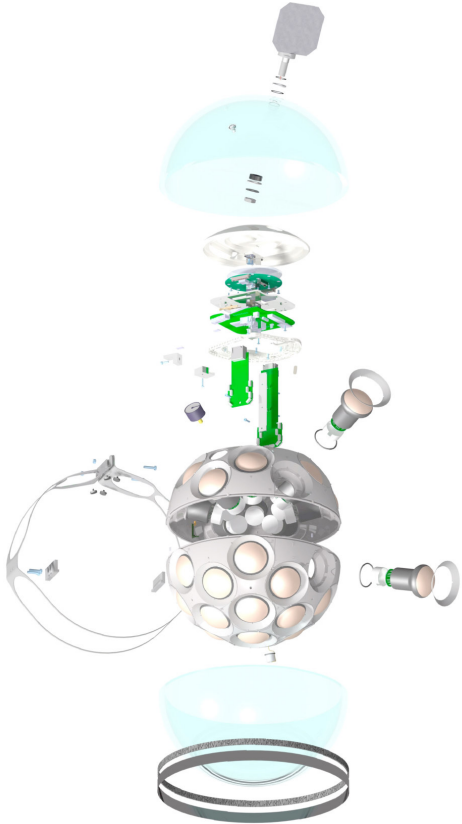


Figure 4.19: The KM3NeT DOM in exploded view, with the a label of each component.

### 4.5.2 DOM Components

The multi-PMT digital optical module was designed as a standard 44 cm diameter pressure-resistant glass sphere with a dense packing of photo-detection sensors, position and timing calibration devices, and associated electronics for electrical power, readout and data acquisition, monitoring, and long-range communication with the onshore control station. The DOM's components were chosen for their ability to operate in low-power environments. As a consequence, DOM's electrical power consumption could be kept to 7 W.

This section is dedicated to describe the DOM's components, an overview can be seen in Fig. ?? and Fig. ???. The majority of parts are already identified in Fig ??.

#### 4.5.2.1 The photomultiplier tube

The photomultiplier tube in use by KM3net DOMs has an 80 mm convex bialkali photocathode and 10-stage dynodes provided by Hamamatsu. In practice, Hamamatsu provided the R12199-02 3 inch, which can be seen in Figure ?? For the next sets, the Hamamatsu R14374 was used, which has much improved performance, particularly when it comes to transit time spread.

Negative high voltage (HV) serves to power the photocathode in PMTs, making control and signal processing smoother. An insulating coating is applied to the outer surfaces of the photomultiplier tubes and to the bases of the PMTs to prevent electrostatic discharge (ESD) between the PMT and its surroundings.

In order to limit the impact of the deterioration and hence extend the lifetime of the PMTs,



Figure 4.20: a picture of a photomultiplier tube and its base made by Hamamatsu, model R12199-02.



Figure 4.21: A view of one of the PMTs boxes that were delivered to the Rabat site. The operator is manipulating the PMTs while wearing anti-ESD gloves.

a relatively low nominal gain of  $3 \times 10^6$  is chosen due to the high counting rate characteristic of the deep-sea condition. By fine-tuning the HV of each PMT in the lab and while the DOM is operational, the functional gain is obtained. As the information on the PMT pulse is reduced to the moment of passing a threshold together with the pulse duration, the tuning is done by taking into account the distribution of pulse-widths of each PMT and setting the average to a value matching to the desired gain (the time-over-threshold technique). The low-power HV bases in the PMTs are developed specially and include integrated amplification and adjustable discriminating.

Two of the first seven integrated DOMs at Rabat used R12199-02 PMTs; the other three used R14374. During DOM integration, a metal reflecting ring is placed around the convex shape of the PMT's sensitive area at the top of the PMTs, creating a 92 percent reflectivity for photons in the 375–500 nm wavelength range. As a result, photon acceptance was improved by 20–40% [96], with the majority of the gain happening in the forward direction. As shown in Fig. ??, 7 boxes of 30 PMTs each and 1 box of 7 PMTs were received in Rabat.

#### 4.5.2.2 Electronics

The DOM houses several electronic boards and sensors that handle data acquisition and monitor the DOM's state during operation. We provide the following electronic components

based on Fig ??:

- The Central Logic Board. it is shown in figure ?? (see also Fig. ?? for reference),
- The long and short octopus boards (they are designated with the number 11 in Fig. ??). All of the PMTs are attached to two boards that are specifically designed for collecting PMT signal data.
- The power Board. Its duty is to provide the electric power required to supply the DOM components (it is illustrated in Fig. ?? and holds the number 7).
- The SFP transceiver (component 15 in Fig. ??).

**4.5.2.2.1 The central logical board** The heart of the DOM electronics is the Central Logic Board (CLB) (shown in Fig. ??), which manages all electronic equipment inside the DOM, analyzes data from PMTs and the acoustic piezo sensor, and keeps communication open with the onshore control station. The CLB also reads a humidity sensor, numerous distributed temperature sensors, and the compass/tiltmeter to keep track of the DOM's operational status. When the optical module is turned on, the CLB's Field Programmable Gate Array (FPGA) is set using an image recorded on the reprogrammable Serial Peripheral Interface (SPI) memory, which holds several images. In the standard arrangement, two images are kept, the first of which is the *golden* image and is loaded at power-up. This image prompts the FPGA to be rebuilt with a *runtime* image that permits full system functionality after running through a series of tests, including communication checks. It also provides a time window for intervention.

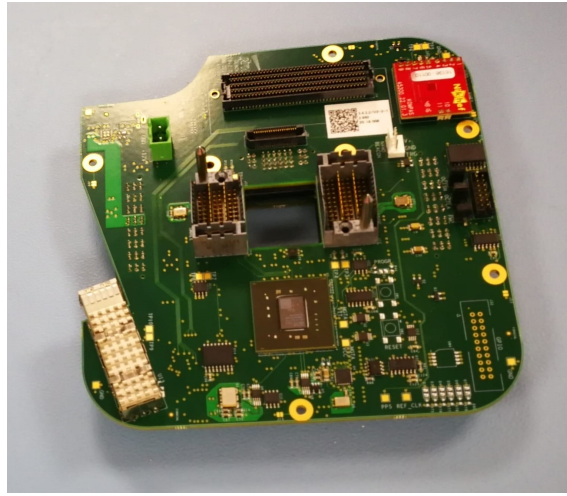


Figure 4.22: A central logic board that was sent to the Rabat site for the integration of the first batch of DOMs is seen in the picture.

**4.5.2.2.2 The octopus boards** The interface between the CLB and the PMT bases is made out of two *octopus* boards, each of which handles the PMTs in a corresponding hemisphere of the DOM. Each PMT base may be addressed individually from the CLB thanks to the I<sup>2</sup>C multiplexer provided by the octopus boards, which also give 3.3 V to the PMT bases.

The piezo sensor's cable which carries the necessary 5V and allows for digital communication between the sensor and the CLB, is also connected to the long octopus board, which serves the bottom half of the DOM, see Fig. ??.



Figure 4.23: At the rabat site, the bottom half of the DOM is being integrated with PMTs connected to the long octopus board.

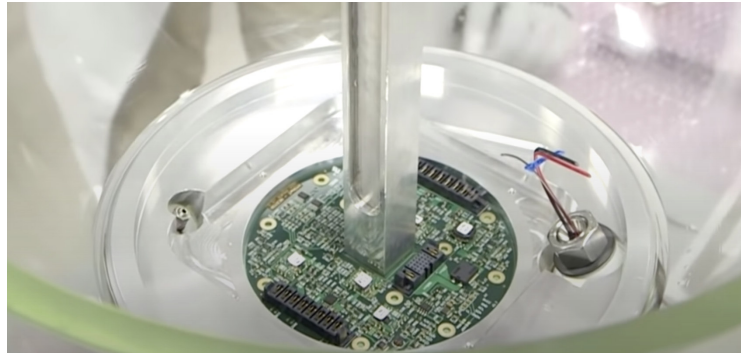


Figure 4.24: A picture of a power board mounted on the top hemisphere of the DOM. The output voltage rails could be seen clearly in black.

**4.5.2.2.3 The power board** To meet the demands of the various components, the power board (see Fig. ??), mounted within the DOM’s top hemisphere, delivers fixed voltage rails of 1, 1.8, 2.5, 3.3, and 5 V, as well as a rail that is tunable up to 30 V through an Analog-to-Digital converter (ADC). The later, monitor the voltage and current of all rails, with output signals transmitted to the CLB.

**4.5.2.2.4 The SFP transceiver** For optical communication and time synchronization, an SFP transceiver (see Fig. ??) is required. It has a high-power duplex single mode laser transceiver with a range of more than 80 kilometers for communicating with the onshore control station over the fiber network. The DOMs are now accessible via a control station broadcast on a shared wavelength.



Figure 4.25: An SFP transceivers received at the Rabat site.

Each DOM has an emitting wavelength chosen with 50 GHz spacing to allow the data stream from the transceiver to be multiplexed onto a lower number of optical fibers. The submarine network is intended to provide a maximum of 72 distinct wavelengths, allowing 4 detecting units each with 18 DOMs to be linked to a single cable. The DOM incorporates an optical add-and-drop filter (Fig. ??), which merges the two communication channels to and from the SFP transceiver into a single fibre.



Figure 4.26: Add-and-Drop filter, combines the signal coming from 2 optical fibers into one.

#### 4.5.2.3 PMT support structure

The PMTs will indeed be mounted using two distinct plastic support structures, each one for each hemisphere. The top support structure houses 12 PMTs, 1 nano beacon (component 12 in Fig. ??), and a pressure gauge to monitor the under-pressure inside the DOM (component 10 in Fig. ??), while the bottom one houses 19 PMTs and has a space for the piezo acoustic sensor (component 14 in Fig. ??).

The structures were built via 3D printing, and the printed support structures had optimizations for printing several components at once in the printers' limited capacity. 3D printing was replaced for the top structure with an injection moulded design made of acrylonitrile butadiene styrene (ABS) for a faster and significantly lower cost of production. In the picture of Fig. ??, a PMTs bottom support structure is shown while being fitted with PMTs and reflector rings.



Figure 4.27: Bottom PMT support structure being integrated with PMTs at Rabat. The operator has already inserted the reflector rings while he wiring the anti-ESD gloves.

#### 4.5.2.4 Glass hemispheres

The DOM elements are enclosed inside a 0.44 m diameter Vitrovex low-activity borosilicate glass sphere (see Fig. ??). The spheres are 14 mm thick and can withstand pressures of

up to  $6.7 \times 10^7$  Pa. The glass of the sphere meets light transmission criteria of more than 95% above 350 nm, which corresponds to the highest sensitivity optical wavelength range of PMTs.



Figure 4.28: Some of the glass hemispheres received in the Rabat site.

The transparent two-component silicone gel utilized provides optical contact between the PMTs and the glass. At the equator, the two hemispheres of the glass sphere are in glass-on-glass contact, relying on atmospheric pressure to keep the seal airtight.

An under-pressure of  $2 \times 10^4$  Pa is applied within the closed DOM, allowing for a perfect seal. This number finds a balance between shipping, storage, and deployment constraints, which need the DOM to remain closed, and the proper operation of all internal components and the gel. To enhance the sealing, a layer of Terostat 81 coated with Scotch encircles the centroid of the DOM (see Fig. ??).

The top glass hemisphere comes with two holes, one of which has a valve via which air will be evacuated in order to apply the under-pressure required to seal the DOM. The other hole is utilized to install the penetrator (Fig. ??), which will allow communication with the DOM through one optical fiber and power supply to the DOM via two copper wires. The penetrator must be impermeable and checked using a helium leak testing machine.

## 4.6 Magnetic monopoles reconstruction with ORCA

Although, the nuclearites analysis has been established and good results are reported, there is still a considerable amount of experimental data that would be explored. At the time being, ANTARES is fully dismantled and its successor, KM3NeT, continues to grow and every time a new line(s) is deployed. The new detector is bigger, more sensitive and more accurate. Following the foreword steps to build the biggest underwater neutrino detector in the abbeys, we investigate the possible signature of magnetic monopoles in the KM3NeT-ORCA detector.

At the time of typesetting this section, the ORCA detector runs with 11 detection units. However, the full ORCA configuration was used in order to simulate MMs. In this section, we present our investigation of reconstructing the simulated MMs using a modified ANTARES algorithm. Although this effort is still in progress, we outline the reconstruc-

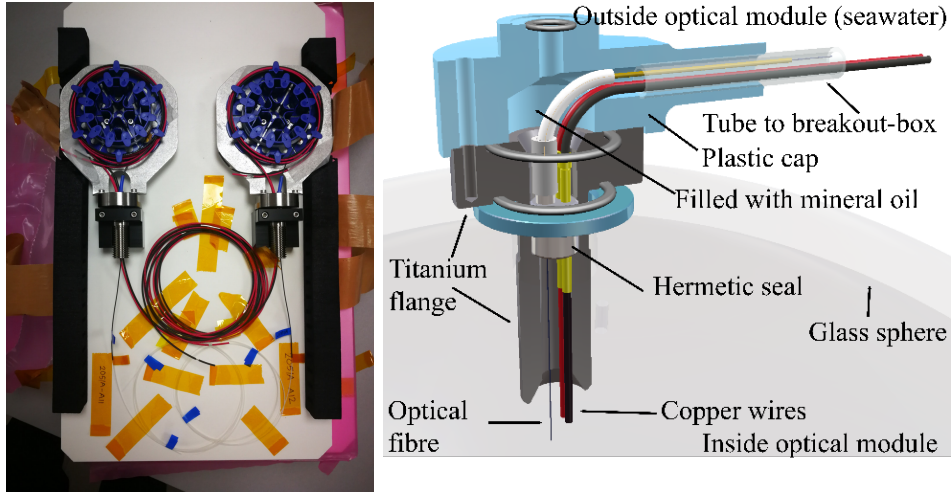


Figure 4.29: Left: 2 of the 7 penetrators received in the Rabat site. Right: Open schematic of a KM3NeT penetrator.

tion process and give some preliminary results. Finally, we will discuss the results that have been revealed.

#### 4.6.1 Simulation chain of MMs in ORCA

MMS have been simulated using a Monte Carlo program based on GEANT3. The simulation is independent of the MM mass and the incoming direction of MMs was distributed isotropically over the lower hemisphere and on the so-called *can*<sup>1</sup>. The propagation and detection of emitted photons is processed inside a virtual cylindrical surface surrounding the instrumented volume around the detector. A radius of 480 m is chosen to take into account the large amount of light emitted by MMs.

Practically, MMs simulation is done in two steps. The first step is to generate MMs with random zenith and azimuth angles bellow the detector, this step is performed by the so-called *genmon* code. Genmon is a program based on *genneu v5r1* (a generation program). It generates monopole tracks to form on the CAN surface. In the code's data card, the parameter CUT is used to specify the monopole velocity interval. Because the light production is so dependent on velocity, different *can* sizes can be used at different speeds. In genmon, a monopole is defined as a particle having a mass of 10 GeV and particle ID 39<sup>2</sup>. The velocity is then connected to the energy by

$$E = \frac{10\text{GeV}}{\sqrt{1 - \beta^2}} \quad (4.4)$$

The second step is to propagate the MMs inside the *can* and perform the light generation and the particle tracking. This step is done using the geamon software. geamon is based

<sup>1</sup>*can* is an abstract geometrical shape that is used to generate particles before they are propagated into the detector sensitive volume. In the case of MMs in ORCA, a cylindrical shape is adopted as a can around the detector active volume.

<sup>2</sup>Actually, a particle id of 666 is utilized in ANTARES since it is not occupied by any particle in geant3. Because it is not identified in the ORCA simulation software, this id produces events with no hit.

on geasim. It uses the files already produced by genmon as input, and produces event files containing the hits caused by the MM on the DOMs.

As previously stated, our goal is to adapt an ANTARES reconstruction method to the KM3NeT ORCA detector. As a result, we begin our investigation with a single MMs velocity interval of  $0.6835 < \beta_{mon} < 0.728$  using logarithmic interpolation to estimate the Cherenkov emission. The interval chosen is not constrained; it is selected randomly. After the code yields satisfactory results, we can proceed to the other intervals.

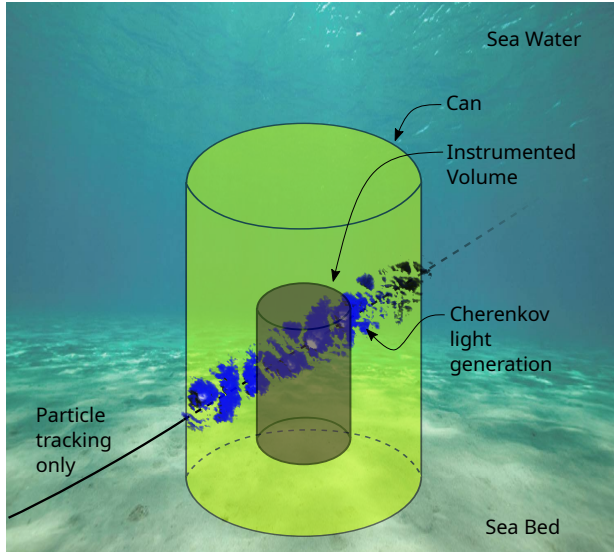


Figure 4.30: A schematic illustration of the simulation of MMs in the km3net-ORCA detector. Because only ascending MMs are simulated, they are generated isotropically on the lower hemisphere with the genmon generator. The geamon code is used to generate and track the light within the can, as seen in blue in the picture.

The simulation chain is composed of several steps. Once the MMs have been generated with genmon. Each produced event involves an MM with a well-defined position ( $x, y, z$ ) and two angles ( $\theta, \phi$ ) indicating the particle direction, as well as other parameters such as particle id and energy. If the particle crosses through the *can*, a light generation and tracking is executed in geamon. Finally, we obtained an event file with all of the hit information about every event.

The next step is to mimic the detector's response to these events. This is accomplished using the collaboration tool called *JTriggerEfficiency* (JTE), which is included in a package named *JPP*. This code simulates the detector response while accounting for the true data collecting circumstances. Finally, we have a JTE file that contains data in the usual km3net format. At this point, the simulation is completed, and we may begin evaluating the simulation parameters at the Trigger level or reconstruct the simulated events to conduct a more accurate analysis with more robust parameters.

#### 4.6.2 Results on the MMs simulation

The simulation of magnetic monopoles in the full KM3NeT ORCA detector was performed, and the results on the hit times and amplitudes of the detected photons were obtained. The presentation of these results can provide valuable insights into the behavior and properties of magnetic monopoles and can help to guide us to set constraints on the reconstruction

parameters. By simulating the behavior of MMs in the KM3NeT ORCA 115 lines detector, we will be able to predict the expected patterns of hit times and amplitudes that would be produced by these particles.

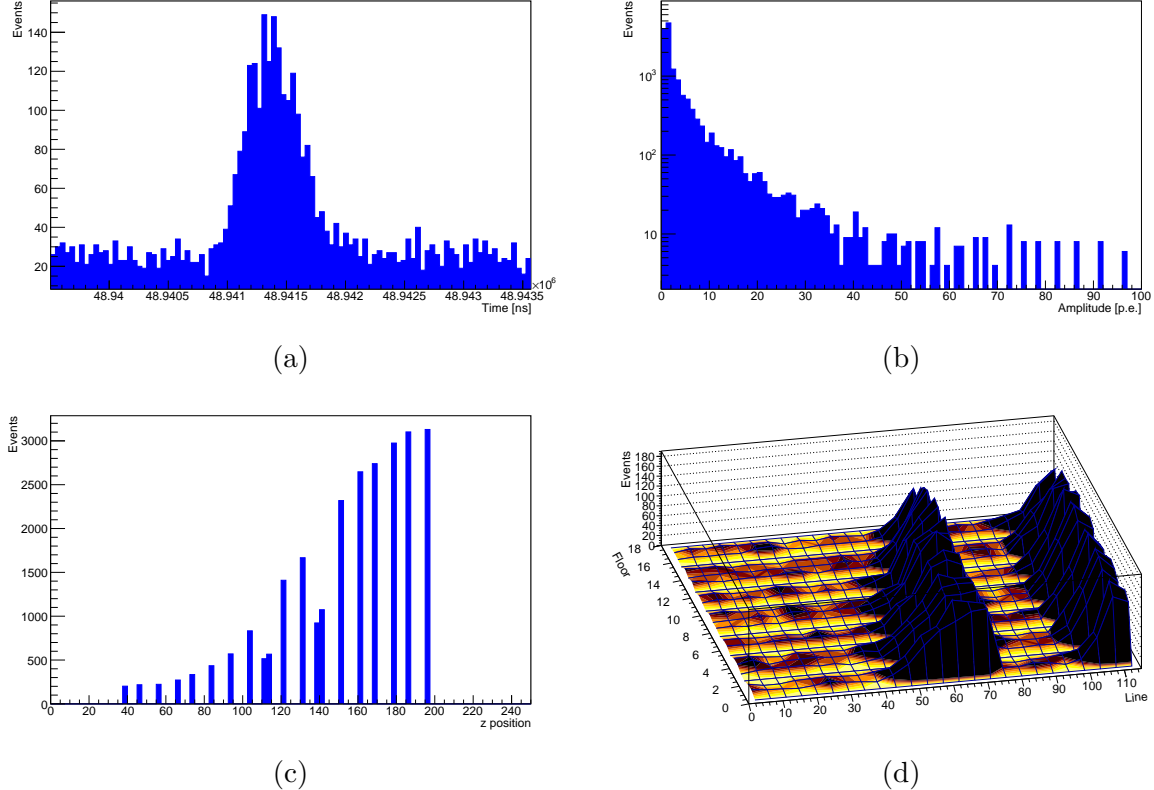


Figure 4.31: Analysis of magnetic monopoles hits within the KM3NeT detector. ?? Distribution of time recorded by the detector for all hits within a particular event, showing high resolution. ?? Amplitude of hits within the same event, showing promising behavior. ?? z position of hits, indicating that the majority of hits come from above the detector. ?? 3D plot of hits within the event, showing two major traces around lines 60 and 110. These results provide valuable guide the development of more advanced reconstruction algorithms

Based on the results of our simulation, the distribution of the time recorded by the detector for all the hits of a particular event of magnetic monopoles within KM3NeT appears to be highly resolved (see Fig. ??), with differences between the first and last hit within an event being on the order of nanoseconds. This high resolution may have implications for our ability to perform selection procedures on the hits in our reconstruction program. It is important to note that this high resolution may be due to the intrinsic properties of the detector or the high speed at which the MMs are crossing the detector. Further investigation is required to determine which of these factors is contributing to the observed behavior.

In addition to the time distribution, we also analyzed the amplitude and z position of the hits as shown in ???. The plot on the amplitude (Fig. ???) of hits looks promising, while the plot on the z position of the hits suggests that the majority of the hits are coming from above the detector, with high numbers of hits located at large z values. Finally, we generated a 3D plot showing the number of hits recorded for a given event in each line and each floor of the detector (see Fig. ??). The topology of the hits in this plot indicates two

major traces for the event around lines 60 and 110. This information can be used to guide further analysis of the event and improve our understanding of the properties of magnetic monopoles within the KM3NeT detector.

In general, the reconstruction of MMs within KM3NeT involves the identification and analysis of the hits produced by MMs as they pass through the detector. The goal is to reconstruct the trajectory and properties of the MMs based on these hits. This can be a complex task, as the detector produces a large number of hits from various sources, and the properties of MMs themselves are not well known.

### 4.6.3 Reconstruction of MMs

The BBDisp software is an ANTARES package used to reconstruct monopoles within the ANTARES neutrinos telescope. The package consists of a collection of C++ files that allow users to select events in the *PhysicsEvent* data format. Each event occurs as a collection of hits carrying the timing, amplitude, and location information of the PMT which caused it. While photons from the physical event are lighting the detector optical modules (OMs), other processes occurring in the abbeys surrounding the detector, such as bioluminescent and  $^{40}\text{K}$  decay events, are also yielding hits. The package includes code that filters hits and selects only consistent hits to improve reconstruction quality.

We intend to adapt the BBDisp package to the KM3NeT in the following sections. The effort consists of changing the data structures from ANTARES to KM3NeT and optimizing hit selection and merging to fit the geometrical requirements of the KM3NeT. We provide the approach for reconstructing MMs in the KM3NeT-ORCA detector. As previously indicated, we employ the entire ORCA setup of 115 detector units. We describe the hit selection method as well as the hit merging modalities. The track and bright point reconstruction procedures will also be highlighted.

The majority of the parameters and equations used for MMs reconstruction within ORCA detector are similar to those reported in [97]. However, the detector geometry change slightly in terms of DOMs and line spacing; this should be considered while specifying the parameters in the new code. In the following, we will refer to this new code as JBB-Monopole code.

#### 4.6.3.1 Geometrical considerations

JBBMonopole, as for ANTARES, uses geometrical approximations in order to provide considerably consistent results within a relatively short time. We adopt the same consideration listed below:

- Vertical line: Detector lines are facing displacement and consequently the DOM's positioning in relation to the sea current. They are assumed to be perfectly vertical, and any aberrations are omitted.
- DOM geometry: The actual geometry of the DOM is overlooked. Each DOM is considered to be a single PMT with an axis-symmetrical field of view that is positioned exactly on the detector line. PMT signals inside a specific DOM are combined.

These assumptions are employed in the phases of hit merging, hit selection, and fitting. A detector line is a straight line in space according to the aforementioned considerations. It is also assumed that a muon track is a straight path, therefore multiple scattering and

other effects are neglected. Except in the case of a completely vertical track, the point of closest approach of the muon track to the detector line could well be calculated. The bulk of the Cherenkov light is estimated to be visible near this point.

#### 4.6.3.2 Hit selection

Prior to beginning the practical hit selection, time and charge calibrations are used to convert raw data to physical quantities such as time (in nanoseconds) and charge (in photo-electrons). The standard data processing in ANTARES has been detailed up to this point, hence we use the same nomenclatures here.

Each DOM's calibrated hits are time-ordered. All hits on the same DOM during a pre-determined period are combined. Merging is achieved by adding the hit charges while preserving the timing of the first hit. The merging time window must be adjusted to be short enough to allow for clean hit selection, with the earliest merged hits having a high chance of coming from a particle track. The combining time window, on the other hand, must be long enough to filter out the majority of the signal hits. A merging window of 1.6 ns is appropriate in the case of ORCA DOMs. As a consequence, a list of combined hits per floors is produced, which serves as the base for all subsequent steps.

The purpose of hit selection is to identify hits owing to Cherenkov photons while eliminating random optical background hits or dispersed late hits. Late scattering hits are infrequent when compared to the standard optical background of 60-100 kHz. A Cherenkov photon at  $k = 470$  nm has a low probability of being scattered by light along a trajectory of 60 m.

The majority of the Cherenkov light is predicted near the point of closest approach of the track to the detector line for tracks that are not parallel to a detector line (see Fig. ??). As a result, the initial step in hit selection is to identify a *hotspot* of light on a detector line caused by Cherenkov light produced by a passing particle. A single high charge hit does not make a clear hotspot in the presence of background light; two high charge hits in adjacent or next-to-adjacent floors are recommended. The detector DOMs are sequentially numbered along the z-axis, similar to floors in a building. The adjacent or next-to-next floor for a given floor  $i$  are at floor  $i \pm j$ , where  $j = 1, 2$ . The following constraint on the absolute hit time difference  $\Delta t$  is applied to confirm that hits on floors  $i$  and  $j = 1, 2$  were caused by the same particle.

$$\Delta t < j \Delta z \frac{n}{c} + t_s, \quad (4.5)$$

with  $\Delta z$  being the absolute vertical distance between neighboring floors,  $c$  being the speed of light in vacuum,  $n$  being the refractive index of the medium, and  $t_s$  being an additional time delay that accounts for the timing uncertainty of the photon detection itself as well as the detector geometry approximations. floors are supposed to be equally spaced.  $\Delta t = 30$  ns for nearby DOMs and  $\Delta t = 60$  ns for next-to-next floors for the ORCA detector with  $\Delta z = 9$  m and  $t_s = 6$  ns. Because merged hits from separate PMTs or with a charge greater than 2.5 photo-electrons are more likely to be produced by a particle track, they are only considered here. All hits that contribute to the aforementioned hotspot of light are collected as approved hits for the following phases. If multiple hotspot appear in the same floor at different times, only the first of them is stored.

Only detector lines with at least one hotspot are considered in the next steps. This condition eliminates the sample's individual hits. Hits are added to the list of selected hits using the "hot spot" hits as identifiers. From now on, hit selection is entirely reliant on time information. At this time, there is no charge cut. This enables the use of the attenuated signal at longer distances from the point of closest approach, as shown in Fig. ???. New hits on a particular detector line are searched recursively within a short period of time surrounding the times of previously chosen hits. The estimated hit timings in adjacent or next-to-adjacent floors are computed under the assumption that hits occur linearly in the  $z - t$  plane. In the following method, the predicted arrival time  $t_{i\pm j}$  at floor  $i \pm j$ , ( $j = 1, 2$ ) is connected to any pair of the three hit times  $t_i$ ,  $t_{i\mp 1}$ ,  $t_{i\mp 2}$  at floors  $i$ ,  $i \mp 1$ ,  $i \mp 2$ .

$$t_{i\pm j} = t_i + j(t_i - t_{i\mp 1}), \quad (4.6)$$

$$t_{i\pm j} = t_i + j(t_i - t_{i\mp 2})/2, \quad (4.7)$$

$$t_{i\pm j} = t_{i\mp 1} + (j+1)(t_{i\mp 1} - t_{i\mp 2}). \quad (4.8)$$

In the next steps, time windows  $[t_{i\pm j}^{early}, t_{i\pm j}^{late}]$  based on the above equations are defined, which are used for the hit selection. Only one of the extrapolations above may be done if only two of the three hits in floors  $i, i \mp 1, i \mp 2$  occur. A new floor  $i \pm j$  hit is considered if it happened within a time window of

$$t_{i\pm j}^{early} = t_{i\pm j} - jt_s, \quad (4.9)$$

$$t_{i\pm j}^{late} = \max(t_i + j\Delta z \frac{n}{c} + t_s, t_{i\pm j} + jt_s). \quad (4.10)$$

If all three hits are found, the minimum and maximum  $t_{i\pm j}$  are calculated, Then a time window of

$$t_{i\pm j}^{early} = t_{i\pm j}^{min} - jt_s, \quad (4.11)$$

$$t_{i\pm j}^{late} = t_{i\pm j}^{max} + jt_s. \quad (4.12)$$

is applied for the floor  $i \pm j$ . If multiple hits in floor  $i \pm j$  match the requirements, only the first one is picked. This operation is repeated indefinitely. If no new hits are detected on either floor  $i \pm 1$  or floor  $i \pm 2$ , the operation ends, avoiding gaps of more than one floor. The appearance of many well-separated hotspots of light across the same detector line acts as independent seeds to relaunch the operation. The hit selection indicated above is only done once, it permit only one hit for each floor.

#### 4.6.3.3 MMs Track reconstruction

The list of selected hits is verified before performing any fit. Only events with at least five hits are qualified. If all of the chosen hits are on a single detector line, a single-line fit strategy is launched; otherwise, a multi-line fit procedure is conducted.

In our approach, a particle path is defined as a straight line in space. The particle is supposed to travel at the speed of light in vacuum. All space-time points,  $\vec{p}(t)$ , that are part of the track can be represented as

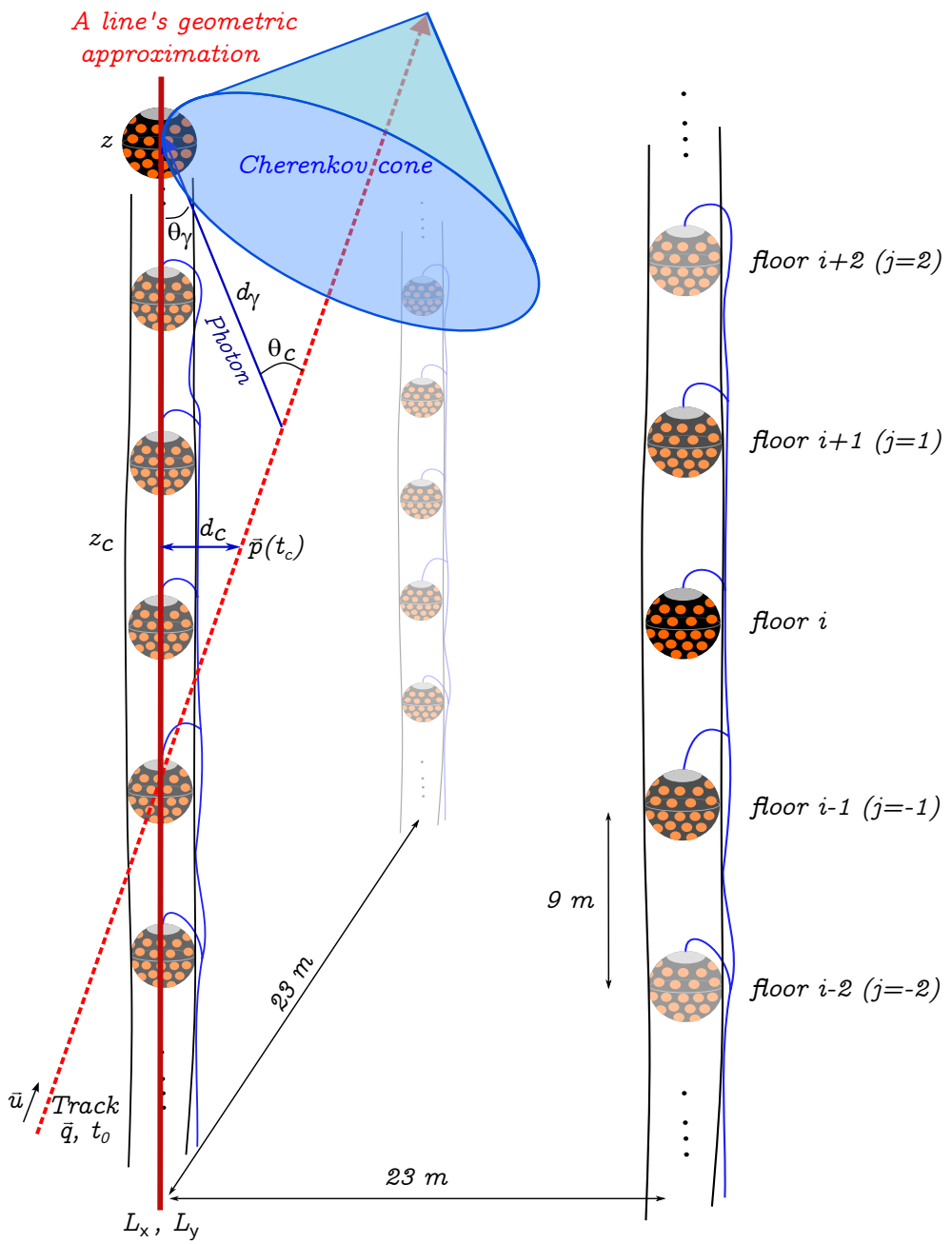


Figure 4.32: Under the geometrical approximation, the variables used to characterize a track and its related Cherenkov cone with respect to a vertical detector line are depicted. The image also illustrates the considered lines and DOMs spacing, as well as the floor indexing implemented in the code.

$$\vec{p}(t) = \vec{q} + c(t - t_0)\vec{u}. \quad (4.13)$$

The particle goes in the direction  $\vec{u}$  after passing through the point  $\vec{q}$  at time  $t_0$  (i.e.  $\vec{q} = \vec{p}(t_0)$ ) see Fig. ???. By redefining  $t_0$ , the vector  $\vec{q}$  may be shifted along the track. As a result, the track is defined by five variables in total: three values to fix  $\vec{q}$  for a particular time and two angles ( $\theta$  and  $\phi$ ) to characterize  $\vec{u}$ . As previously stated, the geometric approximations of the detector lines leads in vertical lines along the z-axis at well defined positions in the x-y plan with the coordinates  $L_x$  and  $L_y$ . The point of closest approach of the particle track to a detector line is defined by the z-component as:

$$z_c = \frac{q_z - u_z(\vec{q} \cdot \vec{u}) + u_z(L_x u_x + L_y u_y)}{1 - u_z^2}, \quad (4.14)$$

the particle passes through this point at the time:

$$t_c = t_0 + \frac{1}{c}(L_x u_x + L_y u_y + z_c u_z + \vec{q} \cdot \vec{u}), \quad (4.15)$$

far from the considered line detector by a distance of:

$$d_c = \sqrt{(p_x(t_c) - L_x)^2 + (p_y(t_c) - L_y)^2}. \quad (4.16)$$

Fig. ?? depicts the parameters mentioned previously. If the track is fully vertical and hence parallel to the detector line, the values  $t_c = t_0$  and  $z_c = q_z$  are chosen. The track may be easily reparametrized in terms of  $z_c$ ,  $t_c$ , and  $d_c$  for each detector line, as well as the two angles that determine  $\vec{u}$ . For a single-line fit, lined the detector line at the coordinate origin  $(L_x, L_y) = (0, 0)$  and use Eqs. ??, ?? and ?? reduced to

$$z_c = \frac{q_z - u_z(\vec{q} \cdot \vec{u})}{1 - u_z^2}, \quad (4.17)$$

$$t_c = t_0 + \frac{q_z u_z - (\vec{q} \cdot \vec{u})}{c(1 - u_z^2)}, \quad (4.18)$$

$$d_c = \sqrt{p_x^2(t_c) + p_y^2(t_c)}. \quad (4.19)$$

A single detector line is invariant when the coordinate system is rotated around the z-axis. This signifies that the track is not fully determined, and only four parameters may be determined:  $z_c$ ,  $t_c$ ,  $d_c$ , and  $u_z$ . There is no dependency on azimuth.

To apply the track fit, the following quantities must be known:

1. the arrival time  $t_c$  of a Cherenkov photon at the detector line coordinates  $(L_x, L_y, z)$ .
2. its associated travel path  $d_\gamma$ .

3. its inclination with respect to the detector line,  $\cos\theta_c$ .

All three values may be obtained using the aforementioned parameters and the refractive index  $n$ , which is associated to the Cherenkov angle  $\theta_c$  by  $1/n = \cos\theta_c$ :

$$t_\gamma(z) = (t_c - t_0) - \frac{1}{c} \left( (z - z_c) u_z + \frac{n^2 - 1}{n} d_\gamma(z) \right), \quad (4.20)$$

$$d_\gamma(z) = \frac{n}{\sqrt{n^2 - 1}} \sqrt{d_c^2 + (z - z_c)^2(1 - u_z^2)}, \quad (4.21)$$

$$\cos\theta_\gamma(z) = (1 - u_z^2) \frac{z - z_c}{d_\gamma(z)} + \frac{u_z}{n}. \quad (4.22)$$

These equations are accurate for Cherenkov photons of a particular wavelength. Dispersion and group velocity effects, as well as delays caused by light scattering, are neglected. Depending on the medium in which the detector is placed, a suitable effective refractive index is applied.

In addition, the software can fit point-like source events in the detector. The paper [97] contains a complete explanation of the methods implemented in the code.

#### 4.6.4 Preliminary results on track reconstruction

We successfully generated, propagated, and simulated the response of the KM3NeT detector to MMs. For our initial analysis, we focused on simulating MMs within the range of  $\beta = [0.8615, 0.906]$ . A sample of 100 arbitrary runs was processed and analyzed. In Fig. ??, we present the number of photoelectrons recorded by each optical module for the selected hits in each event (refer to Fig. ??).

The reconstruction program provided a set of variables characterizing each MM reconstructed event. One of these variables is  $nhit$ , which represents the number of hits used in the track reconstruction of the events. ?? illustrates the distribution of the  $nhit$  variable. Additionally, it depicts the  $nline$  variable, which corresponds to the number of detector lines used to reconstruct the event.

Fig. ?? depicts the angular resolution, represented by the difference between the true zenith angle of an event obtained from Monte Carlo simulations and the reconstructed value. It is evident that a significant difference exists between these two values, with nearly 50% of the events exhibiting a discrepancy of more than 20%. Similar behavior is observed with the azimuth angle. These results indicate an issue in the reconstruction process, highlighting the need for further investigation to improve the reconstruction of MMs using the ORCA detector.

We conducted The research for magnetic monopoles in the KM3NeT detector using simulation, and subsequently performed a reconstruction analysis based on the simulation results. Initial findings indicate that the quality of the reconstruction is not satisfactory. One possible explanation for this is that the temporal spacing between hits is too small in comparison to the selection condition, such that the time between the first and last hit in an event is less than the coincidence time within the same DOM. As a consequence, the entire set of event hits are considered as coincident, resulting in a suboptimal reconstruction. Our ongoing investigation aims to identify the main cause of this problem, in order

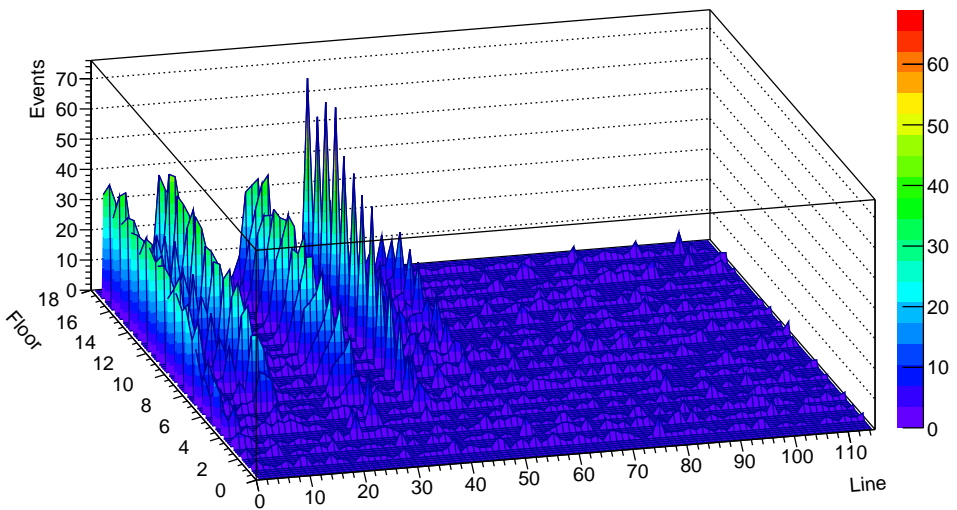


Figure 4.33: Number of selected photoelectrons for each floor. This plot correspond to triggered hits of one event of MMs simulated in ORCA.

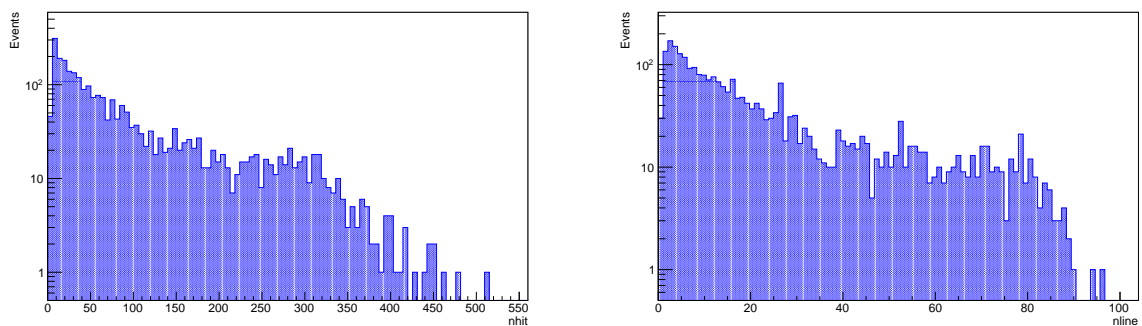


Figure 4.34: Number of selected hits (left) and number of lines used to reconstruct MMs events (right).

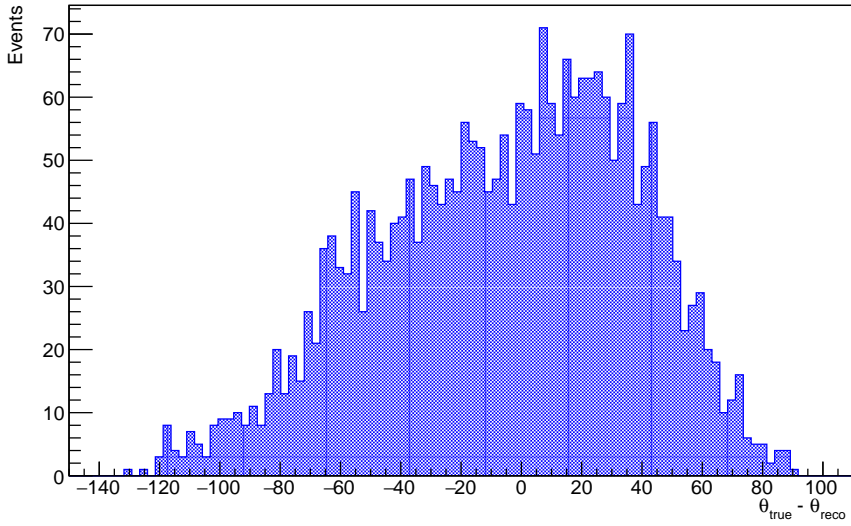


Figure 4.35: Number of selected photoelectrons for each floor. This plot correspond to triggered hits of one event of MMs simulated in ORCA.

to refine our reconstruction methodology and improve the quality of our results. Furthermore, we should note that the temporal spacing between hits is constrained by the time resolution of the photomultipliers, which limits our ability to distinguish between closely spaced events. This poses a significant challenge to the accurate reconstruction of events, and underscores the need for continued research and development in this area.

It should also be noted that the temporal spacing between hits that was observed in our analysis is more rapid than what would typically be expected for a magnetic monopole event, which is expected to traverse the detector over a longer period of time. This discrepancy further supports our hypothesis that the observed poor reconstruction quality may be attributed to the time coincidence condition in the DOMs, and highlights the importance of further investigation into this concern.

## 4.7 Conclusion

In conclusion, the construction of the KM3NeT neutrino telescope represents a significant achievement in the field of astrophysics and particle physics. The telescope is designed to detect neutrinos, which are subatomic particles that are difficult to observe due to their weak interaction with matter. By detecting these elusive particles, the KM3NeT telescope will help scientists study the most violent and energetic phenomena in the universe, such as supernovae, gamma-ray bursts, and black holes. The construction of the KM3NeT telescope involved a large international collaboration of scientists and engineers, who worked together to design and build the complex infrastructure necessary to house the telescope's thousands of optical modules. With its unique capabilities, the KM3NeT telescope is expected to make significant contributions to our understanding of the cosmos and the fundamental properties of matter. The KM3NeT telescope would provide an interesting infrastructure with a resolution that has never been achieved with its two detectors (ARCA and ORCA). The size of the detectors on both devices, ARCA with 21 active lines and ORCA with 15 lines, keeps expanding while they are still being constructed. Numerous

analysis are now being conducted using the information collected by the neutrino telescope’s partial configuration, including the measurement of atmospheric muon flux, the real-time core-collapse supernova neutrino search, and neutrino mass ordering [98–100].

The participation of Oujda and Rabat in the construction of the KM3NeT neutrino telescope is a significant achievement for Morocco and represents a major contribution to the international scientific community. This requires a high level of expertise in the fields of physics, engineering, and technology, and the participation of these cities demonstrates the growing scientific capabilities of Morocco. By participating in the construction of the KM3NeT telescope, Oujda and Rabat have joined a large international collaboration of scientists and engineers who are working together to advance our understanding of the Universe and the fundamental properties of matter. This collaboration not only contributes to the advancement of science, but it also provides opportunities for knowledge sharing and capacity building, which can have important long-term benefits for the development of the country. Overall, the participation of Oujda and Rabat in the construction of the KM3NeT telescope is a significant milestone in the history of science in Morocco and a testament to the country’s commitment to scientific progress.

The modification of the code dedicated to reconstruct magnetic monopoles in ANTARES for use in KM3NeT would constitute a significant achievement toward analyzing this particle in more accurate detector. Magnetic monopoles are hypothetical particles that have been predicted by theory, but have yet to be observed in experiments. By modifying the code to reconstruct the trace of these particles in KM3NeT, we have taken an important step towards potentially searching magnetic monopoles in the future. The development of this new code required a significant amount of investigations and testing, as the KM3NeT telescope differs from ANTARES in several key ways. However, we were able to successfully adapt the code to the new instrument and present some initial results. Further investigation and refinement of the code will be necessary to fully realize the potential of the KM3NeT telescope for the detection of magnetic monopoles, and this work represents an exciting area for future research in particle physics.

# Conclusion

In recent decades, neutrino physics has significantly enriched our understanding of particle physics. These developments are primarily important for a more accurate description of neutrino characteristics, and it is likely that they have significant repercussions for the entire understanding of basic interactions and their relations to astrophysics and cosmology. Given that neutrino masses necessitate physics that apparently went beyond the limits of the model, the neutrino's central role becomes even unambiguous. But right now, we lack a comprehensive understanding of this new physics and its energy scale. The scientific missions of the ANTARES (and its successor KM3NeT) instruments cover a wide range of activities like looking for cosmic ray sources, studying galactic supernova explosions, searching for dark matter, and studying neutrinos in and of themselves. The goal of multiple generations of high-energy gamma-ray and neutrino telescopes has been to locate the accelerators that generate the Galactic and extragalactic cosmic rays, but so far, little progress has been made. With the full implementation of KM3NeT and IceCube, the first neutrino detectors with sensitivity to the predicted fluxes, detection of the gamma-ray and neutrino fluxes associated with cosmic rays approaches a new milestone. By utilizing the Cherenkov light that is released along the path of the charged particles produced in interactions that take place near to the detector volume, neutrino telescopes are conceived to search for neutrino generators in the Cosmos. They provide great tools for searching for exotic and rare particles in cosmic rays because to their enormous size and the protection provided by substantial water or ice overburden. They are particularly responsive to particles that the Standard Model doesn't really forecast and which could be carriers of novel physics.

We reported in this dissertation our results obtained for searching for nuclearites of strange matter with nine years of experimental data gathered by the ANTARES neutrinos telescope. We considered four nuclearites masses  $4 \times 10^{13}$ ,  $10^{14}$ ,  $10^{15}$  and  $10^{16}$  GeV/c<sup>2</sup> assuming a velocity of  $10^{-3}$  at the top of atmosphere. Characterization of nuclearites signal and the simulation chain are addressed in chapter ???. The results reported are at the level of  $\sim 5 \times 10^{-17}$  cm<sup>-2</sup> s<sup>-1</sup> sr<sup>-1</sup> for the higher mass showing an improvement of more than one order of magnitude with respect to the previous reported limits with other experiments. What makes this analysis unique is that it is conducted using a neutrino telescope specifically designed for tracking relativistic particles where the triggering system are based on that fact. In the absence of dedicated triggers for slow moving particles inside ANTARES we investigated the response of the standard muons triggers labeled T3 and 3D. Due to the slow motion of nuclearites events inside the apparatus, both triggers captured a series of snapshot for the same event allowing for nuclearites analysis within the apparatus. The study of exotic particles with different detectors, including the ANTARES telescope, is an active and exciting area of research that has the potential to shed light on some of the most pressing questions in astrophysics, including the nature of dark matter and the

origins of cosmic rays. By continuing to develop and refine advanced detectors and techniques, researchers can make significant progress in our understanding of the Universe and its fundamental properties.

In the end, the research of exotic particles with different detectors, including nuclearites with ANTARES, represents a promising and important area of research that can yield valuable insights into the nature of our Universe. The continued study of these particles using advanced detectors and techniques is crucial to advancing our understanding of the Cosmos.

# Appendix A

## Feldma-Cousin approach

Feldman and Cousins Confidence Intervals, also known as the Feldman-Cousins method, is a statistical technique used in particle physics to construct confidence intervals for parameters of interest. This method addresses the issue of biased intervals that can occur when using traditional frequentist methods in the presence of small or zero event rates. The Feldman-Cousins method is based on the concept of *likelihood ratio ordering*, which involves comparing the likelihood of different parameter values given the observed data.

In particle physics, we often need to set limits on the flux of some rare process, such as the production of a new particle. The Feldman-Cousins approach is a statistical method for calculating confidence intervals on the expected number of events from such a process.

Let's assume we have some experimental data in the form of a histogram of the number of events in a certain energy range, and we want to set a limit on the expected number of events from a particular process in that range. We can write the expected number of events as

$$N_{\text{exp}} = \Phi \cdot \epsilon \cdot A \cdot t \cdot \Delta E,$$

where  $\Phi$  is the flux of the process,  $\epsilon$  is the detector efficiency,  $A$  is the detector effective area,  $t$  is the livetime of the experiment, and  $\Delta E$  is the energy range of interest. We want to calculate a 90% confidence level (CL) upper limit on  $\Phi$ , which we'll call  $\Phi_{\text{UL}}$ .

The Feldman-Cousins approach involves constructing a test statistic  $q$ , which measures the deviation of the observed data from the expected background. A common choice for  $q$  is

$$q = -2 \ln \frac{\mathcal{L}(N_{\text{obs}}|N_{\text{exp}} + B)}{\mathcal{L}(N_{\text{obs}}|N_{\text{obs}} + B)},$$

where  $N_{\text{obs}}$  is the observed number of events in the energy range,  $B$  is the expected number of background events (which we assume is known), and  $\mathcal{L}$  is the likelihood function. The denominator in this expression is the likelihood of the observed data given that the expected signal plus background is the true underlying model, while the numerator is the likelihood of the data given that the observed events are the true underlying model.

We then define two hypotheses: the null hypothesis,  $H_0$ , which corresponds to the case where there is no signal and  $N_{\text{sig}} = 0$ , and the alternate hypothesis,  $H_1$ , which corresponds

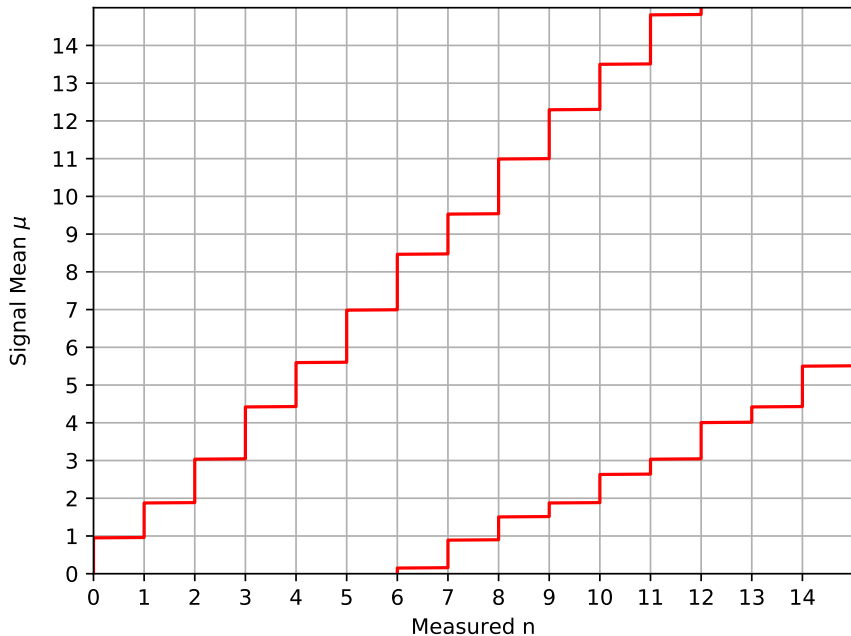


Figure A.1: Confidence belt for 90% C.L. central confidence intervals, for unknown Poisson signal mean  $\mu$  in the presence of a Poisson background with known mean  $b = 3$ .

to the case where there is a signal and  $N_{\text{sig}} > 0$ . We calculate the distribution of  $q$  under each hypothesis using Monte Carlo simulations, and use these distributions to construct a confidence belt in the  $N_{\text{sig}} - q$  plane. The plot in Fig. ?? shows the confidence belt based on the Feldman and Cousins principle for a 90% confidence level for the unknown Poisson signal mean  $\mu$ . It is a reproduction of Fig. 7 from [85].

Now, we assume that have an experiment where the observable  $x$  is simply the measured value of  $\mu$  in an experiment with a Gaussian resolution with known width sigma. The plot in Fig. ?? shows the confidence belt based on the Feldman and Cousins principle for a 90% confidence level for the mean of the Gaussian  $\mu$ , constrained to be non-negative

Suppose we have a background-only hypothesis for a particular search in IceCube [101], and we observe 10 events in our data set. We want to set a 90% confidence level upper limit on the number of signal events that could be present in the data. We know that the expected background in our signal region is 8.3 events, with a Poisson uncertainty of  $\sqrt{8.3} \approx 2.9$  events.

Using the Feldman-Cousins approach, we can calculate the probability of observing  $n$  events, given that the true signal is  $s$  and the true background is  $b$ . This is given by the Poisson probability mass function:

$$P(n|s, b) = \frac{(s+b)^n}{n!} e^{-(s+b)}$$

We can then define the likelihood ratio function as:

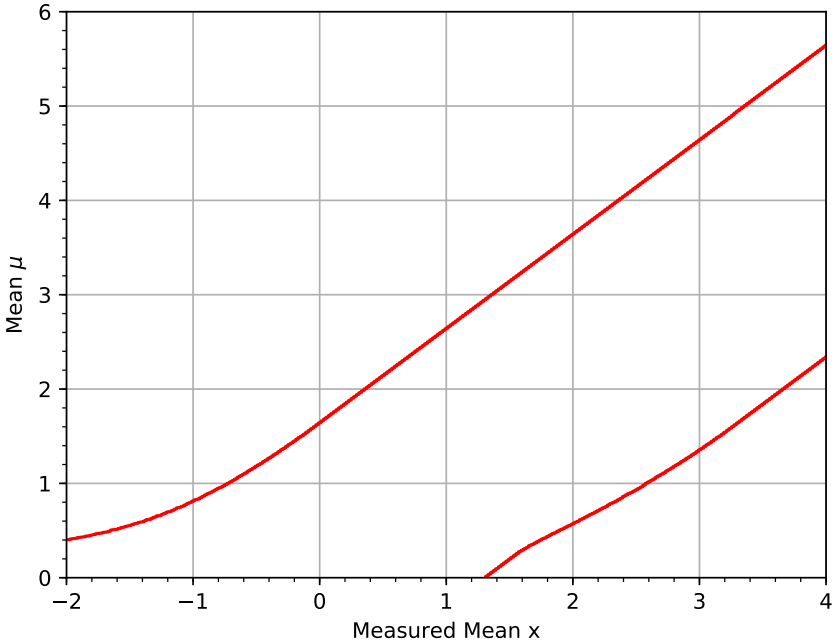


Figure A.2: 90% confidence intervals for the mean of a Gaussian, constrained to be non-negative.

$$\lambda(s) = \frac{P(n|s, b)}{P(n|s = 0, b)}$$

We want to find the value of  $s$  for which  $\lambda(s)$  is maximized, subject to the constraint that the total number of expected events is less than or equal to some upper limit  $s+b < \mu_{\max}$ . This corresponds to the upper limit on the number of signal events that we want to calculate.

Using the methods outlined in the previous response, we can find that the 90% confidence level upper limit on the number of signal events is 8.7. That is, if we observe 10 events in our data set and expect 8.3 events from background, we can say with 90% confidence that there are no more than 8.7 signal events present in the data.

Another example of the Feldman-Cousins approach in action is in the search for dark matter using the XENON1T experiment. In this case, the background is dominated by electronic recoil events from gamma rays, which can mimic the signal of dark matter interacting with the detector material.

Suppose we observe 5 events in the signal region of the XENON1T detector [102], and the expected background is 4.1 events with a Poisson uncertainty of  $\sqrt{4.1} \approx 2.0$  events. Using the same procedure as before, we can find that the 90% confidence level upper limit on the number of signal events is 4.9.

These examples demonstrate how the Feldman-Cousins approach can be applied in real-world searches for new physics, and how it can be used to set limits on the presence of signal events in the data, taking into account the uncertainty in the expected background. Refer to [85] for more details.

## Appendix B

# Incorporating of systematic uncertainties in limits computation

In particle physics, there are several methods for incorporating systematic uncertainties in limits computation. One approach is to use a frequentist framework with a likelihood function that incorporates systematic uncertainties as nuisance parameters. The resulting statistical inference can be performed using techniques such as maximum likelihood estimation or profile likelihood ratio tests.

Another approach is to use Bayesian statistics, which allows for the explicit inclusion of prior knowledge about the systematic uncertainties. In this case, the posterior probability density function can be calculated using Bayes' theorem, and limits can be obtained by integrating over the posterior distribution. Markov Chain Monte Carlo (MCMC) methods can be used to sample the posterior distribution and estimate the uncertainties in the limits.

As an example, the ATLAS experiment at CERN used the Bayesian approach to incorporate systematic uncertainties in a search for new physics in events with missing transverse energy and jets [103]. The analysis included several sources of systematic uncertainties, such as jet energy scale, missing transverse energy scale, and the modeling of the signal and background processes. The systematic uncertainties were incorporated using nuisance parameters with Gaussian prior distributions, and the posterior probability density function was sampled using MCMC techniques. The resulting limits on the signal cross section were presented with the uncertainties due to the systematic uncertainties. Another example is the search for dark matter with the XENON1T experiment [102]. The analysis included systematic uncertainties such as the energy scale, the efficiency of the detector, and the background model. The systematic uncertainties were incorporated using nuisance parameters with log-normal prior distributions, and a frequentist approach was used to calculate the limits on the dark matter-nucleon scattering cross section. The resulting limits were presented with the uncertainties due to the systematic uncertainties.

The incorporation of systematic uncertainties is a crucial aspect of limits computation in particle physics, and the choice of the statistical method and prior distributions can have a significant impact on the resulting limits. It is important to carefully consider the sources of systematic uncertainties and to perform thorough studies to assess their impact on the analysis.

The paper [90] proposes a method to incorporate systematic uncertainties in the calculation of confidence intervals for Poisson statistics. The method is based on the profile likelihood ratio, which is defined as:

$$\lambda(\mu, \boldsymbol{\theta}) = \frac{\mathcal{L}(\mu, \boldsymbol{\theta})}{\mathcal{L}(\hat{\mu}, \hat{\boldsymbol{\theta}})} \quad (\text{B.1})$$

where  $\mathcal{L}(\mu, \boldsymbol{\theta})$  is the likelihood function for the parameter of interest  $\mu$  and the nuisance parameters  $\boldsymbol{\theta}$ , and  $\hat{\mu}$  and  $\hat{\boldsymbol{\theta}}$  are the maximum likelihood estimators of these parameters.

To incorporate systematic uncertainties, the nuisance parameters are split into two groups: those that are affected by the systematic uncertainties (denoted by  $\boldsymbol{\alpha}$ ) and those that are not (denoted by  $\boldsymbol{\beta}$ ). The profile likelihood ratio is then modified to include the systematic uncertainties by maximizing over the nuisance parameters in  $\boldsymbol{\alpha}$ :

$$\lambda_s(\mu, \boldsymbol{\alpha}) = \frac{\mathcal{L}(\mu, \boldsymbol{\alpha}, \hat{\boldsymbol{\beta}})}{\mathcal{L}(\hat{\mu}, \hat{\boldsymbol{\alpha}}, \hat{\boldsymbol{\beta}})} \quad (\text{B.2})$$

where  $\hat{\boldsymbol{\beta}}$  are the maximum likelihood estimators of the nuisance parameters in  $\boldsymbol{\beta}$ .

To calculate confidence intervals, the distribution of the test statistic  $q = -2 \ln \lambda_s$  is compared to a  $\chi^2$  distribution with the appropriate number of degrees of freedom. The systematic uncertainties are incorporated by calculating the distribution of  $q$  for each value of  $\boldsymbol{\alpha}$ , and then combining these distributions using a prior probability distribution for  $\boldsymbol{\alpha}$ .

The method in [90] is illustrated with an example of a search for a rare decay in the MINOS experiment. The search is based on the observation of a small number of events, and the systematic uncertainties are dominated by the uncertainty in the detection efficiency. The paper shows that incorporating the systematic uncertainties leads to a significant improvement in the confidence interval construction.

Overall, the method proposed in the Conrad paper provides a way to include systematic uncertainties in the calculation of confidence intervals for Poisson statistics, and can be applied to a wide range of experiments in particle physics and beyond. This method is applied to incorporate systematics in the nuclearites paper [94].

# Bibliography

1. Agostini, M. & et al. Results on Neutrinoless Double Beta Decay of Ge76 from Phase I of the GERDA Experiment. *Physical Review Letters* **111**, 122503 (2013).
2. Alduino, C. & et al. First Results from CUORE: A Search for Lepton Number Violation via  $0^-$  Decay of 130Te. *Physical Review Letters* **120**, 132501 (2018).
3. Back, H. O. & et al. LUCIFER: an ultra-low background experiment for rare event searches. *European Physical Journal A* **52**, 181 (2016).
4. Aad, G. *et al.* Observation of a new particle in the search for the Standard Model Higgs boson with the ATLAS detector at the LHC. *Physics Letters B* **716**, 1–29. <https://www.sciencedirect.com/science/article/pii/S037026931200857X> (2012).
5. Chatrchyan, S. *et al.* Observation of a new boson at a mass of 125 GeV with the CMS experiment at the LHC. *Physics Letters B* **716**, 30–61. <https://www.sciencedirect.com/science/article/pii/S0370269312008581> (2012).
6. Collaboration, L. Observation of a new baryon state in the  $\Lambda_b^0 \rightarrow J/\psi p K^-$  decay. *Physical Review Letters* **122**, 252001. <https://journals.aps.org/prl/abstract/10.1103/PhysRevLett.122.252001> (25 2019).
7. Bodmer, A. R. Collapsed nuclei. *Physical Review D* **4**, 1601–1606. <https://journals.aps.org/prd/abstract/10.1103/PhysRevD.4.1601> (1971).
8. Witten, E. Superconducting quarks. *Nuclear Physics B* **249**, 557–592. <https://www.sciencedirect.com/science/article/pii/0550321385900227> (1985).
9. Albert, A. *et al.* Search for magnetic monopoles with ten years of the ANTARES neutrino telescope. *Journal of High Energy Astrophysics* **34**, 1–8. ISSN: 2214-4048. <https://www.sciencedirect.com/science/article/pii/S2214404822000118> (2022).
10. Abbasi, R. *et al.* Search for Relativistic Magnetic Monopoles with Eight Years of IceCube Data. *Phys. Rev. Lett.* **128**, 051101. <https://link.aps.org/doi/10.1103/PhysRevLett.128.051101> (5 2022).
11. Gaillard, M. K., Grannis, P. D. & Sciulli, F. J. The standard model of particle physics. *Rev. Mod. Phys.* **71**, S96–S111. <https://link.aps.org/doi/10.1103/RevModPhys.71.S96> (2 1999).
12. Hess, V. F. *Über Beobachtungen der durchdringenden Strahlung bei seben Freiballondurchfahrten* 1084. <http://cds.cern.ch/record/262750> (Z. Phys., 1912).
13. Simpson, J. A. Elemental and Isotopic Composition of the Galactic Cosmic Rays. *Annual Review of Nuclear and Particle Science* **33**, 323–382 (Dec. 1983).
14. BERTOU, X., BORATAV, M. & LETESSIER-SELVON, A. PHYSICS OF EXTREMELY HIGH ENERGY COSMIC RAYS. *International Journal of Modern Physics A* **15**, 2181–2224. <https://doi.org/10.1142/S0217751X00000902> (2000).
15. Greisen, K. End to the cosmic ray spectrum? *Phys. Rev. Lett.* **16**, 748–750 (1966).

16. T, Z. G. & A, K. V. Upper limit of the spectrum of cosmic rays. *JETP Lett.* **4**, 78–80 (1966).
17. Abraham, J. Observation of the suppression of the flux of cosmic rays above  $4 \times 10^{19} eV$ . *Phys. Rev. Lett.* **101**, 061101 (2008).
18. Fermi, E. On the Origin of the Cosmic Radiation. *Physical Review* **75**, 1169–1174 (Apr. 1949).
19. Bhattacharjee, P & Sigl, G. Monopole annihilation and highest energy cosmic rays. *Phys. Rev. D* **51**, 4079–4091. <https://link.aps.org/doi/10.1103/PhysRevD.51.4079> (1995).
20. Berezhinsky, V. & Vilenkin, A. Cosmic necklaces and ultrahigh energy cosmic rays. *Phys. Rev. Lett.* **79**, 5202–5205. <https://link.aps.org/doi/10.1103/PhysRevLett.79.5202> (1997).
21. Abraham, J. *et al.* Correlation of the Highest-Energy Cosmic Rays with Nearby Extragalactic Objects. *Science* **318**, 938–943. eprint: <https://www.science.org/doi/pdf/10.1126/science.1151124>. <https://www.science.org/doi/abs/10.1126/science.1151124> (2007).
22. Atwood, W. B. *et al.* THE LARGE AREA TELESCOPE ON THEFERMI GAMMA-RAY SPACE TELESCOPEMISSION. *The Astrophysical Journal* **697**, 1071–1102 (May 2009).
23. Aharonian, F. *et al.* The H.E.S.S. Survey of the Inner Galaxy in Very High Energy Gamma Rays. *The Astrophysical Journal* **636**, 777–797 (Jan. 2006).
24. Aharonian, F, Buckley, J, Kifune, T & Sinnis, G. High energy astrophysics with ground-based gamma ray detectors. *Reports on Progress in Physics* **71**, 096901 (Aug. 2008).
25. Halzen, F. & Hooper, D. High-energy neutrino astronomy: the cosmic ray connection. *Reports on Progress in Physics* **65**, 1025–1078 (June 2002).
26. Cowan, C. L., Reines, F., Harrison, F. B., Kruse, H. W. & McGuire, A. D. Detection of the Free Neutrino: a Confirmation. *Science* **124**, 103–104. [http://personal.psu.edu/rq9/HOW/Neutrino\\_discovery\\_1.pdf](http://personal.psu.edu/rq9/HOW/Neutrino_discovery_1.pdf) (July 1956).
27. Eidelman, S. *et al.* Review of Particle Physics. *Physics Letters B* **592**, 1–5 (July 2004).
28. Danby, G. *et al.* Observation of High-Energy Neutrino Reactions and the Existence of Two Kinds of Neutrinos. *Physical Review Letters* **9**, 36–44 (July 1962).
29. Perl, M. L. *et al.* Evidence for Anomalous Lepton Production in e+-e-Annihilation. *Physical Review Letters* **35**, 1489–1492 (Dec. 1975).
30. Kodama, K. *et al.* Observation of tau neutrino interactions. *Physics Letters B* **504**, 218–224 (Apr. 2001).
31. Bilen'kii, S. M. Neutrino masses, mixing and oscillations. *Physics-Uspekhi* **46**, 1137–1152 (Nov. 2003).
32. An, F. P. *et al.* Observation of Electron-Antineutrino Disappearance at Daya Bay. *Physical Review Letters* **108** (Apr. 2012).
33. Kappes, A., Hinton, J., Stegmann, C. & Aharonian, F. A. Potential Neutrino Signals from Galactic  $\gamma$ -RaySources. *The Astrophysical Journal* **656**, 870–878 (Feb. 2007).
34. Klebesadel, R. W., Strong, I. B. & Olson, R. A. Observations of Gamma-Ray Bursts of Cosmic Origin. *The Astrophysical Journal* **182**, L85 (June 1973).
35. Kouveliotou, C. *et al.* Identification of two classes of gamma-ray bursts. *The Astrophysical Journal Letters* **413**, L101–L104. <https://ui.adsabs.harvard.edu/abs/1993ApJ...413L.101K/abstract> (Aug. 1993).

36. Piran, T. Gamma-ray bursts and the fireball model. *Physics Reports* **314**, 575–667 (June 1999).
37. Orellana, M. *et al.* A model for the electromagnetic spectrum of the inner jets of Centaurus A. *AIP Conference Proceedings* (2009).
38. Owocki, S. P., Romero, G. E., Townsend, R. H. D. & Araudo, A. T. GAMMA-RAY VARIABILITY FROM WIND CLUMPING IN HIGH-MASS X-RAY BINARIES WITH JETS. *The Astrophysical Journal* **696**, 690–693 (Apr. 2009).
39. McKe, A., Engel, R., Rachen, J., Protheroe, R. & Stanev, T. Monte Carlo simulations of photohadronic processes in astrophysics. *Computer Physics Communications* **124**, 290–314 (Feb. 2000).
40. Böttcher, M., Aharonian, F. A., Hofmann, W. & Rieger, F. Implications of the VHE  $\gamma - Ray$  Detection of 3C279. *AIP Conference Proceedings* (2008).
41. Aharonian, F. *et al.* Detection of VHE gamma-ray emission from the distant blazar 1ES 1101-232 with HESS and broadband characterisation. *Astronomy & Astrophysics* **470**, 475–489 (May 2007).
42. Aharonian, F. TeV gamma rays from BL Lac objects due to synchrotron radiation of extremely high energy protons. *New Astronomy* **5**, 377–395 (Nov. 2000).
43. Crocker, R. M., Melia, F. & Volkas, R. R. Neutrinos from the galactic center in the light of its gamma-ray detection at TeV energy. *The Astrophysical Journal* **622**, L37–L40. <https://doi.org/10.1086/429539> (2005).
44. Kampert, K. Cosmic rays and particle physics. *Acta Physica Hungarica Series A, Heavy Ion Physics* **14**, 203–215. <https://doi.org/10.1556/APH.14.2001.14.20> (2001).
45. Waxman, E. & Loeb, A. TeV neutrinos and GeV photons from shock breakout in supernovae. *Phys. Rev. Lett.* **87**, 071101. <https://link.aps.org/doi/10.1103/PhysRevLett.87.071101> (2001).
46. Khélifi, B. *et al.* TeV gamma-ray observations of pulsar wind nebulae with the HESS detector. *Advances in Space Research* **35**, 1148–1151. <https://www.sciencedirect.com/science/article/pii/S0273117705001821> (2005).
47. Bednarek, W., Burgio, G. & Montaruli, T. Galactic discrete sources of high energy neutrinos. *New Astronomy Reviews* **49**, 1–21. <https://www.sciencedirect.com/science/article/pii/S1387647304001538> (2005).
48. L, G. V. & I, S. S. *The origin of cosmic rays* (1964).
49. Vissani, F. & Villante, F. L. Cosmic rays and neutrinos from supernova remnants: (or: the time when H.E.S.S. met Ginzburg and Syrovatskii). *Nuclear Instruments and Methods in Physics Research Section A: Accelerators, Spectrometers, Detectors and Associated Equipment* **588**, 123–129. <https://www.sciencedirect.com/science/article/pii/S0168900208000521> (2008).
50. Galata, S. *A time dependent search for neutrino emission from microquasars with the ANTARES telescope* PhD thesis (Apr. 2012). <https://tel.archives-ouvertes.fr/tel-00782883>.
51. Levinson, A. & Waxman, E. Probing microquasars with TeV neutrinos. *Phys. Rev. Lett.* **87**, 171101. <https://link.aps.org/doi/10.1103/PhysRevLett.87.171101> (2001).
52. E, R. G., F, T. D., Kaufman & F, M. I. Hadronic gamma-ray emission from windy microquasars. *A & A* **410**, L1–L4. <https://doi.org/10.1051/0004-6361:20031314-1> (2003).
53. .
54. Bodmer, A. R. Collapsed Nuclei. *Physical Review D* **4**, 1601–1606 (Sept. 1971).

55. Schneider, B. I., Le Dourneuf, M. & Lan, V. K. Resonant Vibrational Excitation of N<sub>2</sub> by Low-Energy Electrons: An Ab Initio R-Matrix Calculation. *Phys. Rev. Lett.* **43**, 1926–1929. <https://link.aps.org/doi/10.1103/PhysRevLett.43.1926> (26 1979).
56. Bjorken, J. D. & McLerran, L. D. Explosive quark matter and the "Centauro" event. *Physical Review D* **20**, 2353–2360 (Nov. 1979).
57. DeGrand, T., Jaffe, R. L., Johnson, K. & Kiskis, J. Masses and other parameters of the light hadrons. *Physical Review D* **12**, 2060–2076 (Oct. 1975).
58. DeGrand, T., Jaffe, R. L., Johnson, K. & Kiskis, J. Masses and other parameters of the light hadrons. *Phys. Rev. D* **12**, 2060–2076. <https://link.aps.org/doi/10.1103/PhysRevD.12.2060> (7 1975).
59. Farhi, E. & Jaffe, R. L. Strange matter. *Physical Review D* **30**, 2379–2390 (Dec. 1984).
60. Witten, E. Cosmic separation of phases. *Physical Review D* **30**, 272–285 (July 1984).
61. De Rújula, A. Aborigines of the nuclear desert. *Nuclear Physics A* **434**, 605–626. ISSN: 0375-9474. <https://www.sciencedirect.com/science/article/pii/0375947485905251> (1985).
62. De Rújula, A. & Glashow, S. L. Nuclearites-a novel form of cosmic radiation. *Nature* **312**, 734–737 (Dec. 1984).
63. Guo, W.-L., Xia, C.-J., Lin, T. & Wang, Z.-M. Exploring detection of nuclearites in a large liquid scintillator neutrino detector. *Phys. Rev. D* **95**, 015010. <https://link.aps.org/doi/10.1103/PhysRevD.95.015010> (1 2017).
64. Ambrosio et al., M. & Collaboration, T. M. Nuclearite search with the MACRO detector at Gran Sasso. *The European Physical Journal C - Particles and Fields* **13**, 453–458. ISSN: 1434-6052. <https://doi.org/10.1007/s100520000142> (2000).
65. Cecchini, S. et al. Results of the search for strange quark matter and Q-balls with the SLIM experiment. *The European Physical Journal C* **57**, 525–533. ISSN: 1434-6052. <https://doi.org/10.1140/epjc/s10052-008-0747-7> (2008).
66. Kazama, Y., Yang, C. N. & Goldhaber, A. S. Scattering of a Dirac particle with charge Ze by a fixed magnetic monopole. *Phys. Rev. D* **15**, 2287–2299. <https://link.aps.org/doi/10.1103/PhysRevD.15.2287> (8 1977).
67. Albert, A. et al. Search for relativistic magnetic monopoles with five years of the ANTARES detector data. *Journal of High Energy Physics* **2017**, 54. ISSN: 1029-8479. [https://doi.org/10.1007/JHEP07\(2017\)054](https://doi.org/10.1007/JHEP07(2017)054) (2017).
68. Ahlen, S. P. Monopole-track characteristics in plastic detectors. *Phys. Rev. D* **14**, 2935–2940. <https://link.aps.org/doi/10.1103/PhysRevD.14.2935> (11 1976).
69. Lee, T. & Pang, Y. Nontopological solitons. *Physics Reports* **221**, 251–350. ISSN: 0370-1573. <https://www.sciencedirect.com/science/article/pii/0370157392900647> (1992).
70. Mermin, N. D. & Wagner, H. Absence of Ferromagnetism or Antiferromagnetism in One- or Two-Dimensional Isotropic Heisenberg Models. *Phys. Rev. Lett.* **17**, 1133–1136. <https://link.aps.org/doi/10.1103/PhysRevLett.17.1133> (22 1966).
71. Coleman, S. There are no Goldstone bosons in two dimensions. *Communications in Mathematical Physics* **31**, 259–264. ISSN: 1432-0916. <https://doi.org/10.1007/BF01646487> (1973).
72. Friedberg, R., Lee, T. D. & Sirlin, A. Class of scalar-field soliton solutions in three space dimensions. *Phys. Rev. D* **13**, 2739–2761. <https://link.aps.org/doi/10.1103/PhysRevD.13.2739> (10 1976).

73. Cowan, C. L., Reines, F., Harrison, F. B., Kruse, H. W. & McGuire, A. D. Detection of the Free Neutrino: a Confirmation. *Science* **124**, 103–104. eprint: <https://www.science.org/doi/pdf/10.1126/science.124.3212.103>. <https://www.science.org/doi/abs/10.1126/science.124.3212.103> (1956).
74. Hirata, K. S. *et al.* Observation of  ${}^8\text{B}$  solar neutrinos in the Kamiokande-II detector. *Phys. Rev. Lett.* **63**, 16–19. <https://link.aps.org/doi/10.1103/PhysRevLett.63.16> (1 1989).
75. Reines, F. *et al.* Evidence for High-Energy Cosmic-Ray Neutrino Interactions. *Phys. Rev. Lett.* **15**, 429–433. <https://link.aps.org/doi/10.1103/PhysRevLett.15.429> (9 1965).
76. Achar, C. *et al.* Detection of muons produced by cosmic ray neutrinos deep underground. *Physics Letters* **18**, 196–199. ISSN: 0031-9163. <https://www.sciencedirect.com/science/article/pii/0031916365907122> (1965).
77. Collaboration\*, I. Evidence for High-Energy Extraterrestrial Neutrinos at the Ice-Cube Detector. *Science* **342**, 1242856. eprint: <https://www.science.org/doi/pdf/10.1126/science.1242856>. <https://www.science.org/doi/abs/10.1126/science.1242856> (2013).
78. Roberts, A. The birth of high-energy neutrino astronomy: A personal history of the DUMAND project. *Rev. Mod. Phys.* **64**, 259–312. <https://link.aps.org/doi/10.1103/RevModPhys.64.259> (1 1992).
79. Belolaptikov, I. *et al.* The Baikal underwater neutrino telescope: Design, performance, and first results. *Astroparticle Physics* **7**, 263–282. ISSN: 0927-6505. <https://www.sciencedirect.com/science/article/pii/S0927650597000224> (1997).
80. Ageron, M. *et al.* ANTARES: The first undersea neutrino telescope. *Nuclear Instruments and Methods in Physics Research Section A: Accelerators, Spectrometers, Detectors and Associated Equipment* **656**, 11–38 (Nov. 2011).
81. Aguilar, J. *et al.* The data acquisition system for the ANTARES neutrino telescope. *Nuclear Instruments and Methods in Physics Research Section A: Accelerators, Spectrometers, Detectors and Associated Equipment* **570**, 107–116 (Jan. 2007).
82. Carminati, G., Bazzotti, M., Margiotta, A. & Spurio, M. Atmospheric MUons from PArametric formulas: a fast GEnerator for neutrino telescopes (MUPAGE). *Computer Physics Communications* **179**, 915–923 (Dec. 2008).
83. Albert, A. *et al.* Monte Carlo simulations for the ANTARES underwater neutrino telescope. *Journal of Cosmology and Astroparticle Physics* **2021**, 064–064 (Jan. 2021).
84. Hill, G. C. & Rawlins, K. Unbiased cut selection for optimal upper limits in neutrino detectors: the model rejection potential technique. *Astroparticle Physics* **19**, 393–402 (June 2003).
85. Feldman, G. J. & Cousins, R. D. Unified approach to the classical statistical analysis of small signals. *Physical Review D* **57**, 3873–3889 (Apr. 1998).
86. Aguilar, J. *et al.* Transmission of light in deep sea water at the site of the Antares neutrino telescope. *Astroparticle Physics* **23**, 131–155. ISSN: 0927-6505. <https://www.sciencedirect.com/science/article/pii/S0927650504001902> (2005).
87. Amram, P *et al.* The ANTARES optical module. *Nuclear Instruments and Methods in Physics Research Section A: Accelerators, Spectrometers, Detectors and Associated Equipment* **484**, 369–383. ISSN: 0168-9002. <https://www.sciencedirect.com/science/article/pii/S0168900201020265> (2002).
88. Albert, A. *et al.* Search for magnetic monopoles with ten years of the ANTARES neutrino telescope. *Journal of High Energy Astrophysics* **34**, 1–8. ISSN: 2214-4048.

- <https://www.sciencedirect.com/science/article/pii/S2214404822000118> (2022).
89. Aguilar, J. *et al.* Zenith distribution and flux of atmospheric muons measured with the 5-line ANTARES detector. *Astroparticle Physics* **34**, 179–184. ISSN: 0927-6505. <https://www.sciencedirect.com/science/article/pii/S0927650510001246> (2010).
  90. Conrad, J., Botner, O., Hallgren, A. & Pérez de los Heros, C. Including systematic uncertainties in confidence interval construction for Poisson statistics. *Phys. Rev. D* **67**, 012002. <https://link.aps.org/doi/10.1103/PhysRevD.67.012002> (1 2003).
  91. Păvălaş, G. E. Search for nuclearites with the ANTARES neutrino telescope. *Proceedings of The 34th International Cosmic Ray Conference — PoS(ICRC2015)* (Aug. 2016).
  92. Ambrosio et al., M. Nuclearite search with the MACRO detector at Gran Sasso. *The European Physical Journal C* **13**, 453–458 (Apr. 2000).
  93. Cecchini, S. *et al.* Results of the search for strange quark matter and Q-balls with the SLIM experiment. *The European Physical Journal C* **57**, 525–533 (Oct. 2008).
  94. Albert, A. *et al.* Limits on the nuclearite flux using the ANTARES neutrino telescope. *Journal of Cosmology and Astroparticle Physics* **2023**, 012. <https://dx.doi.org/10.1088/1475-7516/2023/01/012> (2023).
  95. Aiello, S. *et al.* Determining the neutrino mass ordering and oscillation parameters with KM3NeT/ORCA. *The European Physical Journal C* **82**. (2022) (Jan. 2022).
  96. Aiello, S. *et al.* Characterisation of the Hamamatsu photomultipliers for the KM3NeT Neutrino Telescope. *Journal of Instrumentation* **13**, P05035. <https://dx.doi.org/10.1088/1748-0221/13/05/P05035> (2018).
  97. Aguilar, J. *et al.* A fast algorithm for muon track reconstruction and its application to the ANTARES neutrino telescope. *Astroparticle Physics* **34**, 652–662. ISSN: 0927-6505. <https://www.sciencedirect.com/science/article/pii/S0927650511000053> (2011).
  98. Aiello, S. *et al.* Implementation and first results of the KM3NeT real-time core-collapse supernova neutrino search. *The European Physical Journal C* **82**, 317. ISSN: 1434-6052. <https://doi.org/10.1140/epjc/s10052-022-10137-y> (2022).
  99. Ageron, M. *et al.* Dependence of atmospheric muon flux on seawater depth measured with the first KM3NeT detection units. *The European Physical Journal C* **80**, 99. ISSN: 1434-6052. <https://doi.org/10.1140/epjc/s10052-020-7629-z> (2020).
  100. Aiello, S. *et al.* Determining the neutrino mass ordering and oscillation parameters with KM3NeT/ORCA. *The European Physical Journal C* **82**, 26. ISSN: 1434-6052. <https://doi.org/10.1140/epjc/s10052-021-09893-0> (2022).
  101. Aartsen, M. G. *et al.* The IceCube Neutrino Observatory: Instrumentation and Online Systems. *JINST* **12**, P03012. arXiv: [1612.05093 \[astro-ph.IM\]](https://arxiv.org/abs/1612.05093) (2017).
  102. Aprile, E. *et al.* The XENON1T dark matter experiment. *The European Physical Journal C* **77**, 881. ISSN: 1434-6052. <https://doi.org/10.1140/epjc/s10052-017-5326-3> (2017).
  103. Aaboud, M. *et al.* Search for new phenomena in events with a photon and missing transverse momentum in pp collisions at  $\sqrt{s} = 13\text{TeV}$  with the ATLAS detector. *Journal of High Energy Physics* **2016**, 59. ISSN: 1029-8479. [https://doi.org/10.1007/JHEP06\(2016\)059](https://doi.org/10.1007/JHEP06(2016)059) (2016).